

PHD THESIS

Mixing and Evaporation at the Cloud Edge and Angular
Dynamics of Small Crystals in Viscous Flow

JOHAN FRIES

Department of Physics
University of Gothenburg
Göteborg, Sweden 2022

*Mixing and Evaporation at the Cloud Edge and Angular Dynamics of Small Crystals
in Viscous Flow*

Johan Fries

ISBN 978-91-8009-628-7 (PRINT)

ISBN 978-91-8009-629-4 (PDF)

Department of Physics
University of Gothenburg
SE-412 96 Göteborg
Sweden

Telephone: +46 (0)31-786 00 00

Printed by Stema Specialtryck AB
Borås, Sweden 2022



ABSTRACT

How liquid water in atmospheric clouds distributes over droplets of different sizes is important for the initiation of rainfall, and for the optical properties of the atmosphere. Droplet-number densities and droplet-size distributions change rapidly at turbulent cloud edges, where mixing of cloudy and dry air causes cloud dilution and droplet evaporation. The resulting droplet configurations are determined by how individual micrometer-sized droplets are exposed to dry air, by a turbulent flow whose length scales range from millimeters to hundreds of meters.

A first part of this thesis is on mixing and evaporation at turbulent cloud edges. It is explained how several results from numerical simulations can be understood in a simple way by simplifying and non-dimensionalizing a widely used model. The simple understanding makes it possible to interpret empirical data, and to analyze of the multiscale nature of mixing and evaporation in clouds. Two statistical models for mixing and evaporation are presented. The first reproduces the broadening of the droplet-size distribution observed in direct numerical simulations (DNS), but has an oversimplified supersaturation dynamics. This problem is partially resolved in the second model, which under some conditions reproduces the supersaturations of droplets in DNS quantitatively.

A second part of the thesis is on the angular dynamics of small particles in flow. How particles spin and tumble is important for many different phenomena, including the intrinsic viscosity of particle suspensions, the settling of ice crystals in clouds, and the motion of plankton. It is predicted that particles that possess a rotation symmetry and a reflection symmetry in a plane that contains the axis of rotation symmetry spin and tumble like spheroids in Stokes flow. This prediction is verified in an experiment where the angular dynamics of triangular particles in a simple shear flow is observed. The angular dynamics of rotation-symmetric particles without the above-mentioned reflection symmetry is analyzed.

LIST OF PAPERS

This thesis consists of an introductory text and the following three appended papers:

Paper A

FRIES, J., SARDINA, G., SVENSSON, G., & MEHLIG, B. Key parameters for droplet evaporation and mixing at the cloud edge. *Quarterly Journal of the Royal Meteorological Society* **147**, 2160 – 2172, (2021).

Paper B

FRIES, J., EINARSSON, J., & MEHLIG, B. Angular dynamics of small crystals in viscous flow. *Physical Review Fluids* **2**, 014302, (2017).

Paper C

FRIES, J., KUMAR, M. V., MIHIRETIE, B. M., HANSTORP, D., & MEHLIG, B. Spinning and tumbling of micron-sized triangles in a micro-channel shear flow. *Physics of Fluids* **30**, 033304, (2018).

My contributions to the appended papers are:

- **Paper A:** I formulated the research questions together with GS, GS, and BM. I developed the theory under guidance of BM. I wrote the paper together with GS, GS, and BM.
- **Paper B:** I developed the theory together with JE and BM. I did all numerical computations, and contributed to the writing of the paper.
- **Paper C:** I formulated the research question together with BM. I developed the detailed experimental procedure together with MVK, performed major parts of the data analysis, and did all numerical computations. I also contributed to the writing of the paper.

ACKNOWLEDGEMENTS

First of all I would like to thank my main supervisor Bernhard Mehlig for his dedicated support and guidance. Bernhard continuously provided encouragement, and his insightful feedback pushed me to sharpen my thinking. I am also grateful to my co-supervisor Kristian Gustavsson for thoughtful comments and clarifying discussions.

I thank Gaetano Sardina for introducing me to cloud modeling, and for always finding time to answer my questions. I thank Gunilla Svensson, whose broad understanding of clouds and climate has helped me to put my work into context. I thank my co-authors Jonas Einarsson, Dag Hanstorp, Muthu Vijay Kumar, and Beshira Mekonnen Mihiretie for their contributions. I am generally thankful for been given the opportunity to meet with many knowledgeable and stimulating scientists during my studies. Discussions with Jeremy Bec, Ekaterina Ehzova, Szymon Malinowski, and Raymond Shaw have provided particularly valuable insights.

I thank my office mates Anshuman, Ludvig and Jan for being present both scientifically and friendly in my everyday life. My family has persistently supported and endured my work, and for that I am truly grateful. A special thanks to my brother Stefan who lent out his apartment during my last days of thesis writing.

Already published material in this thesis

This thesis builds partly upon my licentiate thesis (defended Mars 19, 2021). All papers included in this thesis were also included in the licentiate. By chapter, the contribution from the licentiate thesis is as follows:

- Chapter 1: This chapter was a part of the licentiate. For this thesis the literature review on cloud modeling in Section 1.1.5 has been extended, and material has been added to introduce the new Chapter 3. About 10 % of the text and references in Chapter 1 are new.
- Chapter 2: This chapter was a part of the licentiate. The literature review in Section 2.1 has been extended. Section 2.2 has been modified (restructured, shortened, and extended) and connected to the new Chapter 3. About 20 % of the text and references in Chapter 2 are new.
- Chapter 3: This chapter is new.
- Chapter 4: This chapter was a part of the licentiate, and only minor changes have been made.
- Chapter 5: This chapter was a part of the licentiate. Conclusions from Chapter 3 have been added to Chapter 5.
- Chapter 6: Section 6.4 was a part of the licentiate. Sections 6.1-6.3 are new.
- Chapter 7: Appendices A and B are new. Appendix C was a part of the licentiate.

Contents

1	Introduction	1
1.1	Dynamics and thermodynamics	4
2	Mixing and evaporation at the cloud edge	23
2.1	Background	23
2.2	My work	26
2.3	Discussion	35
3	Improved statistical model for the cloud edge	37
3.1	Background	37
3.2	My work	38
3.3	Discussion	55
4	Angular dynamics of small crystals in flow	58
4.1	Background	58
4.2	My work	67
4.3	Discussion	70
5	Conclusions	72
6	Outlook	74
6.1	Further improved cloud-edge model	74
6.2	Improved cloud-core models	75
6.3	Three-parameter analysis of empirical data	75
6.4	Intrinsic viscosity of a suspension of particles with non-zero Ψ	76
7	Appendices	77
A	Complete description of simulations in Section 3.2.5	77
B	Derivation of Eq. (3.8)	79
C	Particles with non-zero Γ and Ψ	82
	References	91

1 Introduction

A first part of this thesis is on the evaporation of cloud droplets – micron-sized spherical drops of liquid water – that are turbulently mixed with dry air at the edge of a cloud. A second part is on the angular dynamics of small crystals in flow. The common denominator of these topics is that they concern particles in flow. Clouds are inhomogeneous and transient aggregates of droplets. The droplets evaporate or condensate in response to the air at their positions, while they are being carried by a turbulent air flow. Crystals are particles that possess symmetries, and the angular dynamics of small symmetrical particles is determined by how their symmetries relate to flow gradients at their positions.

Mixing and evaporation at the cloud edge

Clouds are important for most life forms on Earth. Their precipitation constitutes our primary source of fresh water, and they play a pivotal role for the climate we live in by reflecting about 20 % of the solar radiation that reaches Earth from space [Wallace & Hobbs, 2006]. The physics of clouds spans a vast range of length and time scales. Earth's rotation induces jet streams whose sizes are comparable to the planet itself [Lamb & Verlinde, 2011]. These jet streams can last for more than 20 days [Degirmendžić & Wibig, 2007], and are responsible for the formation of cyclones in which clouds form and precipitate. Cloud droplets form when liquid water condenses upon nanometer-sized condensation nuclei, while they are advected by small-scale turbulence with fluctuations on time scales of milliseconds [Devenish *et al.*, 2012]. In one way or another, models for weather and climate must describe the multiscale nature of clouds. More research is needed to understand the strong couplings that exist between processes at different scales, not least because cloud effects constitute the major sources of uncertainty in models for the global climate [Schwartz, 2008; Bellouin *et al.*, 2020].

The physical processes that cause ice-free clouds to rain within about 15 minutes after their formation [Szumowski *et al.*, 1997, 1998] are not well understood [Grabowski & Wang, 2013]. For such rapid onsets of rainfall, droplets must collide and merge with each other [Yau & Rogers, 1989]. But it is difficult to explain how collisions come about, because they require that

some droplets have had time to grow large enough to detach from the air that carries them. The combined effect of mixing and evaporation has been suggested as a plausible resolution to this bottleneck problem of droplet growth [Lasher-Trapp *et al.*, 2005]. Mixing and evaporation can generate cloud regions with low droplet-number densities, in which droplets may grow rapidly by condensation, because the competition for water vapor is small [Cooper, 1989].

At the edge of a turbulent cloud, mixing induces rapid droplet evaporation, by exposing droplets to dry non-cloudy air. The induced evaporation is self-limited, because evaporating droplets may evaporate completely and vanish, or saturate the air that they are mixed with. How droplets are affected by cloud-edge mixing and evaporation therefore depends on how the thermodynamic processes of evaporation and saturation couple to each other, and on how they couple to the turbulent dynamics of the air. The way in which evaporation distributes over droplets that are mixed affects how deep into a cloud solar radiation penetrates [Grabowski, 2006]. Solar radiation interacts with droplet surfaces, and for a given amount of liquid water this surface area is small if the droplets are few and large, and large if they are many and small. A simple analysis of Jeffery [2007] suggests that the optical depth of a cloud may be 50 % larger if evaporation distributes inhomogeneously over mixed droplets, than if all mixed droplets evaporate by the same amount.

Cloud-edge mixing and evaporation takes place at many different length and time scales simultaneously, and has been understood as multiscale processes for a long time [Baker *et al.*, 1980]. It has however not been clear how this multiscale process should be described. What is an appropriate model, and what is the physical meaning of the model parameters? In Paper A, introduced in Chapter 2, the latter of these two questions is resolved for a widely used model. By identifying the most relevant non-dimensional parameters of cloud-edge mixing and evaporation, we provide a simple way to understand several results from numerical simulations. Furthermore, we relate the model to local conditions in a cloud at different scales, and present a new theory for analyzing empirical data.

In Paper A we derive a statistical model to compute our numerical results. We find that the model reproduces the broadening of the droplet-size distribution observed in direct numerical simulations (DNS) of transient cloud-edge mixing. However, the model does not quantitatively reproduce

the supersaturations of droplets. In Chapter 3, I present an improved statistical model that partially overcomes this deficiency. The improved statistical model quantitatively reproduces the supersaturations of droplets in DNS when droplet phase change is slow compared to the rate of mixing, and after the initial transient when droplet phase change is fast. In Chapter 3, I use the model to analyze similarities and differences between the dynamics of supersaturation and that of a passive scalar.

Cloud droplets exist under many different cloud conditions and take part in a large variety of cloud processes [Yau & Rogers, 1989]. In the cloud-edge part of this thesis, I limit my scope to droplet phase change and cloud mixing in ice-free turbulent clouds. Phase changes that include ice are beyond this scope, and droplet formation and collision are only briefly discussed.

Angular dynamics of small crystals in viscous flow

The angular dynamics of particles in flow is of interest in many contexts. How plankton rotate in shear flow is studied within the field of oceanography, because the rotation of a plankton determines the way in which it encounters nutrients and other microorganisms [Nguyen *et al.*, 2011]. The orientational distribution of settling ice crystals in clouds is a topic of active research [Jucha *et al.*, 2018; Gustavsson *et al.*, 2019, 2020; Anand *et al.*, 2020]. Leal & Hinch [1971] were able to compute the intrinsic viscosity of a dilute suspension of small spheroidal particles rotated by a flow gradient and Brownian noise. Their results have later been generalized to suspensions of general ellipsoidal particles [Rallison, 1978; Almondo *et al.*, 2018].

The way in which a particle spins and tumbles depends on the flow that it encounters, but also on its shape. Many of the above mentioned particles possess symmetries, and these symmetries can be exploited to find constraints on their angular equations of motion, if the particles are small enough. With small enough, I mean that the particles are so small their inertia and the inertia of the flow in their vicinities can be neglected. When all inertial effects can be neglected, the angular dynamics are completely determined by viscous stresses of the flow, and the flow is governed by Stokes equations [Kim & Karrila, 1991].

It is frequently stated that an axisymmetric particle has the same angular dynamics as an equivalent spheroid in Stokes flow [Gustavsson *et al.*, 2020; Kim & Karrila, 1991; Einarsson *et al.*, 2014]. But Bretherton [1962] showed

that there are axisymmetric particles that do not move as spheroids already in 1962. In Paper B, introduced in Chapter 4, the symmetry requirements are sorted out. Here, we show that axisymmetry is required in two senses: Rotation symmetry is not enough, but a particle spins and tumbles as a spheroid if it also possesses a reflection symmetry in a plane that contains the axis of rotation symmetry.

A small-enough platelet shaped as an equilateral triangle is an example of a particle that is predicted to spin and tumble like a spheroid in Paper B. In Paper C, also introduced in Chapter 4, this prediction is verified through an experiment. In the experiment, the spinning and tumbling of micron-sized triangular particles in a micro-channel shear flow is observed. The symmetry axis of the triangle tumbles periodically upon a so-called Jeffery orbit, while the particle spins at a different rate. The full three-dimensional motion can be reconstructed from the observations, because the triangle has corners.

Thesis outline

This thesis is organized as follows. In the immediate following, I introduce the dynamics and thermodynamics that concern this thesis. After that, in Chapter 2, I introduce Paper A, which is on mixing and evaporation at the edge of an ice-free cloud. In Chapter 3, I present the improved statistical model for cloud-edge mixing and evaporation mentioned above. In Chapter 4, I introduce Papers B and C, which are on the angular dynamics of particles that possess certain symmetries. I conclude with Chapter 5. Chapter 6 contains an outlook, where I discuss possible directions for future research. Chapter 7 contains appendices. After that follows a list of references, and Papers A, B, and C.

1.1 Dynamics and thermodynamics

This section introduces dynamics and thermodynamics that concerns this thesis. Section 1.1.1 is on the thermodynamics of clouds. In Section 1.1.2, I introduce a set of fundamental microscopic equations that describe how cloud thermodynamics is at work in the air flow of the atmosphere. The flow within turbulent clouds can be analyzed using Kolmogorov's theory from 1941 [Kolmogorov, 1941], which I introduce in Section 1.1.3. In Section 1.1.4, I introduce the translational and angular dynamics of cloud droplets and

small non-spherical particles. Finally, in Section 1.1.5, I introduce different types of models that are important for the understanding of clouds and cloud edges.

1.1.1 Cloud thermodynamics

Most clouds reside within the troposphere, a layer of the atmosphere that extends from the Earth's surface to altitudes of around 10 km [Lamb & Verlinde, 2011]. Air in the troposphere is a mixture that consists mainly of nitrogen and oxygen, but also some argon, carbon dioxide, and water vapor. At a position \mathbf{x} and time t the air has a pressure $p(\mathbf{x}, t)$, a density $\varrho(\mathbf{x}, t)$, and a temperature $T(\mathbf{x}, t)$. Even though these quantities vary within the troposphere, air is well described as an ideal gas at every position [Yau & Rogers, 1989]. The equation of state,

$$p = \varrho RT, \quad (1.1)$$

holds pointwise. Here, I introduced R to denote the gas constant of air.

An ice-free cloud forms as air is carried upwards and cools through expansion work, so that water vapor condenses into droplets. The, rather small, amount of water vapor is therefore essential for the thermodynamics of clouds. Water vapor is the gas that exchanges mass with droplets that condensate or evaporate, and to understand phase changes in clouds it is sufficient to describe this gas separately, and all other gases together. The mixture of all gases except water vapor is referred to as dry air [Yau & Rogers, 1989]. Both water vapor and dry air are well described as ideal gases, with partial pressures $p_v(\mathbf{x}, t)$ and $p_a(\mathbf{x}, t)$, and gas constants R_v and R_a . Their equations of state read:

$$p_v = \varrho_v R_v T \quad \text{and} \quad p_a = \varrho_a R_a T. \quad (1.2)$$

In terms of R_v and R_a , the gas constant of air is given by

$$R = \frac{\varrho_a R_a + \varrho_v R_v}{\varrho_a + \varrho_v}. \quad (1.3)$$

Dry adiabatic atmosphere

Temperature, pressure, and density of air tend to decrease with height within the troposphere, as a consequence of the gravitational acceleration. To

grasp mechanisms behind large-scale variations within the troposphere, it is useful to consider a so-called dry adiabatic atmosphere [Lamb & Verlinde, 2011]. A dry adiabatic atmosphere consists of dry air only ($\varrho_v = 0$), and its thermodynamic variables are subject to two constraints. One is that the atmosphere is at hydrostatic equilibrium. The other follows by assuming that air masses undergo adiabatic changes while descending or ascending.

Hydrostatic equilibrium means that pressure fluctuations due to air motion immediately fade away, so that the gravitational force upon the air is precisely balanced by a vertical pressure gradient. All state variables are then functions of the altitude z only, and we have

$$\frac{dp}{dz} = -\varrho |\mathbf{g}|, \quad (1.4)$$

where \mathbf{g} is the gravitational acceleration.

To adopt the hydrostatic pressure at its altitude, air expands or contracts as it moves upwards or downwards. The first law of thermodynamics dictates that the internal energy changes upon compression or expansion, and upon the addition or removal of heat. Denoting the internal energy and heat source per unit mass by $U(\mathbf{x}, t)$ and $Q(\mathbf{x}, t)$, the first law of thermodynamics reads [Yau & Rogers, 1989]:

$$dU = Q + \frac{p}{\varrho^2} d\varrho. \quad (1.5)$$

The adiabatic constraint is $Q(\mathbf{x}, t) = 0$, and means that heat sources and sinks resulting from thermal conduction or radiation are neglected. Described as an ideal gas, the internal energy $U(\mathbf{x}, t)$ depends on temperature only,

$$dU = c_v dT. \quad (1.6)$$

Here, c_v is the heat capacity per unit mass of dry air at constant volume.

By combining Eqs. (1.1) and (1.4) to (1.6), and imposing $Q(\mathbf{x}, t) = 0$, one obtains the vertical profiles of pressure, density, and temperature of a dry adiabatic atmosphere:

$$p = p_r \left(1 - \frac{|\mathbf{g}|}{c_p T_r} z \right)^{\frac{c_p}{R_a}}, \quad \varrho = \varrho_r \left(1 - \frac{|\mathbf{g}|}{c_p T_r} z \right)^{\frac{c_p}{R_a} - 1}, \quad \text{and} \quad T = T_r - \frac{|\mathbf{g}|}{c_p} z. \quad (1.7)$$

Here, $c_p = c_v + R_a$ is the heat capacity per unit mass of dry air at constant pressure. Furthermore, p_r , ρ_r , and T_r are the pressure, density, and temperature at sea-level, $z = 0$. Fig. (1.1) shows the vertical profiles of Eqs. (1.7). The linear decrease of temperature with altitude can be seen, as well as the power-law dependences of pressure and density. Assuming a sea-level temperature $T_r = 20^\circ\text{C}$, the pressure at 10 km altitude is only 20 % of the pressure at sea level. The density and temperature at 10 km are 40 % and 70 % of their sea-level values.

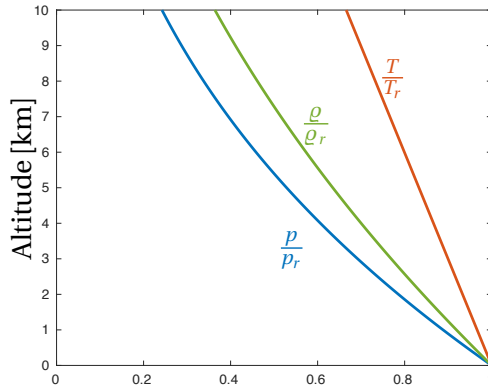


Figure 1.1: Pressure p , density ρ and temperature T of a dry adiabatic atmosphere, Eqs. (1.7). The vertical axis is the altitude z , so $z = 0$ at sea level. The profiles are computed using $T_r = 20^\circ\text{C}$, a typical sea-level temperature.

The negative temperature gradient of a dry adiabatic atmosphere,

$$\Gamma_d = \frac{|\mathbf{g}|}{c_p} = 0.01 \text{ K/m}, \quad (1.8)$$

is called the dry adiabatic lapse rate. Eq. (1.8) tells us that the temperature decreases by 1°C as one moves 100 m upwards in a dry adiabatic atmosphere. This height dependence is observed under some conditions [Chen *et al.*, 2013], but in general the temperature gradient is less steep. This can be understood from that the average temperature lapse rate in the atmosphere is 0.006 K/m [Cavcar, 2000], 60 % of the dry adiabatic lapse rate. This means that the adiabatic and hydrostatic constraints are not always fulfilled, but can be used to predict the order of magnitude of temperature lapse rate. That the order of magnitude comes out correctly suggests that the part of the

atmosphere where clouds are found is, up to a first approximation, adiabatic and hydrostatic.

Allowing for violations of the hydrostatic constraint, one finds that the dry adiabatic lapse rate Γ_d is an upper bound for the temperature lapse rate [Yau & Rogers, 1989]. The vertical structure of the atmosphere becomes unstable when this bound is violated. This is important for cloud formation, because air masses tend to move upwards and form clouds in an unstable atmosphere.

Droplet condensation and evaporation

For water vapor to condense into liquid water, its partial pressure $p_v(\mathbf{x}, t)$ must exceed the saturation vapor pressure $p_{vs}(T)$ with respect to liquid water. The saturation pressure increases with the temperature $T(\mathbf{x}, t)$, and is to a first approximation given by [Yau & Rogers, 1989]:

$$p_{vs}(T) = p_{vs}(\hat{T}) \exp \left[\frac{L_Q}{R_v} \left(\frac{1}{\hat{T}} - \frac{1}{T} \right) \right]. \quad (1.9)$$

Here, $\hat{T} = 0^\circ\text{C}$ is a reference temperature, and $p_{vs}(\hat{T} = 0^\circ\text{C}) = 611$ Pa. The latent heat of water vapor is denoted by L_Q , and assumed constant. More exact expressions for the saturation vapor pressure are given by Yau & Rogers [1989].

Water vapor may condense and cause droplets to grow where p_v exceeds p_{vs} , so that the supersaturation

$$s(\mathbf{x}, t) = \frac{p_v(\mathbf{x}, t)}{p_{vs}[T(\mathbf{x}, t)]} - 1 \quad (1.10)$$

is positive. I write 'may', because the growth of a very small droplet is counteracted by its surface tension. Due to this surface tension, the supersaturation must exceed a small positive threshold to initiate the formation and growth of a very small droplet. However, once a droplet has grown to a radius of about $1 \mu\text{m}$, the growth effects of surface tension become very small [Yau & Rogers, 1989].

For a droplet α whose radius $r_\alpha(t)$ is a few micrometers, the growth equation

$$\frac{dr_\alpha^2}{dt} = 2A_3 s(\mathbf{x}_\alpha(t), t) \quad (1.11)$$

is accurate [Yau & Rogers, 1989]. Here, $\mathbf{x}_\alpha(t)$ denotes the position of droplet α at time t . Furthermore, A_3 is a thermodynamic coefficient, accounting for the diffusion of water vapor to the surface of a droplet, as well as the delay of condensation caused by the latent heat that a condensating droplet releases. The thermodynamic coefficient A_3 depends on temperature and pressure, with typical cloud values ranging between $10 \mu\text{m}^2/\text{s}$ and $100 \mu\text{m}^2/\text{s}$ [Yau & Rogers, 1989]. Eq. (1.11) not only describes droplet growth, but also how a droplet shrinks, if it happens to reside within subsaturated air ($s < 0$) that causes it to evaporate.

In the derivation of Eq. (1.11), one assumes a quasisteady state in which the air is saturated at the surface of the droplet, and temperature and water vapor diffuse towards or away from the droplet at constant rates [Yau & Rogers, 1989]. The supersaturation $s(\mathbf{x}_\alpha(t), t)$ enters as the ambient supersaturation in this derivation, the supersaturation at distances from the position $\mathbf{x}_\alpha(t)$ of the droplet that are much larger than the radius $r_\alpha(t)$. This means that the supersaturation $s(\mathbf{x}, t)$ is only defined at length scales that are much larger than the micron-sized droplets [Srivastava, 1989].

Collective effect of phase-changing droplets

Condensating or evaporating droplets affect water-vapor density and temperature by exchanging water and latent heat with the surrounding air. The collective effects of many phase-changing droplets are described by the condensation rate,

$$C_d(\mathbf{x}, t) = \sum_{\alpha} G(|\mathbf{x} - \mathbf{x}_\alpha(t)|) \frac{dm_\alpha(t)}{dt}. \quad (1.12)$$

Here, the sum is over all droplets α in the system under consideration. Furthermore, $m_\alpha(t) = 4\pi\rho_p r_\alpha(t)^3/3$ is the mass of droplet α , computed using the density ρ_p of liquid water. The field description of the combined phase change of many locally present droplets is enabled through the kernel function $G(|\mathbf{x}|)$, which is normalized to unity. The condensation rate is positive at a given position if most nearby droplets grow by condensation, and negative if they shrink by evaporation.

The condensation rate $C_d(\mathbf{x}, t)$ appears in source terms in equations for temperature and water vapor. These source terms reflect the conservation of water and energy. Under the microscopic equations of Vaillancourt *et al.*

[2001] introduced in Section 1.1.2, the temperature and water-vapor density within a spatially uniform cloud at rest evolve according to

$$\frac{dT}{dt} = \frac{LQ}{\rho c_p} C_d \quad \text{and} \quad \frac{d\rho_v}{dt} = -C_d. \quad (1.13)$$

Here, the heat capacity c_p per unit mass of air at constant pressure is assumed constant. It is clear that this heat capacity changes when the amount of water vapor changes. However, the change in heat capacity is small, because only a small amount of the air is water vapor. The usage of c_p – rather than the constant-volume heat capacity c_v – can be motivated by that expanding air in the atmosphere pushes neighboring air away. But pushes clearly affect the air pressure, so the constant-pressure assumption can not be strictly true. Nevertheless, it is standard to assume constant heat capacities and work-free expansion in descriptions of phase changing cloud droplets [Jeffery, 2007; Vaillancourt *et al.*, 2001; Andrejczuk *et al.*, 2006; Pinsky *et al.*, 2016a; Kumar *et al.*, 2014; Perrin & Jonker, 2015; Sardina *et al.*, 2015].

As air rises and droplets form, condensation brings the air close to saturation, $s = 0$. As a consequence, the air in the core of a cloud is always saturated, or nearly saturated. The air outside the cloud tends to be subsaturated ($s < 0$), and it contains no droplets that can establish the saturated equilibrium. Near cloud edges, mixing between saturated air with droplets and subsaturated droplet-free air causes droplets to evaporate. Cloud-edge mixing and evaporation is the topic of Chapters 2 and 3. To describe droplet evaporation and mixing at cloud edges, it is necessary to account for variations in temperature, water-vapor density, and droplet content in the vicinities of individual droplets, and therefore on small spatial scales.

1.1.2 Microscopic equations of cloud dynamics

The air flow in a cloud carries temperature, water vapor and droplets along. The air velocity $\mathbf{u}(\mathbf{x}, t)$ is in turn affected by variations in temperature, water-vapor content and liquid-water content, because such variations imply density variations that are accelerated by gravity. Vaillancourt *et al.* [2001] proposed a set of fundamental microscopic equations for the dynamics of air and droplets in ice-free clouds. I refer to these equations as fundamental, because they describe cloud dynamics and thermodynamics in all detail that can be expected relevant for ice-free mixing and evaporation locally near and

within clouds. I refer to the equations as microscopic, because they describe every droplet and the smallest structures of velocity and scalar fields in full detail.

The equations of Vaillancourt *et al.* [2001] describe a volume of air that moves on top of a dry adiabatic atmosphere. It is cooled by expansion work if it moves upwards, and it is heated if it sinks. For purposes of this thesis, I consider local cloud systems at fixed altitude, and formulate the dynamical description of Vaillancourt *et al.* [2001] without this forcing:

$$\frac{\partial \mathbf{u}}{\partial t} + (\mathbf{u} \cdot \nabla) \mathbf{u} = -\frac{1}{\varrho_0} \nabla p' + \nu \nabla^2 \mathbf{u} - B \mathbf{g}, \quad (1.14a)$$

$$\nabla \cdot \mathbf{u} = 0, \quad (1.14b)$$

$$\frac{\partial \varrho_v}{\partial t} + (\mathbf{u} \cdot \nabla) \varrho_v = \kappa_v \nabla^2 \varrho_v - C_d, \quad \text{and} \quad (1.14c)$$

$$\frac{\partial T}{\partial t} + (\mathbf{u} \cdot \nabla) T = \kappa_T \nabla^2 T + \frac{L_Q}{\varrho_0 c_p} C_d - \Gamma_d u_z. \quad (1.14d)$$

Here, the kinematic viscosity ν of air, the gravitational acceleration \mathbf{g} , the diffusivity κ_v of water vapor, the diffusivity κ_T of temperature, the heat capacity c_p of air, the latent heat L_Q of water vapor, and the dry adiabatic lapse rate Γ_d are assumed constant. Also constant is the reference density ϱ_0 . It is the density of a dry adiabatic atmosphere at the altitude of the system considered. I denote the corresponding pressure and temperature by p_0 and T_0 , so that $p_0 = \varrho_0 R_a T_0$.

In Eq. (1.14a) $p'(\mathbf{x}, t)$ is the pressure deviation from p_0 . Furthermore $B = B(\mathbf{x}, t)$ is buoyancy,

$$B = \frac{T - \langle T \rangle}{T_0} + \frac{1}{\varrho_0} \left[\left(\frac{R_v}{R_a} - 1 \right) (\varrho_v - \langle \varrho_v \rangle) - \varrho_\ell \right], \quad (1.15)$$

where $\varrho_\ell = \varrho_\ell(\mathbf{x}, t)$ is the density of liquid water, and $\langle T \rangle$ and $\langle \varrho_v \rangle$ are time-dependent volume averages of temperature and water-vapor density, taken over the domain over which Eqs. (1.14) are solved. The buoyancy B is (minus) the linearized difference between the total density

$$\varrho_t = \varrho_a + \varrho_v + \varrho_\ell \quad (1.16)$$

and the average density of the air, divided by the reference density ϱ_0 .

In Eqs. (1.14c) and (1.14d) $C_d = C_d(\mathbf{x}, t)$ is the condensation rate, the change in liquid-water density that follows from that droplets evaporate or condensate. Both the liquid-water density and the condensation rate are computed from the droplets using a kernel function, as in Eq. (1.12). In Eq. (1.14d), $u_z = u_z(\mathbf{x}, t)$ is the upward component of the velocity $\mathbf{u}(\mathbf{x}, t)$. Vaillancourt *et al.* [2001] formulated the dynamics of Eqs. (1.14) using the water-vapor mixing ratio $q_v = \rho_v/\rho_0$ instead of the water-vapor density. Their formulation is however equivalent to the formulation in Eqs. (1.14) when it comes to describing cloud systems at fixed altitudes, because ρ_0 remains constant in them.

Eqs. (1.14a) and (1.14b) are Navier-Stokes equations in the Boussinesq approximation [Bannon, 1996]. They represent the conservation of mass and momentum. In the Boussinesq approximation, density variations are neglected everywhere, apart from in the buoyancy term. The flow is therefore incompressible, Eq. (1.14b). Eqs. (1.14c) and (1.14d) prescribe advection-diffusion equations for water-vapor density and temperature, with source terms accounting for effects of droplet phase change. The thermodynamics and dynamics of droplets, described in Sections 1.1.1 and 1.1.4, couple to the dynamics of air through these source terms. Vertical motion results in heating or cooling through the dry adiabatic lapse rate Γ_d , as dictated by the conditions of a dry adiabatic atmosphere.

The microscopic description of Vaillancourt *et al.* [2001] consists of Eqs. (1.14), and a set of equations that describe the motion, condensation, and evaporation of droplets. The authors performed DNS of their equations in 2002 [Vaillancourt *et al.*, 2002]. Many others have solved the same equations, or small variations of them, using DNS since then [Kumar *et al.*, 2014; Perrin & Jonker, 2015; Sardina *et al.*, 2015; Kumar *et al.*, 2017, 2018].

1.1.3 Turbulence

Turbulence, the chaotic motion that a flow exhibits if inertial stresses dominate over viscous stresses, causes cloud dynamics at widely separated spatial scales to be strongly coupled [Bodenschatz *et al.*, 2010]. A hallmark of turbulence is that the velocity field possesses structures over a range of spatial scales, commonly referred to as eddies. The range of eddy sizes corresponds to an energy cascade, in which kinetic energy is transferred downstream from large-scale eddies driving the flow, towards smaller and smaller eddies.

At the small-scale end of the cascade, kinetic energy dissipates into heat.

Kolmogorov's theory from 1941

A very useful theory that makes it possible to quantify central aspects of a turbulent flow is due Kolmogorov [1941]. The theory applies directly to incompressible flows with constant density ϱ_0 ,

$$\frac{\partial \mathbf{u}}{\partial t} + (\mathbf{u} \cdot \nabla) \mathbf{u} = -\frac{1}{\varrho_0} \nabla p + \nu \nabla^2 \mathbf{u} \quad \text{and} \quad (1.17a)$$

$$\nabla \cdot \mathbf{u} = 0, \quad (1.17b)$$

but is widely used to analyze cloud motion as well, despite that buoyancy effects may be important [Devenish *et al.*, 2012; Andrejczuk *et al.*, 2004; Lehmann *et al.*, 2009]. As a starting point for my introduction of the theory, we note that a flow problem on the length scale \mathcal{L} and the velocity scale \mathcal{U} exhibits two scales for inertial and viscous stresses. The viscous scale $\varrho_0 \nu \mathcal{U} / \mathcal{L}$ depends on the viscosity of the fluid, but the inertial scale $\varrho_0 \mathcal{U}^2$ does not. Their ratio forms the Reynolds number

$$\text{Re} = \frac{\mathcal{U} \mathcal{L}}{\nu}. \quad (1.18)$$

If the Reynolds number is very large, the nonlinear term $(\mathbf{u} \cdot \nabla) \mathbf{u}$ dominates over the viscous term $\nu \nabla^2 \mathbf{u}$ in Eq. (1.17a). This is what causes the flow to be turbulent.

Kolmogorov's theory recognizes that motion at large scales are unique to each flow, but assumes that the chaotic motion of turbulence causes large scale motion to be forgotten in the energy cascade towards small scales. As a consequence, statistics describing local motion at small-enough spatial scales are of the same form in all high-Reynolds number flows. The range of scales that exhibits this universal form is called the universal equilibrium range. Motion at the spatial scale ℓ belong to this range if ℓ is smaller than a certain length that I denote by ℓ_E . Large-scale motion at spatial scales $\ell > \ell_E$ contains most of the kinetic energy, and belong to the flow-specific energy-containing range. Kolmogorov's theory predicts that all local statistics at a spatial scale ℓ within the universal equilibrium range are determined by ℓ , together with the mean energy dissipation rate ε and the kinematic viscosity ν . This determines the Kolmogorov scales, the scales that characterize the

smallest eddies of the flow. The Kolmogorov length, time, and velocity are given by:

$$\eta = \left(\frac{\nu^3}{\varepsilon} \right)^{\frac{1}{4}}, \quad \tau_\eta = \left(\frac{\nu}{\varepsilon} \right)^{\frac{1}{2}}, \quad \text{and} \quad u_\eta = (\varepsilon \nu)^{\frac{1}{4}}. \quad (1.19)$$

Furthermore, Kolmogorov's theory predicts that the universal equilibrium range is separated into two subranges by a length $\ell_D \sim \eta$. Motion at spatial scales $\ell < \ell_D$ belongs to the dissipative range, and motion at spatial scales $\ell > \ell_D$ belongs to the inertial range. Kinetic energy dissipates into heat within the dissipative range only. Within the inertial subrange, viscous effects are negligible, and the characteristic time and velocity of an eddy of length ℓ are given by

$$\tau_\ell \sim \left(\frac{\ell^2}{\varepsilon} \right)^{\frac{1}{3}}, \quad \text{and} \quad u_\ell \sim (\varepsilon \ell)^{\frac{1}{3}}. \quad (1.20)$$

The largest scales of the inertial range are constrained by the size of the flow. With $\mathcal{L} \sim \ell_E$ and $\mathcal{U} \sim u_{\ell_E}$, Eqs. (1.18) to (1.20) yield

$$\frac{\eta}{\ell_E} \sim \text{Re}^{-\frac{3}{4}}, \quad \frac{\tau_\eta}{\tau_{\ell_E}} \sim \text{Re}^{-\frac{1}{2}} \quad \text{and} \quad \frac{u_\eta}{u_{\ell_E}} \sim \text{Re}^{-\frac{1}{4}}. \quad (1.21)$$

This tells us that the extent of the inertial range increases with Reynolds number.

Kolmogorov's theory has been shown to give many accurate predictions [Pope, 2000]. One example is the form of the energy spectrum – the kinetic energy $E(k)$ per wave number $k = 2\pi/\ell$ – within the universal equilibrium range. Within the inertial range, the theory predicts that the spectrum takes the form of a power law,

$$E(k) = C_K \varepsilon^{\frac{2}{3}} k^{-\frac{5}{3}}, \quad (1.22)$$

where C_K is a constant. Furthermore, the theory predicts that the compensated spectrum

$$\mathcal{E} = E(k) k^{\frac{5}{3}} / \varepsilon^{\frac{2}{3}} \quad (1.23)$$

is independent of the large-scale Reynolds number, and universally determined by $k\eta$ for all k within the universal equilibrium range. Fig. (1.2) shows

DNS results from Ishihara *et al.* [2009], confirming this prediction. The compensated energy spectrum is plotted for three different values of the Taylor-scale Reynolds number Re_λ , which scales as the square root of the large-scale Reynolds number Re in Eq. (1.18), $Re_\lambda \sim \sqrt{Re}$. The leftmost parts of the spectra are not universal. They belong to the energy-containing range. Above this range, the spectra are very similar. This suggests that they adhere to the universality predicted by Kolmogorov [1941]. Indeed, the range of scales contained within the spectra increases with Re . Fig. (1.2) also indicates that the power law-spectrum of Eq. (1.22) is quite accurate. Just above the energy-containing range, the compensated spectra are roughly flat, suggesting the existence of an inertial range with $k^{-5/3}$ scaling. Based on spectra of this type, Ishihara *et al.* [2009] conclude that the constant C_K in Eq. (1.22) is between 1.5 and 1.7. The dashed line in Fig. (1.2) indicates $C_K = 1.6$.

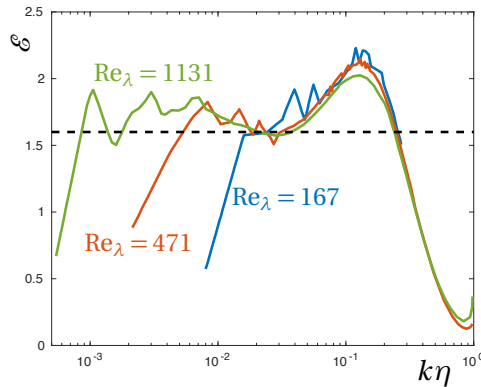


Figure 1.2: Compensated energy spectra, data from Ishihara *et al.* [2009]. The spectra are computed from DNS of statistically stationary turbulence within a cubic domain with periodic boundary conditions. Solid lines are for different Taylor-scale Reynolds numbers $Re_\lambda \sim \sqrt{Re}$. The dashed line is the power-law spectrum of Eq. (1.22), for $C_K = 1.6$.

Inaccuracies and refinements of the 1941 theory

The theory of Kolmogorov [1941] makes it possible to quantify central aspects of the turbulent energy cascade, but it is not strictly correct. In inhomogeneous flows, flow-specific large-scale motion is not completely forgotten, and make flow-specific imprints on small-scale statistics [Pope, 2000]. Even

under homogeneous conditions, some turbulence statistics are not well described by the theory. The theory is quite accurate for the first and second moments of the velocity field, but it fails to predict higher-order statistics [Pope, 2000]. To describe the higher-order statistics, it is important to account for intermittent fluctuations of the instantaneous dissipation rate $\varepsilon'(\mathbf{x}, t)$ around the mean dissipation rate ε . Flow statistics are Reynolds-number dependent, as a consequence of this intermittency. The effects of intermittency are largely accounted for by Kolmogorov's refined theory from 1962 [Kolmogorov, 1962].

1.1.4 Particle dynamics

The particles considered in this thesis are water droplets and rigid non-spherical particles. They have uniform mass densities ρ_p . Their translational acceleration is given by

$$m \frac{d\mathbf{v}^{(c)}}{dt} = m \mathbf{g} + \mathbf{F} - \rho V \mathbf{g}, \quad (1.24)$$

where \mathbf{F} is the hydrodynamic force exerted by the flow, and $\mathbf{v}^{(c)}$ is the center-of-mass velocity. Furthermore, V and $m = \rho_p V$ are particle volume and mass. The density ρ is the density of the suspending fluid, which is air in the case of cloud droplets. Eq. (1.24) is simply Newton's second law for a particle subject to gravitation and hydrodynamic force. The last term on the right-hand side of Eq. (1.24) follows from Archimedes' principle. It is the lifting force that equals the gravitational force upon the fluid displaced by the particle. Cloud droplets consist of liquid water, which is a factor ~ 1000 heavier than air, $m \gg \rho V$. The lifting force is therefore very small for cloud droplets, and can be neglected. The rigid particles considered in Chapter 4 are neutrally buoyant. This means that $m = \rho V$ for them, so that the first and last terms on the right-hand side of Eq. (1.24) cancel.

To describe the angular dynamics of the rigid particles considered in Chapter 4, I introduce their angular velocities $\boldsymbol{\omega}$. The motion of a point \mathbf{x}' in the reference frame of a particle is then given by

$$\frac{d\mathbf{x}'}{dt} = \mathbf{v}^{(c)} + \boldsymbol{\omega} \times (\mathbf{x}' - \mathbf{x}^{(c)}), \quad (1.25)$$

where $\mathbf{x}^{(c)}$ is the particle's center of mass. The hydrodynamic torque with respect to the center of mass is denoted by $\boldsymbol{\tau}^{(c)}$. The angular acceleration is given by

$$\frac{d}{dt} \mathbb{I}^{(c)} \boldsymbol{\omega} = \boldsymbol{\tau}^{(c)}, \quad (1.26a)$$

where $\mathbb{I}^{(c)}$ is the inertia tensor of the particle, evaluated at the particle's center of mass [Marion, 2013]. The particles considered in Chapter 4 are neutrally buoyant, and so small that their inertia is negligible. Their dynamics is therefore overdamped. This means that the particles instantaneously relax to a motion for which their torques and forces vanish [Kim & Karrila, 1991]. It is nevertheless useful to imagine a small particle at rest, and compute its force \mathbf{F} and torque $\boldsymbol{\tau}^{(c)}$. The reason is that the translational and angular dynamics can be inferred from the resulting non-zero values of \mathbf{F} and $\boldsymbol{\tau}^{(c)}$, as explained in Chapter 4.

Stokes equations

To calculate the force and torque upon a small particle in flow, it is important to recognize that very small particles tend to follow the flow. They are so light that settling and inertial effects are efficiently dampened by hydrodynamic action. The velocity scale \mathcal{U} characterizing velocity differences in the vicinity of a particle is therefore small. Since the length scale \mathcal{L} is comparable to the particle size, it follows that the Reynolds number [Eq. (1.18)] of the local flow around the particle is small. Viscous stresses therefore dominate over inertial stresses in the vicinity of the particle.

In the limit of zero Reynolds number, the viscous term $\nu \nabla^2 \mathbf{u}$ dampens all effects of the nonlinear term $(\mathbf{u} \cdot \nabla) \mathbf{u}$ in Navier-Stokes equations (1.17), and one obtains Stokes equations,

$$\frac{1}{\rho} \nabla p = \nu \nabla^2 \mathbf{u} \quad , \quad \text{and} \quad (1.27a)$$

$$\nabla \cdot \mathbf{u} = 0. \quad (1.27b)$$

A solution to Stokes equations is determined by boundary conditions. When a particle is present, boundary conditions are required at the particle surface. The force and torque upon a small-enough particle can therefore be computed by solving the Stokes problem that the presence of the particle

implies. As opposed to Navier-Stokes equations, Stokes equations are linear. In Chapter 4 I explain how the linearity makes it possible to derive the form of the angular dynamics of small particles that possess symmetries without solving their Stokes problems.

Droplets in clouds

A Stokes problem of high relevance for cloud physics is that presented by a translating sphere with no-slip boundary conditions. The solution gives the force and torque upon a micron-sized cloud droplet. The force is independent of the rotation of the droplet, and called Stokes drag. For a droplet with center-of-mass position $\mathbf{x}^{(c)}$ and radius r , translating with the velocity $\mathbf{v}^{(c)}$, it is given by

$$\mathbf{F} = 6\pi\varrho \nu r [\mathbf{u}(\mathbf{x}^{(c)}, t) - \mathbf{v}^{(c)}]. \quad (1.28)$$

Together with Eq. (1.24) one obtains the acceleration of the droplet,

$$\frac{d\mathbf{v}^{(c)}}{dt} = \frac{1}{\tau_p} [\mathbf{u}(\mathbf{x}^{(c)}, t) - \mathbf{v}^{(c)}] + \mathbf{g}, \quad (1.29)$$

where $\tau_p = 2r^2\varrho_p/9\varrho\nu$ is Stokes relaxation time: the time scale at which the droplet relaxes to the velocity of the surrounding air in the absence of gravity. Eq. (1.29) is derived using that the density ϱ_p of a droplet is much larger than the density of air, $\varrho_p \gg \varrho$.

Effects of droplet inertia are described by the Stokes number:

$$\text{St} = \frac{\tau_p}{\tau_\eta}. \quad (1.30)$$

The Stokes number of a droplet is the ratio between its Stokes relaxation time and the smallest time scale of the turbulent flow that carries it. Accordingly, at small St and in the absence of gravity, the droplet quickly adopts the velocity of the surrounding air.

Gravity causes droplets to settle. A force balance between gravitation and hydrodynamic drag in quiescent flow ($\mathbf{u} = \mathbf{0}$) gives the settling velocity of a droplet,

$$\mathbf{v}_s = \tau_p \mathbf{g}, \quad (1.31)$$

the velocity that a droplet adopts in an atmosphere at rest. Flow detachment due to settling is described by the settling number,

$$Sv = \frac{|\boldsymbol{v}_s|}{u_\eta}. \quad (1.32)$$

At small values of Sv , the gravitational settling is efficiently dampened by Stokes drag force, Eq. (1.28).

Consistently with that micron-sized cloud droplets detach little from the surrounding flow, the Stokes and settling numbers of a droplet whose radius r is a few microns are smaller than unity. For typical cloud conditions ($\varepsilon \sim 10^{-3} \text{ m}^2/\text{s}^3$, $\nu \sim 1.5 \times 10^{-5} \text{ m}^2/\text{s}$) [Shaw, 2003], one finds $St \sim 10^{-4} (r/\mu\text{m})^2$ and $Sv \sim 10^{-2} (r/\mu\text{m})^2$. One also finds that the Reynolds number based on the radius and settling velocity of the droplet is $Re \sim 10^{-5} (r/\mu\text{m})^3$. Since the Reynolds number is much smaller than unity for micron-sized droplets, their acceleration is found by solving the Stokes problem of a translating sphere, and given by Eq. (1.29). Their small Stokes numbers suggest that their inertia does not cause them to detach much from the flow. Settling can however be important, because some droplets have settling numbers near unity.

1.1.5 Modeled cloud-edge dynamics

Important parts of our understanding of clouds relies on models of mixing and evaporation at cloud edges [Mellado, 2017]. Fundamental microscopic equations, such as the equations of Vaillancourt *et al.* [2001] in Section 1.1.2, are too computationally expensive to solve for cloud systems that exceed a few meters in linear size. Numerical simulations of whole clouds can therefore not resolve cloud dynamics in full detail. Instead, whole-cloud simulations rely on models of small-scale processes. An important work in cloud physics is to improve models for mixing-evaporation dynamics, so that effects of mixing and evaporation at the cloud edge can be described more accurately [Mellado, 2017].

The high computational cost that DNS of microscopic equations entail for large turbulent cloud systems can be avoided in two different ways. One may either model statistics of an ensemble of independent flow realizations, or consider a single realization and filter the velocity field so that the smallest eddies are not resolved [Pope, 2000]. Models that employ the latter approach are called large-eddy simulations (LES), and I refer to models that employ

the former approach as statistical models. A LES relies on closure approximations that describe effects of unresolved eddies. Different types of statistical models employ different probabilistic descriptions, and rely on different types of closure approximations as a consequence. Important types of statistical models are Reynolds-averaged Navier-Stokes (RANS) models, and probability-density function (PDF) models. RANS models describe only a few moments of the velocity field, and rely on closures for Reynolds stresses or for a turbulent viscosity. PDF models describe the full joint PDF of velocity components, and rely on models for velocity and pressure gradients [Pope, 2000]. LES and statistical models can describe flows with scalars, such as temperature and water-vapor density. The models then rely on additional closures for the scalar dynamics.

Models for mixing and evaporation that incorporate the linear eddy model of Kerstein [1988] are interesting alternatives or complements to the model types above [Krueger, 1993; Su *et al.*, 1998; Tölle & Krueger, 2014; Hoffmann & Feingold, 2019]. In such models, effects of turbulent mixing are described by repeated stretchings and foldings of a one-dimensional map. Droplets can be carried along with the map, in order to describe the fragmentation of cloud structures caused by turbulence. An important advantage of these models is that they describe how cloud structures of arbitrary sizes within the universal equilibrium range of turbulence evolve, because they rest on well-understood scaling arguments [Kerstein, 1988]. The main drawback is however that they lack a definite interpretation in terms of a microscopic description.

All types of models face difficulties when describing droplets in a cloud [Shima *et al.*, 2009; Paoli & Shariff, 2009]. RANS models are very problematic, because the flow that accelerates the droplets and the supersaturations that causes them to change phase are not available under their statistical descriptions. LES can describe how droplets are carried by large eddies, but they can neither describe the small-scale motion of droplets, nor the supersaturations at droplet positions. Furthermore, it is not computationally possible to describe every droplet that large a cloud systems contains individually. One way to circumvent this problem is to describe the effects and presence of many droplets by a single superdroplet that has one position and one size [Grabowski *et al.*, 2019]. A fundamental limitation of this approach is however that droplet dispersion and different evaporation and condensation rates become difficult to describe [Hoffmann & Feingold, 2019]. PDF models

can describe the supersaturations of individual droplets statistically, if they incorporate droplets into their statistical descriptions [Jenny *et al.*, 2012]. Chapter 2 introduces Paper A. Here, a statistical model for cloud-edge dynamics that belongs to the family of PDF models is derived. It incorporates droplets into its statistical description, and describes the supersaturations of individual droplets. An improved version of the model that quantitatively reproduces the supersaturations of droplets in DNS is presented in Chapter 3.

The drawbacks of PDF models stem from that they describe flow and droplets in terms of one-point, one-time, statistics [Pope, 2000; Jeffery & Reisner, 2006]. Consider, for instance, a PDF model that describes droplets using the probability density

$$\mathcal{F}_{sr^2}(S, R^2; t) = \frac{\partial^2}{\partial S \partial R^2} F_{sr^2}(S, R; t), \quad (1.33)$$

where $F_{sr^2}(S, R; t)$ is the probability that a droplet α has a radius $r_\alpha(t) < R$ and a supersaturation $s(\mathbf{x}_\alpha(t), t) < S$ ¹. The PDF \mathcal{F}_{sr^2} is a one-point, one-time, statistic for the instantaneous state of a single droplet. It does not describe the coherent spatial distributions of droplets that form as a consequence of that droplets are carried together, by the same flow. It is therefore not possible to account for how many phase-changing droplets collectively maintain saturation within large cloud structures using \mathcal{F}_{sr^2} .

It should be noted that the exchange of water and latent heat between air and phase-changing droplets can not be described in terms of \mathcal{F}_{sr^2} alone, because this PDF does not describe the air. It is however possible to describe the air using a second PDF, such as the probability density

$$f_s(S; \mathbf{x}, t) = \frac{\partial}{\partial S} F_s(S; \mathbf{x}, t), \quad (1.34)$$

where $F_s(S; \mathbf{x}, t)$ is the probability of $s(\mathbf{x}, t) < S$, i. e. the probability that the supersaturation of the air is smaller than S at the position \mathbf{x} . To describe a system using two PDFs is common in combustion studies, where dispersed particles react with a gas [Jenny *et al.*, 2012]. The statistical model in Chapter 3 is of this type, and it rests on a probabilistic description in terms of \mathcal{F}_{sr^2} and

¹The reason that I define \mathcal{F}_{sr^2} as a density in squared radius $r_\alpha(t)^2$ in Eq. (1.33), instead of radius $r_\alpha(t)$, is that it is often more convenient to analyze the evolution of probability densities in squared droplet radius [Siewert *et al.*, 2017; Paper A].

f_s . The statistical model in Paper A is also of this type, but it rests on a more comprehensive probabilistic description.

To understand the statistical model in Chapter 3, it is important to recognize that the PDF:s \mathcal{F}_{sr^2} and f_s are of two different types. The PDF \mathcal{F}_{sr^2} is evaluated along the trajectories of droplets, whereas f_s is evaluated at fixed positions. PDF:s of the former type are called *Lagrangian*, whereas PDF:s of the latter type are called *Eulerian* [Pope, 2000]. In the remainder of this thesis, I refer to (the Lagrangian) \mathcal{F}_{sr^2} as the joint PDF of droplets and supersaturation, and I refer to f_s as the Eulerian supersaturation PDF.

PDF models can be formulated as Lagrangian stochastic models for independently evolving droplets and fluid elements. Consider, for instance, a Lagrangian stochastic model for the supersaturation $s_\alpha(t) = s(\mathbf{x}_\alpha(t), t)$ and radius $r_\alpha(t)$ of droplet α . The Fokker-Planck equation [Pope, 2000] that corresponds to the stochastic dynamics is a modeled evolution equation for \mathcal{F}_{sr^2} . In a similar way, a modeled evolution equation for f_s can be obtained from a Lagrangian stochastic model for fluid elements with supersaturation $s(t)$ [Pope, 2000].

Several models describe cloud dynamics using Lagrangian stochastic models [Sardina *et al.*, 2015; Paoli & Shariff, 2009; Chandrakar *et al.*, 2016; Siewert *et al.*, 2017; Grabowski & Abade, 2017; Abade *et al.*, 2018]. These models can generally be brought into the framework of PDF models, by formulating their corresponding Fokker-Planck equations. But this step is often omitted, likely because the models are best understood through their stochastic dynamics. It is however important to consider their corresponding PDF formulations. One reason is that the PDF formulations give the models definite interpretations in terms of a microscopic dynamics. The microscopic connection is provided, because stochastic and deterministic terms in Lagrangian equations constitute models for conditional averages in exact, but unclosed, evolution equations of PDF:s [Pope, 1985]. This notion resolves the apparent contradiction that droplets and fluid elements evolve independently in Lagrangian stochastic models, despite that they do not under microscopic descriptions [Pope, 2000]. PDF formulations can also provide means to improve the accuracy of models [Pope, 1991]. In the statistical model formulated in Chapter 3, I make use of the PDF formulation of the model to derive an accurate closure for effects of droplet phase change.

A third reason for considering the PDF formulation of a Lagrangian stochastic model is that it provides a link to the theory on filtered-density function

(FDF) modeling [Colucci *et al.*, 1998; Givi, 2006]. An FDF is essentially a PDF for unresolved quantities in a LES. FDF models are therefore closely related to PDF models, and used in combination with LES. A LES-FDF model makes use of the strengths of LES when it comes to describing correlated motion at large spatial scales, while an FDF model is used to account for reactions and fluctuations at small spatial scales. LES-FDF models have mostly been developed within the combustion community, but there are many parallels to LES models for clouds. FDF models are for instance solved using Lagrangian stochastic models coupled to LES, so the solution algorithms of LES-FDF models are analogous to cloud LES with superdroplets [Grabowski *et al.*, 2019].

2 Mixing and evaporation at the cloud edge

In Paper A we analyze the effects of mixing and evaporation at the edge of a turbulent cloud, where the cloud is mixed with its environment. Since the environmental air tends to be subsaturated, droplets evaporate when they are exposed to it. Mixing and evaporation at the cloud edge affect both the droplet-size distribution and the number density of droplets. The droplet-size distribution shifts towards smaller droplet sizes locally where droplets evaporate. It should however be noted that secondary effects of evaporation may give rise to large droplets elsewhere in the cloud [Lasher-Trapp *et al.*, 2005]. Mixing with environmental air can cause the droplet-number density to reduce through two mechanisms. First, a reduction in droplet-number density follows from that cloudy air is diluted by non-cloudy air [Devenish *et al.*, 2012]. Second, the droplet-number density may reduce because some droplets evaporate completely and vanish [Baker *et al.*, 1980].

2.1 Background

The cloud edge is a non-equilibrium system located between the core of the cloud and the air outside the cloud. Compared to the cloud edge, the cloud core is essentially equilibrated. Here, droplet phase change is comparatively slow, because the air is saturated or nearly saturated [Yau & Rogers, 1989]. Mixing throws droplet populations near the cloud edge out of their equilibria, by exposing them to subsaturated air from outside the cloud. The droplets within a given volume may then evaporate until one out of two possible steady states establishes. A moist steady state establishes if the droplets saturate the surrounding air, and a dry steady state establishes if all droplets evaporate completely and leave subsaturated air behind [Kumar *et al.*, 2013]. Turbulence ensures that neighboring droplet populations have different histories of mixing and evaporation. Cloud-edge mixing and evaporation therefore gives rise to spatial fluctuations throughout the cloud [Beals *et al.*, 2015].

Fluctuations caused by mixing with non-cloudy air has been suggested as a resolution of the bottleneck problem of droplet growth [Grabowski & Wang, 2013], because such fluctuations may allow a small fraction of droplets to grow fast enough [Beard & Ochs, 1993]. Fast droplet growth can be ob-

tained in a turbulent cloud with a varying droplet-number density, because turbulence ensures that droplet trajectories reaching the cloud top are not monotonous ascents. If a small fraction of droplets rises with few neighboring droplets and sink with many neighboring droplets, their competition for water vapor is reduced when they rise, but they can not give away much water when they sink [Telford & Chai, 1980]. It has been suggested that this mechanism is responsible for 60μ droplet radii observed in ice free clouds [Beard & Ochs, 1993], well beyond the size thought to be necessary to initiate droplet growth by collision [Yau & Rogers, 1989].

Moist regions with few droplets allowing for fast droplet growth can be generated through complete droplet evaporation [Yang *et al.*, 2016]. In regions where complete evaporation has taken place, droplets grow upon vertical ascent, by consuming the water vapor that once constituted their neighbors. The growth may be fast, because the vanished neighbors no longer participate in the competition for water vapor. Mechanisms of this type, where fast droplet growth follows from reduced competition for water vapor, have therefore been tied to a mixing-evaporation regime where evaporation distributes inhomogeneously over the droplets that are mixed [Baker *et al.*, 1980; Desai *et al.*, 2019]. In this mixing-evaporation regime – called inhomogeneous mixing – a moist steady state can establish by some droplets evaporating completely, while other droplets do not evaporate at all. In the opposing limit – called homogeneous mixing – all droplets share the work of saturating the air, and only initially small ones evaporate completely. It has been argued that the degree of inhomogeneous mixing increases with the spatial scale of a droplet population, since large-scale cloud regions are mixed into homogeneity more slowly than small ones [Devenish *et al.*, 2012]. A simple observable that is closely related to the dichotomy of homogeneous and inhomogeneous mixing is the fraction P_e^* of droplets that have evaporated completely in the steady state.

The dichotomy of homogeneous and inhomogeneous mixing is also relevant for the optical properties of clouds [Beals *et al.*, 2015]. Many small droplets interact more with light than a few small ones with the same liquid water content. As a consequence, modeled cloud systems reflect more solar radiation back into space if local mixing is assumed to be homogeneous, than if it is assumed to be inhomogeneous [Grabowski, 2006]. Assuming a spatially uniform droplet configuration, the intensity of solar radiation decays exponentially with a rate that is proportional to the droplet-number

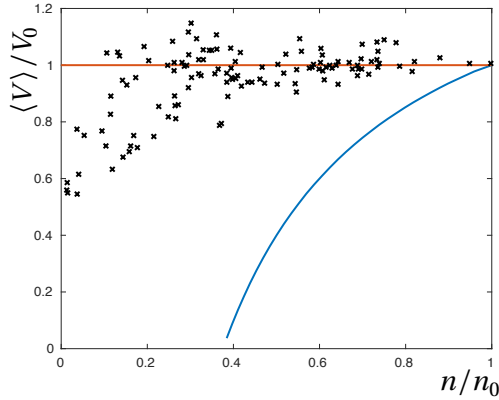


Figure 2.1: Example of a mixing diagram, empirical data and mixing lines from Beals *et al.* [2015]. Black crosses are mean droplet volumes $\langle V \rangle$ and droplet-number densities n measured in a convective cloud. The axes are normalized by a mean droplet volume V_0 and a droplet-number density n_0 , representative of undiluted cloud. The blue line is the homogeneous mixing line, and the red line is the inhomogeneous mixing line.

density and the average surface area of droplets [Kokhanovsky, 2004]. Jeffery [2007] found that the depth to which solar radiation penetrates a cloud – the clouds optical thickness – may be 50 % larger under inhomogeneous mixing than under homogeneous mixing.

Empirical cloud data are often related to the concepts of homogeneous and inhomogeneous mixing in mixing diagrams [Devenish *et al.*, 2012]. Mixing diagrams show the mean droplet volume $\langle V \rangle$ versus the droplet-number density n for locally measured droplet populations. The axes are normalized by a droplet volume V_0 and a droplet-number density n_0 , both assumed representative of a cloudy mixing substrate from which the locally measured droplet populations originate. An example is shown in Fig. (2.1), where I plotted empirical data from Beals *et al.* [2015] as crosses. The data represents droplets within $\sim 15 \text{ cm}^3$ volumes along a few kilometers long flight through a convective cloud. I also drew the homogeneous and inhomogeneous mixing lines [Devenish *et al.*, 2012] from Beals *et al.* [2015]. The inhomogeneous mixing line describes droplet populations that have resided in the cloudy mixing substrate, and undergone mixing processes that caused their droplet-number densities to reduce by dilution and complete droplet evaporation in such a way that their mean droplet volume remained the same. The homo-

geneous mixing line describes droplet populations that have been diluted by droplet-free air and adopted moist steady states (n^* , $\langle V \rangle^*$) without any complete droplet evaporation ($P_e^* = 0$).

In the last years, several studies have analyzed local mixing-evaporation processes within a fixed domain using computer simulations [Jeffery, 2007; Andrejczuk *et al.*, 2006; Pinsky *et al.*, 2016a; Kumar *et al.*, 2014, 2018; Andrejczuk *et al.*, 2004; Kumar *et al.*, 2013; Andrejczuk *et al.*, 2009; Kumar *et al.*, 2012; Pinsky & Khain, 2018]. It has however not been clear which parameters that are most important for the local mixing-evaporation processes.

2.2 My work

In Paper A, we adopt the model configuration of Kumar *et al.* [2014, 2018, 2013, 2012]. A slab of cloudy air with droplets is turbulently mixed with subsaturated air within a cubic domain of size L with periodic boundary conditions. We take the flow to be statistically stationary homogeneous isotropic turbulence, as in Kumar *et al.* [2013, 2012]. The initial conditions are schematically illustrated in Fig. (2.2). Before mixing, the cloud slab occupies a volume fraction χ of the domain. While the air masses are mixed, the droplets evaporate in response to the supersaturation at their positions. With time, mixing causes the system to become spatially uniform. Evaporation proceeds either until the entire domain is saturated (moist steady state), or until all droplets have evaporated completely (dry steady state). We follow Kumar *et al.* [2014, 2018, 2013, 2012] and address the dichotomy of homogeneous and inhomogeneous mixing using this model configuration.

2.2.1 Key parameters

In Paper A, we conclude that several DNS results of Kumar *et al.* [2014, 2018, 2013, 2012], as well as results obtained using other models for mixing and evaporation [Jeffery, 2007; Andrejczuk *et al.*, 2006; Pinsky *et al.*, 2016a], can be understood in terms of two or three key parameters. To arrive at this conclusion, we start by analyzing under which conditions one may simplify the fundamental microscopic equations of Vaillancourt *et al.* [2001]. We find that droplet inertia and settling, buoyancy, non-linear dependency of supersaturation on temperature and water-vapor density, expansion work upon vertical air motion, and temporal variations of thermodynamic coefficients

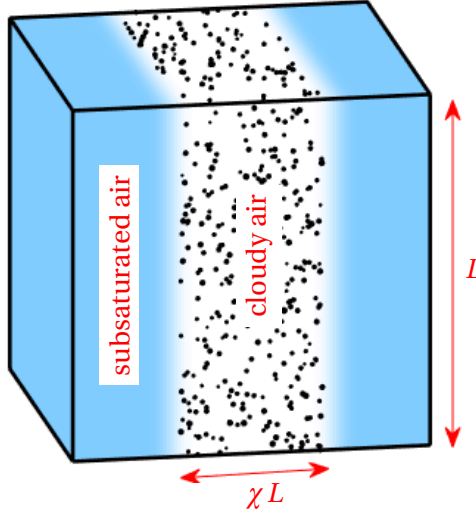


Figure 2.2: Initial condition used in Paper A: A slab of cloudy air with droplets is surrounded by subsaturated air in a cubic domain with side length L . The cloud slab occupies a volume fraction χ of the domain.

tend to be of secondary importance for the understanding of local cloud systems. Neglecting these ingredients of mixing-evaporation dynamics, we derive a set of simplified microscopic equations:

$$\frac{\partial \mathbf{u}}{\partial t} + (\mathbf{u} \cdot \nabla) \mathbf{u} = -\frac{1}{\rho_0} \nabla p + \nu \nabla^2 \mathbf{u}, \quad (2.1a)$$

$$\nabla \cdot \mathbf{u} = 0, \quad (2.1b)$$

$$\frac{\partial s}{\partial t} + (\mathbf{u} \cdot \nabla) s = \kappa \nabla^2 s - A_2 C_d(\mathbf{x}, t), \quad (2.1c)$$

$$\frac{d\mathbf{x}_\alpha}{dt} = \mathbf{u}(\mathbf{x}_\alpha(t), t) \quad \text{and} \quad (2.1d)$$

$$\frac{dr_\alpha^2}{dt} = 2A_3 s(\mathbf{x}_\alpha(t), t). \quad (2.1e)$$

Here, κ denotes the diffusivity of supersaturation. The condensation rate $C_d(\mathbf{x}, t)$ is given by Eq. (1.12), supplemented by Eq. (2.1e) to compute the rate at which the mass m_α of droplet α changes. See the Supporting Information of Paper A for the derivation of Eqs. (2.1).

Non-dimensionalizing the simplified equations (2.1), we find that the

dynamics is parameterized by two Damköhler numbers [Dimotakis, 2005] in the limit of large Reynolds numbers, Da_d and Da_s . The Damköhler numbers are time-scale ratios,

$$Da_d = \frac{\tau_L}{\tau_d}, \quad \text{and} \quad Da_s = \frac{\tau_L}{\tau_s}. \quad (2.2)$$

They relate the kinematic time scale τ_L of mixing to two thermodynamic time scales: the time scale τ_d of droplet evaporation [Andrejczuk *et al.*, 2009], and the time scale τ_s of supersaturation relaxation [Kumar *et al.*, 2018]. The time scale τ_L is the large-eddy turnover time. It is the time scale at which the system is stirred once. This time scale increases with the size of the system, and decreases with the intensity of the turbulence, $\tau_L \sim (L^2/\varepsilon)^{1/3}$. The droplet evaporation time τ_d is the time that it takes for a typical droplet to evaporate completely, if it is placed in the subsaturated air outside the initial cloud slab [Fig. (2.2)]. It increases with the initial droplet size, and decreases with increasing levels of subsaturation outside the cloud slab. The supersaturation relaxation time τ_s is a time scale at which the supersaturation relaxes towards saturation in a spatially uniform mixture. It decreases with the initial droplet size, and with the droplet-number density of the initial cloud slab.

At large values of Da_d , droplets evaporate faster than the system is mixed. Evaporation is then limited by the rate of mixing, and takes place at sharp boundaries between cloudy and subsaturated air. Mixing is inhomogeneous, because evaporation distributes inhomogeneously over the droplets. At small values of Da_d , droplets tend to evaporate after the system has been mixed. They then evaporate under spatially uniform conditions, and the mixing is homogeneous. At large values of Da_s , saturation of the air is mixing limited and takes place at sharp boundaries between cloudy and subsaturated air. At small values of Da_s , saturation takes place under spatially uniform conditions, but only if droplets remain. We could show in Paper A that droplet-size distributions and steady-state fractions in the DNS of Kumar *et al.* [2014, 2018, 2013, 2012], computed with DNS of fundamental microscopic equations, can be well understood in terms of Da_d and Da_s only.

The amount of complete evaporation depends on Da_d and Da_s , but also on the initial volume fraction χ of cloudy air. This means that there are three key parameters for the transition between homogeneous and inhomogeneous mixing. Kumar *et al.* [2014, 2018, 2013, 2012] did not vary χ

considerably, so their results can be understood in terms of Da_d and Da_s only. Dynamics and initial conditions are conveniently parameterized by Da_d , χ , and the Damköhler-number ratio

$$\mathcal{R} = \frac{Da_d}{Da_s}, \quad (2.3)$$

which regulates the moisture of the mixing-evaporation process. At large values of \mathcal{R} , all droplets evaporate completely before they saturate the air, and the system ends up in a dry steady state. At small values of \mathcal{R} , the air becomes completely saturated before much evaporation has taken place, and the system ends up in a moist steady state. In Fig. 4 of Paper A, we show how the steady-state fraction P_e^* of completely evaporated droplets varies with \mathcal{R} and Da_d . More droplets evaporate completely with increasing values of Da_d , because the mixing becomes more inhomogeneous. The amount of complete droplet evaporation increases with \mathcal{R} up to a critical Damköhler-number ratio \mathcal{R}_c , above which dry steady states are obtained. With a simple form of the initial conditions, the critical Damköhler-number ratio is given by:

$$\mathcal{R}_c = \frac{2}{3} \frac{\chi}{1 - \chi}. \quad (2.4)$$

The Damköhler numbers Da_d and Da_s , and the volume fraction χ , have been considered in many previous studies [Baker *et al.*, 1980; Andrejczuk *et al.*, 2006; Kumar *et al.*, 2014; Lehmann *et al.*, 2009], but not as the only parameters of a microscopic dynamics. C. A. Jeffery found that a model for mixing and evaporation is determined by Da_d , Da_s and χ already in 2007 [Jeffery, 2007]. Later results have however not been analyzed in light of this finding. The most likely reason is that it has not been clear in which way the later results relate to Jeffery's model. By deriving Eqs. (2.1) from a fundamental set of equations, we could provide the link to Jeffery [2007] and thereby unify and explain several results in the literature. First, Kumar *et al.* [2018] expected that mixing transcends from homogeneous to inhomogeneous with increasing values of Da_s at fixed χ , regardless of the value of Da_d . They were therefore surprised when they observed very small values of P_e^* for values of Da_s above the transition that they expected. We show that P_e^* at fixed χ must be understood as a function of both Da_d and Da_s in Kumar *et al.*

[2018]. Second, we show that droplet-size distributions and fractions of completely evaporated droplets of Kumar *et al.* [2014, 2012] are well explained in terms of Da_d and Da_s , both in the steady state and in the transient. Third, we show that the physics contained in Da_d and $\mathcal{R}/\mathcal{R}_c$ makes it possible to understand variations in P_e^* in the model of Andrejczuk *et al.* [2006], which differs somewhat from ours. Fourth, Korolev *et al.* [2016] and Pinsky *et al.* [2016*b*] concluded that Da_d is irrelevant for mixing-evaporation dynamics. We show that this is incorrect, and that the apparent contradiction is resolved by noting that the potential evaporation parameter R that appears in their dynamics is in fact a Damköhler-number ratio, $R \propto Da_d/Da_s$.

2.2.2 Statistical model

I mentioned in the introduction that we derive a statistical model for cloud-edge mixing and evaporation in Paper A. The numerical-simulation results in Paper A are computed using this statistical model. The model is derived from the simplified microscopic equations (2.1), which in turn are derived from the fundamental microscopic equations of Vaillancourt *et al.* [2001]. It belongs to the family of PDF models, introduced in Section 1.1.5. Briefly summarized, the model rests on a probabilistic description of air and droplets in terms of two one-point, one-time, PDF:s. It is best understood in terms of a Lagrangian stochastic model for independently evolving fluid elements with positions, velocities, and supersaturations [Eqs. (6) to (8) in Paper A]. Some fluid elements move together with a droplet, and those fluid elements are also described by the radius of their droplets [Eq. (9) in Paper A]. The statistical model employs closure approximations from the literature on PDF models, whose strengths and limitations are well understood [Jenny *et al.*, 2012].

We show in Paper A that the statistical model reproduces the time evolution of the fraction of completely evaporated droplets and the broadening of the droplet size distribution observed in DNS [Kumar *et al.*, 2014, 2012] (Figs. 2 and 3 of Paper A). We use the model to explore how mixing-evaporation dynamics depends qualitatively on its key parameters in both small and large Damköhler-number regimes. It is not possible to test the accuracy of the model at large values of Da_d and Da_s by comparing to DNS, because DNS at large Damköhler numbers is beyond the computational capability of today's computers. We argue in Paper A that the statistical model may not

work quantitatively in the limit of large Damköhler numbers, because it does not accurately account for effects of large saturated cloud structures. The statistical model should however work qualitatively in the large-Damköhler-number limit. This expectation rests on that the statistical model computes values of P_e^* that change monotonously with the parameters of the dynamics (Fig. 4 of Paper A), in a way that is consistent with the physics that the parameters describe.

Tails of droplet-size distributions come out lighter in the statistical model than in DNS (Fig. 3 of Paper A). We explain in Paper A that this is likely due to that the supersaturation dynamics of the model is oversimplified. The supersaturation $s(t)$ of a droplet in the statistical model decays towards a position-dependent mean field $\langle s(x, t) \rangle$ [Eq. (7) of Paper A]. In reality, one must expect a decay towards $\langle s(x, t) \rangle$ on average, but also fluctuations away from the mean field. The mean-field decay of the statistical model therefore underestimates the range of supersaturation fluctuations. Furthermore, it is known that mean-field decay does not allow the PDF of a passive scalar to relax into a Gaussian, as observed in DNS [Pope, 2000; Eswaran & Pope, 1988]. Gaussian relaxation must be expected for supersaturation at small values of Da_s , when supersaturation is only slowly affected by droplet phase change.

That the supersaturation dynamics of the statistical model is oversimplified can be understood from the evolution of the Lagrangian supersaturation PDF

$$\mathcal{F}_s(S; t) = \int \mathcal{F}_{sr^2}(S, R^2; t) dR^2, \quad (2.5)$$

a marginal PDF of the joint PDF $\mathcal{F}_{sr^2}(S, R^2; t)$ of droplets and supersaturation¹. The Lagrangian supersaturation PDF $\mathcal{F}_s(S; t)$ describes how supersaturation distributes over the droplets at time t . Fig. (2.3) shows a typical evolution of $\mathcal{F}_s(S; t)$ in the transient DNS of Kumar *et al.* [2014, 2018, 2013, 2012] (dashed lines). The PDF is a thin peak near saturation initially, because droplets are initialized within cloudy air. As mixing sets in, $\mathcal{F}_s(S; t)$ forms a heavy tail towards the (negative) supersaturation of dry air (blue and red). The tail is transient, and $\mathcal{F}_s(S; t)$ becomes a thin peak again when the system is mixed into homogeneity. Consistently with the passive-scalar observations mentioned above, $\mathcal{F}_s(S; t)$ adopts a Gaussian shape before the peak of

¹The joint PDF $\mathcal{F}_{sr^2}(S, R^2; t)$ of droplets and supersaturation was defined in Eq. (1.33).

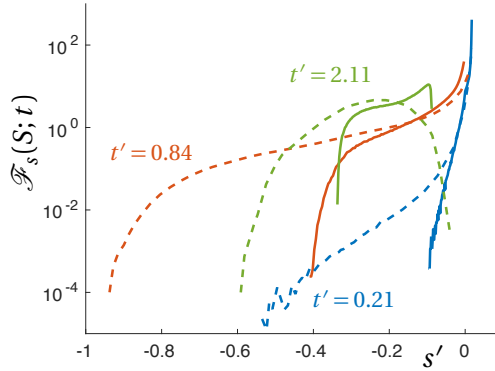


Figure 2.3: Lagrangian supersaturation PDF $\mathcal{F}_s(S; t)$ at different non-dimensional times $t' = t/\tau_L$ in statistical model of Paper A (solid lines) and DNS (dashed lines). The DNS results are from Kumar *et al.* [2014]. The axes are re-scaled to show $s' = s/|s_e|$, where s_e is the (negative) supersaturation of the initially dry air [Fig. (2.2)]. The tail of $\mathcal{F}_s(S; t)$ is less prominent in the statistical model than in DNS during the first large-eddy time (blue and red). Furthermore, $\mathcal{F}_s(S; t)$ does not relax into a Gaussian, as in DNS (green). The deviations are consequences of the oversimplified supersaturation dynamics of the statistical model (see text). The statistical-model simulation is for the key parameters $Da_d = 2.44$, $Da_s = 0.97$, and $\chi = 0.43$, its detailed setup is specified on the first row of Table S1 in the Supporting Information of Paper A. The DNS is simulation S1 of Kumar *et al.* [2014].

homogeneity establishes (green). The transient heavy tail of $\mathcal{F}_s(S; t)$ seems to form regardless of parametric setup in the DNS of Kumar *et al.* [2014, 2018, 2013, 2012]. Gaussian relaxation is however not always observed. The heavy tail of $\mathcal{F}_s(S; t)$ persists until the domain is saturated at larger Damköhler numbers than in Fig. (2.3) [Kumar *et al.*, 2012].

Also shown in Fig. (2.3) is the Lagrangian supersaturation PDF $\mathcal{F}_s(S; t)$ computed with the statistical model (solid lines). It can be seen that the heavy tail of $\mathcal{F}_s(S; t)$ is less prominent in the statistical model during the first large-eddy time (blue and red). This means that the most rapid evaporation rates are not reproduced by the statistical model, and explains why the statistical model computes a too light tail for the droplet-size distribution [Fig. (3) of Paper A]. The Gaussian relaxation of $\mathcal{F}_s(S; t)$ is also not reproduced by the statistical model (green). That the statistical model of Paper A fails to reproduce the Lagrangian supersaturation PDF in DNS is the motivation

behind the improved statistical model in Chapter 3. This model employs more refined closure approximations [Pope, 1991; Chen *et al.*, 1989; Fox, 1995], and quantitatively reproduces the Lagrangian supersaturation PDF at the Damköhler numbers of Fig. (2.3).

2.2.3 Interpretation of empirical data

In Paper A, we relate statistical-model results to empirical data represented in a mixing diagram, under the assumption that our model configuration [Fig. (2.2)] represents the evaporation and mixing that a cloud structure at the spatial scale L undergoes. To do so, we start by showing that the homogeneous mixing line can be generalized to droplet populations that have undergone complete droplet evaporation as well ($P_e^* > 0$). In fact, under the assumptions that pertain to the homogeneous mixing line, both P_e^* and the volume fraction χ of cloudy air are fully determined by \mathcal{R} for any steady state point $(n^*, \langle V \rangle^*)$ in a mixing diagram. For a simple form of the initial supersaturation profile one finds:

$$P_e^* = 1 - \frac{\frac{n^*}{n_0} \left(1 + \frac{3}{2}\mathcal{R}\right)}{\frac{n^*}{n_0} \frac{\langle V \rangle^*}{V_0} + \frac{3}{2}\mathcal{R}} \quad \text{and} \quad \chi = \frac{n^*/n_0}{1 - P_e^*}. \quad (2.6)$$

The homogeneous mixing line is parameterized by \mathcal{R} , and obtained from Eqs. (2.6) by inserting $P_e^* = 0$ and solving for $\langle V \rangle^*/V_0$.

Eqs. (2.6) allow us to map Da_d to the region above the homogeneous mixing line in a mixing diagram [Fig. 5(a) of Paper A], because we can compute P_e^* for combinations of Da_d , \mathcal{R} and χ . This gives meaning to the region above the homogeneous mixing line. The value of Da_d increases as one moves upwards from the homogeneous mixing line, into the region where complete droplet evaporation sets in. In light of this tendency, there are two ways in which an observed droplet population in the region above the homogeneous mixing line can be explained. Either Da_d must be large enough, which means that the mixing process that shaped the droplet population took place at a large-enough spatial scale L . Alternatively, the homogeneous mixing line must be raised, by decreasing the value of \mathcal{R} . Lower values of \mathcal{R} mean that the mixing process was moister: Fewer droplets evaporated completely, and the reduction in number density was caused by dilution to a higher degree. In Paper A, we use this theory to argue that many droplet populations observed

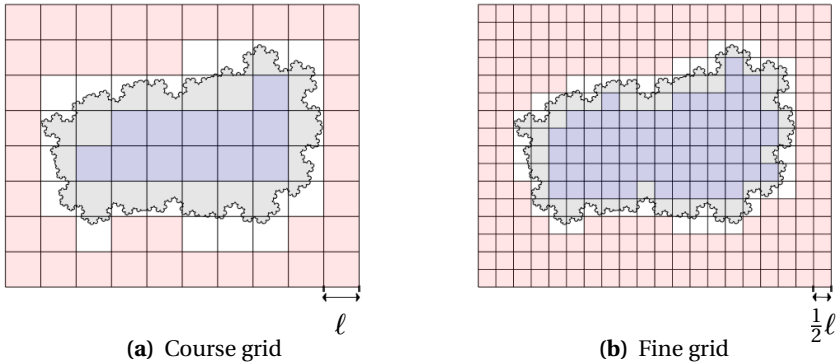


Figure 2.4: The same cloud (gray color) overlaid by two different box grids. The grid spacing in the left panel is ℓ , and the grid spacing in the right panel is $\ell/2$. Grid cells at moist steady states are colored blue, grid cells at dry steady states are colored red. White boxes are not equilibrated. In each panel, the ring of white boxes defines the cloud edge at a given spatial scale.

by Beals *et al.* [2015] resulted from mixing with premixed air. Premixed air has become partially saturated by earlier mixing events, and it is therefore not as dry as the air far away from the cloud. Furthermore, our analysis suggests that quite few droplets evaporated completely during the mixing of cloudy and premixed air, less than about 1%. The low droplet-number densities observed by Beals *et al.* [2015] are primarily a result of dilution, not complete droplet evaporation.

2.2.4 Multiscale picture of mixing and evaporation

In Paper A we let our analysis of empirical data from Beals *et al.* [2015] support a general discussion on mixing and evaporation in clouds. The simultaneous mixing and evaporation in turbulent clouds has been understood as a multiscale process, tied to the inertial range of turbulence, for a long time. An early model that makes use of inertial-range scaling arguments is due Baker *et al.* [1980]. By analyzing our model, we clarify the roles played by the two thermodynamic processes – droplet evaporation and saturation of the air – in the multiscale process. We do this by arguing for a simple picture of how the model parameters vary within the cloud, and near the cloud edge.

Figure (2.4) shows how a cloud can be decomposed into subvolumes defined by box grids. The grid spacing in Fig. (2.4b) is $\ell/2$, half the grid spacing ℓ in Fig. (2.4a). In each panel, the grid cells are colored based on their steady-state properties. Red boxes are at dry steady states, blue boxes are at moist steady states, and white boxes are not equilibrated. The cloud core is essentially saturated and consists of moist steady states, while the air outside of the cloud consists of dry steady states. In each panel, the ring of boxes that are not equilibrated can be taken as a definition of the cloud edge at the spatial scale of the box grid. Each box in Fig. (2.4a) defines a mixing process at the spatial scale ℓ , and each box in Fig. (2.4b) defines a mixing process at the spatial scale $\ell/2$. These mixing processes can be described using three parameters, for instance Da_d , \mathcal{R} , and χ . The larger mixing processes in Fig. (2.4a) have larger values of Da_d than the smaller ones in Fig. (2.4b), because their turnover times are longer. Large grid boxes at the cloud edge mix inhomogeneously, simply because they sample more droplets in the cloud core. This effect was understood already in 1979 [Baker & Latham, 1979]. We add to the understanding of local mixing-evaporation processes by noting how \mathcal{R} and χ varies within the cloud.

As one moves from the interior of the cloud and out into the dry air, the values of χ for local mixing-evaporation processes decrease from unity to zero, and the values of \mathcal{R} increase from zero to infinity. As a consequence, $\mathcal{R}/\mathcal{R}_c$ exceeds above unity as one passes the cloud edge. This reflects that complete droplet evaporation takes place at the cloud edge, because subsystems for which $\mathcal{R}/\mathcal{R}_c > 1$ tend towards dry steady states. The cloud is consumed by complete evaporation at a given spatial scale if cloud-edge processes at that scale tend towards dry steady states. The cloud expands by dilution if most processes tend towards moist steady states. A cloud can be consumed by complete evaporation at a given scale, even though this consumption is part of an expansion at larger spatial and temporal scales. In the same way, a small-scale expansion can be part of a large-scale consumption. Local equilibria are eventually abandoned, since they belong to transients at larger spatial scales. Central aspects of how evaporation distributes over a local droplet population in a cloud can therefore be described in terms of two parameters: Its spatial scale is contained in Da_d , and its distance to the cloud edge can be parameterized by $\mathcal{R}/\mathcal{R}_c$.

2.3 Discussion

A complicating factor to our multiscale theory of mixing and evaporation in clouds is that the air mass contained in a given box in Fig. (2.4a) or Fig. (2.4b) moves and deforms with time [Devenish *et al.*, 2012]. The air mass stretches and folds, so that it eventually adopts a highly irregular shape. Air and droplets constantly flow into and out of fixed grid boxes, and the flow between two grid boxes can therefore only be understood by analyzing both of them together. To what extent can the multiscale nature of mixing and evaporation in clouds then be understood by analyzing local mixing processes?

Despite that it is difficult to relate fixed volumes to mixing and evaporation in the atmosphere, one may argue that they allow for qualitatively correct predictions. It is reasonable to model the air mass contained within a cube of side length L at one particular instant using a cubic domain, as long as the air mass does not become too deformed. Mixing within such an air mass proceeds faster than the deformation, because this mixing is governed by motion at spatial scales $\ell < L$. Droplet evaporation and saturation causes the air mass to approach a steady state, which is moist or dry depending on the value of $\mathcal{R}/\mathcal{R}_c$. The steady state may not establish while the air mass has a shape that still reminds of the cube that contained it initially. Nevertheless, the value of $\mathcal{R}/\mathcal{R}_c$ determines the tendency of the evolution. In a frame that moves together with the cloud edge it is reasonable to assume that the air that enters the initial cubic volume has undergone a similar evolution as the original air mass. The model then represents the evolution within the cubic volume for some additional time. This argument can be repeated several times, so that it becomes an argument for that our model predicts a tendency for a cloud region to expand by dilution or shrink by complete evaporation. The argument therefore indicates that our model captures the thermodynamics and scale dependency of mixing and evaporation in atmospheric clouds, and that the multiscale theory outlined in Paper A is qualitatively correct.

3 Improved statistical model for the cloud edge

In this Chapter, I present a statistical model that – as opposed to the statistical model of Paper A – quantitatively reproduces the Lagrangian supersaturation PDF $\mathcal{F}_s(S; t)$ in DNS of transient cloud-edge mixing and evaporation¹. Quantitative agreement is obtained at low values of the Damköhler number Da_s , and after an initial transient at the largest values of Da_s explored in the DNS of Kumar *et al.* [2014, 2018, 2013, 2012]. I use the improved model to conclude that heavy tails of $\mathcal{F}_s(S; t)$ observed by Kumar *et al.* [2014, 2013, 2012] during the initial transient correspond to a U-shaped passive-scalar distribution in the DNS of Eswaran & Pope [1988]. Furthermore, I analyze how transient supersaturation dynamics differs from the corresponding dynamics of a passive scalar within finite simulation domains. Implications for the relaxation of supersaturation fluctuations during cloud-edge mixing and evaporation in the atmosphere are discussed.

3.1 Background

Kumar *et al.* [2014, 2013, 2012] emphasize that the Lagrangian supersaturation PDF $\mathcal{F}_s(S; t)$ forms a pronounced heavy tail that stretches towards the (negative) supersaturation of non-cloudy air during their transient DNS [Fig. (2.3)]. The heavy tail is significant, because it seems to form regardless of the parametric setup of the simulation, and makes it possible to compute similar heavy tails for the droplet-size distribution [Kumar *et al.*, 2012]. The tail relaxes after some time, and the PDF becomes approximately Gaussian if the Damköhler numbers Da_d and Da_s are not too large. But the heavy tail persists until the domain is saturated at $Da_s = 8.2$ and $Da_d = 0.75$ in [Kumar *et al.*, 2012] (see Paper A for definitions of Da_d and Da_s). Why the heavy tail forms is not understood, but Kumar *et al.* [2012] draw attention to exponential tails that the PDF of a passive scalar forms during turbulent mixing.

The PDF of a passive scalar is known to possess exponential tails under certain statistically stationary conditions, in the presence of a mean scalar gradient [Warhaft, 2000]. Without the mean gradient, the PDF is Gaussian

¹The Lagrangian supersaturation PDF $\mathcal{F}_s(S; t)$ was defined in Eq. (2.5).

or sub-Gaussian [Sreenivasan *et al.*, 1980]. Eswaran & Pope [1988] simulate decaying passive-scalar fluctuations, and show that an initially bimodal PDF relaxes to a Gaussian via a U-shaped distribution. The Gaussian outcome is consistent with the DNS of Kumar *et al.* [2014, 2012] at small values of Da_d and Da_s , but no consideration of passive-scalar mixing can explain why the heavy tail of $\mathcal{F}_s(S; t)$ persists at moderate Damköhler numbers.

The statistical model of Paper A allowed us to explain how droplet evaporation depends on Da_d and Da_s , but it is not suitable for analyzing the evolution of $\mathcal{F}_s(S; t)$. The reason is that its supersaturation dynamics is oversimplified. The supersaturation $s(t)$ of a droplet decays towards a position-dependent mean field $\langle s(x, t) \rangle$ [Eq. (7) of Paper A]. This underestimates the range of supersaturation fluctuations, and prevents the model from reproducing heavy tails and Gaussian relaxation of $\mathcal{F}_s(S; t)$, as explained in Section 2.2.2.

The reason we imposed decay towards $\langle s(x, t) \rangle$ in Paper A is that this respects the boundedness of supersaturation. Supersaturation is bounded, because the values that it can adopt within a given volume are constrained to remain between the minimal and maximal supersaturations of that volume [Pope, 1985]. This is strictly true for isobaric cloud dynamics if the non-linear dependency of supersaturation on temperature and water vapor is neglected, and approximately true otherwise [Yau & Rogers, 1989]. Droplet phase change quickly restores saturation within unmixed cloudy air, and the upper bound for supersaturation is therefore approximately zero when unmixed cloudy air is present. It is essential for a cloud-edge model to respect this upper bound. Cloud-edge models must namely describe how droplets within saturated air become exposed to strong negative supersaturations, while accounting for that fluctuations towards positive supersaturations are impossible.

To overcome the deficiencies of the statistical model of Paper A, it is necessary to describe a wider range of bounded supersaturation fluctuations along the Lagrangian trajectories of droplets. How to account for a wide range of scalar fluctuations in models has been extensively studied [Pope, 1985; Chen *et al.*, 1989; Curl, 1963; Valino & Dopazo, 1991; Fox, 1992; Meyer & Jenny, 2006]. There is however no model that, in itself, can be used to describe Lagrangian supersaturation fluctuations. Instead, one must look at how different models in combination allow for an accurate description.

3.2 My work

3.2.1 Combination of models

To develop the improved statistical model, I start by adopting a mapping closure of Chen *et al.* [1989]. Chen *et al.* [1989] outline different mapping closures for effects of turbulent mixing on the Eulerian PDF of a scalar². I adopt the simplest one, which is known to reproduce the shapes that Eulerian PDF:s of passive and reacting scalars adopt during transient turbulent mixing excellently [Pope, 1991; Valiño & Gao, 1992]. The mapping closure respects that scalars are bounded. Furthermore it makes the Eulerian PDF of a passive scalar relax to a Gaussian, as observed empirically [Eswaran & Pope, 1988]. Jeffery & Reisner [2006] used the mapping closure in a statistical model for mixing and evaporation within the cloud core. The model of Jeffery & Reisner [2006] is however not applicable to the cloud edge, because it describes only very moist systems in which droplet sizes remain constant during mixing. Importantly, Pope [1991] has suggested a Lagrangian stochastic model that employs the mapping closure to describe a wide range of bounded passive-scalar fluctuations along Lagrangian trajectories.

Unfortunately, the mapping closure does not predict the rate at which the Eulerian PDF of a scalar evolves. This rate can however be computed with the spectral relaxation model of Fox [1995]. The spectral relaxation model reproduces the decay of the variance of a passive scalar during turbulent mixing remarkably well, by describing how this variance distributes over a range of shells in wave-number space. The mapping closure of Chen *et al.* [1989], the Lagrangian stochastic model of Pope [1991], and the spectral relaxation model of Fox [1995] constitute a combination of models that makes it possible to describe a wide range of bounded passive-scalar fluctuations along Lagrangian trajectories. The statistical model employs this combination to describe bounded fluctuations of supersaturation. But supersaturation is not a passive scalar, because it is affected by droplet phase change. I therefore derive a new closure for effects of droplet phase change that can be used in combination with the passive-scalar models.

²Eulerian PDF:s are evaluated at fixed positions, as opposed to Lagrangian PDF:s. Lagrangian PDF:s are evaluated along droplet trajectories. This was explained in Section 1.1.5.

3.2.2 Probabilistic description

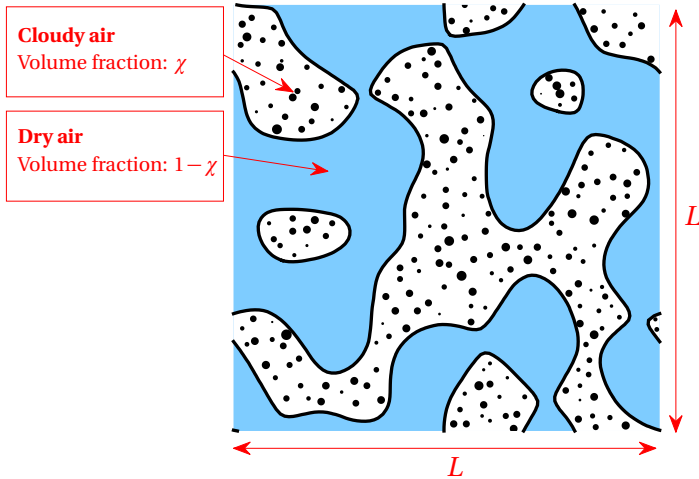


Figure 3.1: Initial condition for improved statistical model (schematic cross section). Cloudy filaments are initialized randomly within a cubic domain of size L with periodic boundary conditions. The cloudy filaments occupy a volume fraction χ of the domain, while the remainder of the domain is subsaturated air without droplets. The initial condition is statistically homogeneous, as required by the improved statistical model (see text).

The models of Chen *et al.* [1989], Pope [1991], and Fox [1995] that I incorporate into the statistical model describe statistically homogeneous systems only, systems in which all statistics of scalars and flow are independent of spatial position. The statistical model is therefore a model for statistically homogeneous cloud-edge mixing and evaporation. This makes the model less general than the statistical model of Paper A, which describes statistically inhomogeneous systems as well. It may be possible to extend the scope of the present statistical model to inhomogeneous systems in the future, using refined forms of its closure approximations [Fox, 1997; Klimenko & Pope, 2003]. For now, I focus on mixing and evaporation within statistically homogeneous systems.

The statistically homogeneous initial condition considered in the following is schematically illustrated in Fig. (3.1). Filaments of moist cloudy air with droplets are initialized randomly within a fixed cubic domain with periodic

boundary conditions. The side length of the cubic domain is L , and the cloudy air occupies a volume fraction χ of the domain. The remaining volume fraction $1 - \chi$ consists of subsaturated air without droplets. This initial condition is the statistically homogeneous analogue of the one-dimensional initial cloud slab in Fig. (2.2). The cloud slab is the initial condition of Paper A and the DNS of Kumar *et al.* [2014, 2018, 2013, 2012]. I may therefore compare results in these papers to results computed with the improved statistical model under the assumption that the detailed shape of the initial cloud slab in Fig. (2.2) is of secondary importance.

The initial condition in Fig. (3.1) entails statistically homogeneous mixing and evaporation if the flow is homogeneous turbulence. I assume stationary homogeneous isotropic turbulence with turbulent kinetic energy TKE, and mean dissipation rate of TKE per unit mass ε . I derive statistical-model equations from the simplified microscopic description in Eqs. (2.1). The dynamics is therefore parameterized by the Damköhler numbers Da_d and Da_s , whose effects on mixing and evaporation were explained in Section 2.2.1.

Just as in Paper A, I adopt a probabilistic description of droplets and air. I describe droplets using the joint PDF $\mathcal{F}_{sr^2}(S, R^2; t)$ of droplets and supersaturation, and I describe air using the Eulerian supersaturation PDF $f_s(S; t)$ ³. I write $f_s(S; t)$ without the position \mathbf{x} as an argument in this Chapter, as appropriate when describing statistically homogeneous systems. The statistical model can be formulated as a closed set of evolution equations for \mathcal{F}_{sr^2} and f_s . But the evolution equations of \mathcal{F}_{sr^2} and f_s are long and difficult to interpret, and I therefore present a more accessible formulation below.

3.2.3 Statistical-model derivation

Mapping closure

The mapping closure approximates effects of turbulent mixing on the shape of the Eulerian supersaturation PDF $f_s(S; t)$. It rests on one fundamental assumption: That unknown statistics of the supersaturation field $s(\mathbf{x}, t)$ equal corresponding statistics of a surrogate field $\widehat{s}(\mathbf{x}, t)$. The surrogate field is given by

$$\widehat{s}(\mathbf{x}, t) = X(\xi(\mathbf{x}, t), t), \quad (3.1)$$

³The PDFs $\mathcal{F}_{sr^2}(S, R^2; t)$ and $f_s(S; t)$ were defined in Eqs. (1.33) and (1.34).

where the so-called mapping $X(\eta, t)$ [Chen *et al.*, 1989] is a transformation of f_s , defined by the relation

$$F_s(X(\eta, t); t) = \mathbb{G}(\eta). \quad (3.2)$$

Here,

$$F_s(S; t) = \int_{-\infty}^S f_s(S'; t) dS' \quad (3.3)$$

is the Eulerian cumulative-distribution function (CDF) of supersaturation, and $\mathbb{G}(\eta)$ is the CDF of a standardized Gaussian. Furthermore, in Eq. (3.1), $\xi(\mathbf{x}, t)$ is a standardized Gaussian field, independent of time when expressed as a function of the stretched position $\mathbf{z} = J(t)\mathbf{x}$. Here, the stretching $J(t)$ is an unknown time-dependent function. It reflects that the mapping closure does not predict the supersaturation dissipation rate

$$\varepsilon_s(t) = 2\kappa \langle \nabla s \cdot \nabla s \rangle, \quad (3.4)$$

the decay rate of supersaturation variance in the absence of droplet phase change [Pope, 2000]. Under the mapping-closure assumption, $\varepsilon_s(t)$ determines the stretching $J(t)$ through [Pope, 1991]:

$$\varepsilon_s(t) = 2\kappa J(t)^2 \int_{-\infty}^{\infty} \frac{1}{\sqrt{2\pi}} \exp\left(-\frac{\eta^2}{2}\right) \left(\frac{\partial X}{\partial \eta}\right)^2 d\eta. \quad (3.5)$$

That the mapping closure does not predict $\varepsilon_s(t)$ reflects that it is applied to single-point statistics only, and single-point statistics can not account for length scales of supersaturation fluctuations. But it is well known that the rate at which a scalar dissipates depends sensitively upon the length scales of its fluctuations during initial stages of mixing [Eswaran & Pope, 1988]. For the initial conditions in Fig. (3.1), one must therefore expect that early values of $\varepsilon_s(t)$ are strongly affected by the sizes of the initial cloud filaments. To account for the length scales, the mapping closure must be supplemented by a model for $\varepsilon_s(t)$. The supplementary model adopted below is the spectral relaxation model of Fox [1995].

The point with the mapping closure is that its fundamental assumption implies an evolution equation for f_s , in which effects of turbulent mixing appear in closed form. The evolution equation is derived exactly from the

advection-diffusion equation (2.1c) for supersaturation, and it therefore inherits physics of supersaturation evolution. It is most conveniently expressed as an equivalent evolution equation for the mapping $X(\eta, t)$:

$$\frac{\partial X}{\partial t} = \kappa J(t)^2 \left(-\eta \frac{\partial X}{\partial \eta} + \frac{\partial^2 X}{\partial \eta^2} \right) - A_2 \langle C_d(t) | s = X \rangle. \quad (3.6)$$

The first term on the right-hand side of Eq. (3.6) describes how the mapping is affected by turbulent mixing. The second term describes effects of droplet phase change. Here, $\langle C_d(t) | s = X \rangle$ denotes the average condensation rate of air with supersaturation $s(\mathbf{x}, t) = X$. Why the mapping-closure assumption implies Eq. (3.6) is pedagogically explained by Pope [1991].

Now recall that the mapping $X(\eta, t)$ is a transformation of the Eulerian supersaturation PDF f_s , defined by Eqs. (3.2) and (3.3). The evolution equation (3.6) of the mapping therefore tells us that – under the mapping-closure assumption – one obtains a closed evolution equation for f_s by approximating the average $\langle C_d(t) | s = X \rangle$ in Eq. (3.6), and the supersaturation dissipation rate $\varepsilon_s(t)$ in Eq. (3.5). This simplifies the modeling of f_s tremendously, because it is no longer necessary to consider how the shape of the distribution is affected by turbulent mixing.

Spectral relaxation model

The statistical model employs the spectral relaxation model of Fox [1995] to approximate the dissipation rate $\varepsilon_s(t)$ of supersaturation [Eq. (3.4)]. This dissipation rate depends sensitively upon the length scales of supersaturation fluctuations during initial stages of mixing, as explained above. The length scales can be accounted for with the spectral relaxation model, which describes a turbulent cascade that transfers the variance of a passive-scalar variance upstreams in wave-number space. Supersaturation is not a passive scalar, because it is affected by droplet phase change. The spectral relaxation model is therefore employed under the assumption that effects of droplet phase change are of secondary importance for the cascade of supersaturation variance.

The spectral relaxation model was first formulated by Fox [1995], and Fox [1997] clarifies some details on how the model should be interpreted. I refer to these papers for a complete description, and summarize the model briefly in the following. In the spectral relaxation model, the cascade of passive-scalar

variance is described using M wave-number shells, separated by the wave numbers $0 = k_0 < k_1 < k_2 < \dots < k_M$. Here, k_1 is a wave number associated to the largest eddies of the velocity field, and k_M is associated to the smallest fluctuations of the scalar field. The variance $\langle s'(t)^2 \rangle_m$ within wave-number shell m is obtained by integrating the spectrum of supersaturation variance from wave number k_{m-1} to wave number k_m [Fox, 1997].

The spectral relaxation model assumes a feed-forward cascade of supersaturation variance that is local in wave-number space, and driven by fully developed turbulence. Under this assumption, Fox [1995] derives a set of ordinary differential equations for the variances $\langle s'(t)^2 \rangle_m$. These equations describe how variance within shell $m - 1$ is drained to shell m , while the variance within shell m is drained to shell $m + 1$. The rates of transfer are determined by time constants t_m , one for each shell m . The small-scale variance $\langle s'(t)^2 \rangle_M$ is used to account for the turbulent cascade in a heuristic model for the supersaturation dissipation rate:

$$\begin{aligned} \frac{d\varepsilon_s}{dt} = & 2C_\omega \tau_\eta^{-1} \varepsilon_s(t) - \frac{2C_\chi}{2 + \text{Sc}^{-1}} \frac{1}{\sigma_s^2(t)} \left(\varepsilon_s(t) + C_D \tau_\eta^{-1} \sum_{m=1}^M \langle s'(t)^2 \rangle_m \right) \varepsilon_s(t) \\ & + C_D C_\phi \tau_\eta^{-1} \frac{\langle s'(t)^2 \rangle_M}{t_M} \end{aligned} \quad (3.7)$$

The first and second terms describe effects of turbulent stretching and molecular diffusion of supersaturation gradients. Here, C_ω and C_χ are modeling constants, τ_η is the Kolmogorov time [Eq. (1.19)], $\sigma_s^2(t)$ is the variance of supersaturation, $\text{Sc} = \kappa/\nu$ is the Schmidt number of supersaturation, and $C_D = 2C_\omega(2 + \text{Sc}^{-1})/(2C_\chi - 2 - \text{Sc}^{-1})$. The third term describes how $\varepsilon_s(t)$ may increase due to small-scale fluctuations of supersaturation generated by the turbulent cascade. Here, C_ϕ is an empirical constant. It gives the exponential decay $\sigma^2(t) \sim e^{-C_\phi t}$ for the variance $\sigma^2(t)$ of a passive scalar during late stages of turbulent mixing [Eswaran & Pope, 1988]. Furthermore, t_M is the time constant of the uppermost wave-number shell.

I compare statistical-model results to DNS in Section 3.2.5. Meaningful comparison requires that the empirical constant C_ϕ in Eq. (3.7) is not too crudely estimated. I therefore estimate $C_\phi = 2.5$ from Kumar *et al.* [2012] when comparing to their DNS results. Details on this estimate are given in Appendix A. Implications for the interpretation of statistical-model results are discussed in Section 3.3.

Closure for droplet phase change

A closure is required for the average condensation rate conditional on the supersaturation S , $\langle C_d(t) | s = S \rangle$. This average appears in the evolution equation (3.6) for the mapping $X(\eta, t)$, but with the argument X instead of S . It describes how the mapping is affected by droplet phase change. Equivalently, it describes how the Eulerian supersaturation PDF $f_s(S; t)$ is affected by droplet phase change, because f_s and $X(\eta, t)$ are transformations of each other. The average $\langle C_d(t) | s = S \rangle$ corresponds to the condensation rate averaged along contours of constant supersaturation $s(\mathbf{x}, t) = S$. Such contours are determined by local mixing-evaporation processes, and must therefore reflect the shapes of cloudy and non-cloudy structures. Examples of such contours are schematically illustrated in Fig. (3.2).



Figure 3.2: Contours of constant supersaturation in a region with cloudy and non-cloudy air (schematic). The contours $s(\mathbf{x}, t) = S_1$, $s(\mathbf{x}, t) = S_2$, and $s(\mathbf{x}, t) = S_3$ are determined by local mixing-evaporation processes, and reflect the shapes of cloudy and non-cloudy structures. The improved statistical model requires a closure for the average $\langle C_d(t) | s = S \rangle$, the average condensation rate conditional on the supersaturation $s(\mathbf{x}, t) = S$ (see text).

My closure for the effects of droplet phase change in Eq. (3.6) amounts to

an accurate approximation of the average $\langle C_d(t) | s = S \rangle$,

$$\langle C_d(t) | s = S \rangle = 4\pi A_3 \varrho_p S \frac{N_0/V}{f_s(S; t)} \int R \mathcal{F}_{sr^2}(S, R^2; t) dR^2. \quad (3.8)$$

Here, $V = L^3$ is the volume of the simulation domain, and N_0 denotes the number of droplets within the domain. In the following, I summarize the most important steps in the derivation of $\langle C_d(t) | s = S \rangle$. Details are provided in Appendix B.

The derivation of Eq. (3.8) starts by imposing that the width of the spatial kernel $G(|\mathbf{x} - \mathbf{x}_\alpha(t)|)$ in Eq. (1.12) is much smaller than the smallest length scale of the supersaturation field. This makes it possible to compute the average condensation rate $\overline{C}_d(t)|_S^{S+\Delta S}$ in the space between the supersaturation contours $s(\mathbf{x}, t) = S$ and $s(\mathbf{x}, t) = S + \Delta S$, in the limit of small ΔS . The average $\overline{C}_d(t)|_S^{S+\Delta S}$ depends on the number $N(t)_S^{S+\Delta S}$ of droplets that are present within the space, and the volume $V(t)_S^{S+\Delta S}$ of the space. In the limit $\Delta S \rightarrow 0$, one obtains the average condensation rate $\overline{C}_d(t)|_S$ at the contour $s(\mathbf{x}, t) = S$:

$$\overline{C}_d(t)|_S = 4\pi A_3 \varrho_w \overline{r}(t)_S S \lim_{\Delta S \rightarrow 0} \frac{N(t)_S^{S+\Delta S}}{V(t)_S^{S+\Delta S}}. \quad (3.9)$$

Here, $\overline{r}(t)_S$ is the average droplet radius at the contour $s(\mathbf{x}, t) = S$. To be able to take the limit $\Delta S \rightarrow 0$, one must account for that droplets are not points in terms of their effects on supersaturation. Instead, it is the spatial kernel $G(|\mathbf{x} - \mathbf{x}_\alpha(t)|)$ that describes the effects of a droplet at a given position. The variables $N(t)_S^{S+\Delta S}$ and $\overline{r}(t)_S$ are defined in Appendix B, and account for the spatial kernel $G(|\mathbf{x} - \mathbf{x}_\alpha(t)|)$.

The effects of the width of the spatial kernel $G(|\mathbf{x} - \mathbf{x}_\alpha(t)|)$ has not been systematically analyzed in the context of a supersaturation field $s(\mathbf{x}, t)$ that varies in space. Srivastava [1989] analyzed effects of droplet-droplet interactions when $s(\mathbf{x}, t)$ is spatially uniform, and one may infer from his analysis that a well-chosen width is smaller than or comparable to the typical distances between droplets. I now argue that it is not an approximation to impose that the width of $G(|\mathbf{x} - \mathbf{x}_\alpha(t)|)$ is much smaller than the smallest length scale of the supersaturation field. The presence of $G(|\mathbf{x} - \mathbf{x}_\alpha(t)|)$ in Eq. (1.12) reflects that phase-changing droplets exchange water and heat with the surrounding air. Meanwhile, the droplet-growth equation (2.1e) is

derived by imposing that the supersaturation $s(\mathbf{x}_\alpha(t), t)$ of droplet α is the supersaturation at distances from the droplet that are much larger than the droplet radius $r_\alpha(t)$ [Yau & Rogers, 1989]. Furthermore, it is assumed that the supersaturation of the air that the droplet exchanges water and heat with equals $s(\mathbf{x}_\alpha(t), t)$. This kind of exchange is only obtained if the width of the spatial kernel $G(|\mathbf{x} - \mathbf{x}_\alpha(t)|)$ is much smaller than the smallest length scale of the supersaturation field. This means that the small kernel width that I impose is consistent with the physics described by Eqs. (2.1).

To understand the final approximation in the derivation of Eq. (3.8), one must recall that $\overline{C}_d(t)|_S$, $\overline{r}(t)_S$, $N(t)_S^{S+\Delta S}$, and $V(t)_S^{S+\Delta S}$ are computed from the microscopic Eqs. (2.1). Independent realizations of the microscopic dynamics are subject to statistical variability, and we have no reason to believe that $\overline{C}_d(t)|_S$, $\overline{r}(t)_S$, $N(t)_S^{S+\Delta S}$, and $V(t)_S^{S+\Delta S}$ adopt precisely the same values in different realizations [Eswaran & Pope, 1988]. This means that these variables are, in fact, stochastic. The final approximation of the closure is to neglect their statistical variability, and define

$$\langle C_d(t)|s=S \rangle = 4\pi A_3 \varrho_p \langle r(t)|s=S \rangle_{[d]} S \lim_{\Delta S \rightarrow 0} \frac{\langle N(t)_S^{S+\Delta S} \rangle}{\langle V(t)_S^{S+\Delta S} \rangle}, \quad (3.10)$$

where

$$\langle r(t)|s=S \rangle_{[d]} = \int R \frac{\mathcal{F}_{sr^2}(S, R^2; t)}{\mathcal{F}_s(S; t)} dR^2 \quad (3.11)$$

is the average radius of droplets with supersaturations $s(t) = S$. Eq. (3.8) is obtained from Eqs. (3.10) and (3.11), because

$$\lim_{\Delta S \rightarrow 0} \frac{\langle N(t)_S^{S+\Delta S} \rangle}{\langle V(t)_S^{S+\Delta S} \rangle} = \frac{N_0}{V} \frac{\mathcal{F}_s(S; t)}{f_s(S; t)}. \quad (3.12)$$

A proof of this relation is provided in Appendix B.

There may be circumstances under which statistical variability is important, but I expect that statistical variability is of secondary importance in DNS of cloud-edge mixing and evaporation. Values of $\overline{C}_d(t)|_S$, $\overline{r}(t)_S$, $N(t)_S^{S+\Delta S}$, and $V(t)_S^{S+\Delta S}$ adopted in such DNS first and foremost reflect the simulated physics, which is the same for all simulations with identical parameters. Assumptions of negligible statistical variability are implicit in the DNS studies

of Kumar *et al.* [2014, 2018, 2013, 2012], because independent simulation results for identical combinations of parameters are not shown.

The statistical model employs the function $\langle C_d(t) | s = S \rangle$ in Eq. (3.8) to approximate effects of droplet phase change on f_s , but not on \mathcal{F}_{sr^2} . It is in principle possible to use $\langle C_d(t) | s = S \rangle$ to approximate the effects of droplet phase change on \mathcal{F}_{sr^2} as well, but it then becomes difficult to obtain closure for the effects of turbulent mixing on \mathcal{F}_{sr^2} , without violating the boundedness of supersaturation. In the following, I adopt a Lagrangian stochastic model for the supersaturations of droplets. This model provides closure for the effects of both droplet phase change and turbulent mixing on \mathcal{F}_{sr^2} , and it respects the boundedness of supersaturation.

Lagrangian stochastic model

Having adopted the mapping closure of Chen *et al.* [1989] to describe effects of turbulent mixing on the Eulerian supersaturation PDF f_s , it is straightforward to describe a wide range of bounded supersaturation fluctuations along the Lagrangian trajectories of droplets. The reason is that the mapping $X(\eta, t)$, which is a transformation of f_s , maps any stochastic process $\xi(t)$ to a stochastic process of supersaturation $s(t) = X(\xi(t), t)$ that inherits the bounds of f_s . As mentioned above, I adopt a Lagrangian stochastic model of Pope [1991]:

$$s(t) = X(\xi(t), t) \quad (3.13a)$$

$$d\xi(t) = -\xi(t)\kappa J(t)^2 dt + [2\kappa J(t)^2]^{1/2} d\zeta(t). \quad (3.13b)$$

Eq. (3.13a) prescribes that the supersaturation $s(t)$ of a droplet couples to the supersaturation $s(\mathbf{x}, t)$ of air through the mapping $X(\eta, t)$. The Lagrangian fluctuations are provided through the argument $\xi(t)$ of the mapping, which is given by an independent stochastic process for each droplet. This stochastic process is Eq. (3.13b). In Eq. (3.13b), $d\zeta(t)$ are stochastic Brownian increments with variance equal to the time step dt [Pope, 2000]. The stochastic process in Eq. (3.13b) is an Ornstein-Uhlenbeck process with variance unity and a time-dependent auto-correlation frequency $\kappa J(t)^2$.

Turbulent mixing ensures that the initial supersaturations of an ensemble of droplets are eventually forgotten, so that droplets sample the air uniformly after some time. I now explain that Eqs. (3.13a) and (3.13b) ensure that the

statistical model reproduces this important aspect of droplet dynamics. The Ornstein-Uhlenbeck process in Eq. (3.13b) ensures that the distribution of $\xi(t)$ relaxes to a standardized Gaussian with time [Pope, 2000]. Meanwhile, the mapping $X(\eta, t)$ in Eq. (3.13a) transforms a standardized Gaussian to the Eulerian supersaturation PDF $f_s(S; t)$ through Eq. (3.2) [Pope, 1991]. A combined effect of Eqs. (3.13a) and (3.13b) is therefore that the Lagrangian supersaturation PDF $\mathcal{F}_s(S; t)$ relaxes to the Eulerian supersaturation PDF $f_s(S; t)$ with time.

When Pope [1991] suggested Eqs. (3.13a) and (3.13b) as a model for Lagrangian fluctuations, he did not specify the time-dependent auto-correlation frequency in Eq. (3.13b). I prescribe the auto-correlation frequency $\kappa J(t)^2$. An auto-correlation frequency proportional to $\kappa J(t)^2$ is required for consistency with the mapping-closure assumption, at least in the absence of droplet phase change. Under the mapping-closure assumption, conditional averages of the Laplacian $\nabla^2 s$ of supersaturation are proportional to $J(t)^2$ [Pope, 1991]. Meanwhile, continuity of probability dictates that the time derivative of $\mathcal{F}_s(S; t)$ is proportional to a conditional average of $\kappa \nabla^2 s$ (in the absence of droplet phase change) [Pope, 1985]. Consistency with the mapping-closure assumption therefore requires that the time derivative of $\mathcal{F}_s(S; t)$ is proportional to $\kappa J(t)^2$. This requirement is met in the statistical model if and only if the auto-correlation frequency in Eq. (3.13b) is proportional to $\kappa J(t)^2$. The constant of proportionality is set to unity in Eq. (3.13b).

Pope [1991] formulated Eqs. (3.13a) and (3.13b) as a model for Lagrangian fluctuations of a passive scalar. How well can we expect this model to describe the supersaturations of droplets? The supersaturation of a droplet that resides in saturated cloudy air initially, but is exposed to subsaturated air at a later time, undergoes a net decrease. The supersaturation may not decrease monotonously, because the droplet may move into and out of cloudy regions. At a given instant, the droplet tends to move together with a neighborhood of droplets that is carried together, by the same flow. When the droplet and its neighbors evaporate, they saturate the air they reside in collectively. This means that decreases in supersaturation along the trajectory of a droplet tend to be delayed by the presence of other droplets. In other words, droplet interaction gives rise to Lagrangian correlations of supersaturation and condensation rate. Eqs. (3.13a) and (3.13b) do not account for the Lagrangian correlations, because the increment of the stochastic variable $\xi(t)$ for a droplet in Eq. (3.13b) does not reflect the presence of neighboring

droplets. Droplet phase change affects supersaturation rapidly when Da_s is large, so Lagrangian correlations of supersaturation and condensation rate are most important at large values of Da_s . I therefore do not expect that the statistical model reproduces the supersaturations of droplets quantitatively when Da_s is large. In the Outlook of this thesis, I argue for how this problem may be resolved in an improved future version of the model.

3.2.4 Statistical-model equations

The statistical model is obtained by imposing the closures listed in Section 3.2.3. It prescribes the following stochastic dynamics for droplets with radii $r(t)$ and supersaturations $s(t)$:

$$\frac{dr(t)^2}{dt} = 2A_3 s(t), \quad (3.14a)$$

$$s(t) = X(\xi(t), t), \quad \text{and} \quad (3.14b)$$

$$d\xi(t) = -\xi(t)\kappa J(t)^2 dt + [2\kappa J(t)^2]^{\frac{1}{2}} d\zeta(t). \quad (3.14c)$$

Eq. (3.14a) is the droplet growth equation, Eq. (2.1e). Eqs. (3.14b) and (3.14c) are the Lagrangian stochastic model of Pope [1991]. The mapping $X(\eta, t)$ evolves according to

$$\frac{\partial X}{\partial t} = \kappa J(t)^2 \left(-\eta \frac{\partial X}{\partial \eta} + \frac{\partial^2 X}{\partial \eta^2} \right) - A_2 \langle C_d(t) | s = X \rangle, \quad (3.15)$$

where $\langle C_d(t) | s = X \rangle$ is the approximation in Eq. (3.8). The factor $\kappa J(t)^2$ in Eqs. (3.14) and (3.15) is given by Eq. (3.5), where the supersaturation dissipation rate $\varepsilon_s(t)$ is computed using the spectral relaxation model of Fox [1995]. Details on the implementation of the spectral relaxation model behind the statistical-model simulations reported below are given in Appendix A.

The statistical-model equations (3.14) and (3.15) correspond a closed set of evolution equations for the joint PDF $\mathcal{F}_{sr^2}(S, R^2; t)$ of droplets and supersaturation and the Eulerian supersaturation PDF $f_s(S; t)$. The evolution equation of \mathcal{F}_{sr^2} can be obtained from Eqs. (3.14) in two steps. First, one concatenates Eqs. (3.14b) and (3.14c) into a single stochastic differential equation for $s(t)$ using the Ito transformation [Pope, 1991]. Second, one formulates the Fokker-Planck equation that corresponds to the stochastic dynamics of $s(t)$ and $r(t)^2$. Eq. (3.15) for the mapping $X(\eta, t)$ corresponds

to an evolution equation of f_s , because the mapping is a transformation of f_s . The evolution equations of \mathcal{F}_{sr^2} and f_s are long and difficult to interpret, and therefore not given.

Non-dimensional dynamics

In the next section, I compare non-dimensional statistical-model results to DNS of Kumar *et al.* [2012]. For the purpose of that section, I non-dimensionalize as follows: $t' = t/\tau_L$, $s' = s/|s_e|$, $X' = X/|s_e|$, $J^{2'} = \kappa J^2 \tau_L$, $r' = r/r_0$, $C'_d = C_d/(4\pi A_3 \rho_p n_0 r_0 |s_e|)$, $V' = V/(U \tau_L)^3$, and $G' = G(U \tau_L)^3$. Here, $\tau_L = \text{TKE}/\varepsilon$ is the large-eddy turnover time, $U = \sqrt{2\text{TKE}/3}$ is the root-mean square velocity, $n_0 = N_0/(\chi V)$ is the droplet-number density of the initial cloud filaments, $|s_e|$ is the (positive) subsaturation of the initially non-cloudy air, and $r_0 = [N_0^{-1} \sum_{\alpha=1}^{N_0} r_\alpha(0)^3]^{1/3}$ is the initial volume-averaged droplet radius. Dropping the primes, Eqs. (3.14) and (3.15) take the non-dimensional form:

$$\frac{dr(t)^2}{dt} = \text{Da}_d s(t), \quad (3.16a)$$

$$s(t) = X(\xi(t), t), \quad (3.16b)$$

$$d\xi(t) = -\xi(t)J(t)^2 dt + [2J(t)^2]^{1/2} d\zeta(t), \quad \text{and} \quad (3.16c)$$

$$\frac{\partial X}{\partial t} = J(t)^2 \left(-\eta \frac{\partial X}{\partial \eta} + \frac{\partial^2 X}{\partial \eta^2} \right) - \text{Da}_s \langle C_d(t) | s = X \rangle, \quad (3.16d)$$

with

$$\langle C_d(t) | s = X \rangle = \frac{\chi}{f_s(X; t)} \int R \mathcal{F}_{sr^2}(X, R^2; t) dS dR^2. \quad (3.16e)$$

Here, Da_d and Da_s are the Damköhler numbers discussed in Section 2.2.1, see Paper A for definitions. Eq. (3.16) tells us that the statistical-model dynamics is determined by Da_d and Da_s , together with parameters of the spectral relaxation model determining the evolution of the stretching $J(t)$. See Appendix A for the spectral-relaxation-model parameters of the statistical-model simulations reported below.

3.2.5 Simulation results

Fig. (3.3a) shows the Lagrangian supersaturation PDF $\mathcal{F}_s(S; t)$ in the statistical model (solid lines), and in the DNS of Kumar *et al.* [2012] (dashed

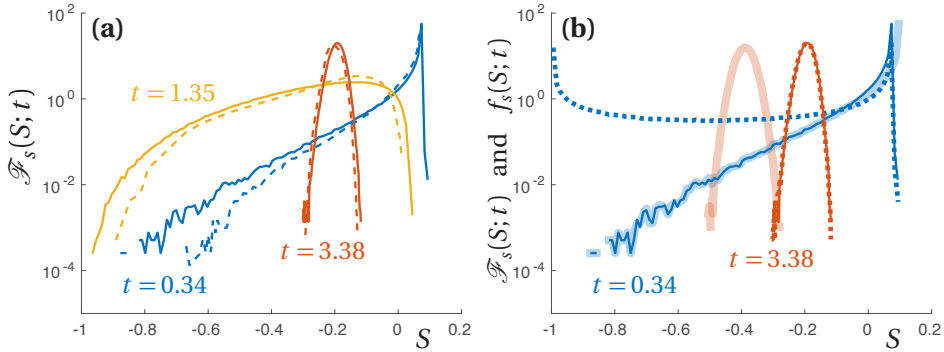


Figure 3.3: (a) Lagrangian supersaturation PDF $\mathcal{F}_s(S; t)$ at different non-dimensional times t in the improved statistical model (solid lines), and in DNS of Kumar *et al.* [2012] (dashed lines) at $Da_s = 0.82$ and $Da_d = 0.075$. See Appendix A for details. (b) Statistical-model results for the Lagrangian supersaturation PDF $\mathcal{F}_s(S; t)$ at zero (thick solid lines) and non-zero (thin solid lines) values of Da_s . The results for $Da_s > 0$ are for the simulation in panel (a), and the results at $Da_s = 0$ is for the same value of Da_d . Also shown is the Eulerian supersaturation PDF $f_s(S; t)$ (dotted lines) for the simulations with $Da_s > 0$.

lines) at $Da_s = 0.82$ and $Da_d = 0.075$. A complete specification of simulation parameters is given in Appendix A. It can be seen that the statistical model reproduces $\mathcal{F}_s(S; t)$ in DNS quantitatively at these Damköhler numbers. This indicates that the closures for turbulent mixing of the statistical model are accurate, and I therefore proceed by comparing the supersaturation results in Fig. (3.3a) to analogous results of for a passive scalar using the statistical model.

Fig. (3.3b) shows statistical-model results from Fig. (3.3a) (thin solid lines) together with corresponding statistical-model results for a passive scalar (thick solid lines), obtained by setting Da_s to zero in Eq. (3.16d). It can be seen that the supersaturation dynamics shaping $\mathcal{F}_s(S; t)$ in Fig. 3.3 is quite simple. Supersaturation behaves like a passive scalar during the first large-eddy time. After that, droplet phase change causes the mean of $\mathcal{F}_s(S; t)$ to drift, while supersaturation fluctuations decay like the fluctuations of a passive scalar. The relaxation is in the form of a Gaussian, just as in the DNS of transient passive-scalar mixing of Eswaran & Pope [1988]. This type

of supersaturation dynamics must be expected at low Da_s , where droplets saturate the air only after the system has been well mixed [Dimotakis, 2005].

Also shown in Fig. (3.3b) is the Eulerian supersaturation PDF $f_s(S; t)$ (dotted lines). During the initial transient, $f_s(S; t)$ is U-shaped, because both cloudy and non-cloudy air remain. The distribution is very similar to the U-shaped distribution of Eswaran & Pope [1988], and one must expect a direct correspondence in the absence of droplet phase change. Droplets are initialized into air that is saturated, or nearly saturated, and few of them encounter dry air during the initial transient. As a consequence, the Lagrangian PDF $\mathcal{F}_s(S; t)$ possesses only the saturated peak of $f_s(S; t)$, and has a heavy tail that corresponds to the right half of the U-shaped distribution. The relaxation of the Lagrangian PDF $\mathcal{F}_s(S; t)$ to the Eulerian PDF $f_s(S; t)$ discussed above can be seen in Fig. (3.3b), where the two PDF:s have become indistinguishable after 3.38 large-eddy times.

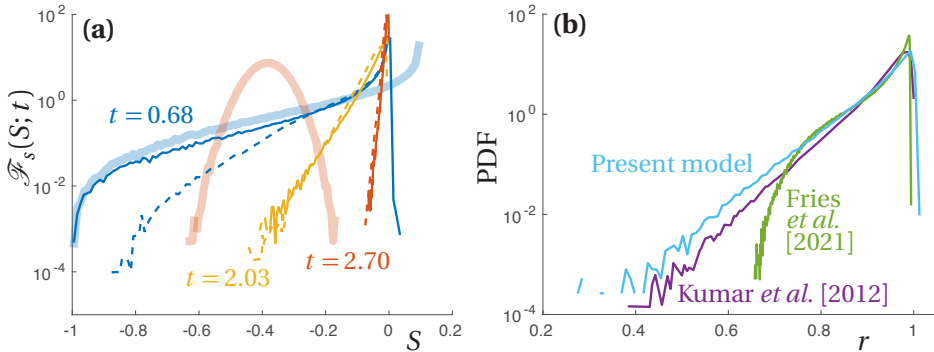


Figure 3.4: Lagrangian supersaturation PDF $\mathcal{F}_s(S; t)$ and droplet-size distribution at $Da_s = 8.2$ and $Da_d = 0.75$. See Appendix A for details. **(a)** The PDF $\mathcal{F}_s(S; t)$ at different non-dimensional times t in the improved statistical model (solid lines), and in DNS of Kumar *et al.* [2012] (dashed lines). **(b)** Steady-state droplet-size distribution in DNS of Kumar *et al.* [2012] (purple), statistical model of Paper A (green), and improved statistical model (light blue).

Fig. (3.4a) shows $\mathcal{F}_s(S; t)$ in the statistical model and in the DNS of Kumar *et al.* [2012] as in Fig. (3.3a), but at larger Damköhler numbers. Here, both Damköhler numbers are larger than in Fig. (3.3a) by a factor ten. The Damköhler number $Da_s = 8.2$ is the largest value of Da_s explored in the DNS

of Kumar *et al.* [2014, 2018, 2013, 2012] (see Fig. 4 of Paper A). The statistical model computes a too heavy tail for $\mathcal{F}_s(S; t)$ during the initial transient in Fig. (3.4a), but reproduces the tail excellently from about two large-eddy times. The initial deviation is expected. As explained above, the statistical model neglects Lagrangian correlations between supersaturation and condensation rate. At large enough values of Da_s , such correlations are important during the initial transient, when little mixing has taken place and droplets still reside within pronounced cloud structures. Decreases in supersaturation are delayed due to the pronounced structures, because droplets saturate the air within these structures collectively. The collective saturation neglected by the statistical model suppresses the tail of $\mathcal{F}_s(S; t)$ in the DNS of Kumar *et al.* [2012].

The initial deviations between statistical-model results and DNS in Fig. (3.4a) makes the excellent agreement at later times interesting. The heavy tail persists until the domain is saturated, but the persisting tail can not be affected by the Lagrangian correlations between supersaturation and condensation rate that the statistical model neglects. This means that there are two types of heavy tails in the DNS of Kumar *et al.* [2012]. One early type that depends on the Lagrangian correlations, and one later type that does not. A plausible explanation of the excellent agreement at late times in Fig. (3.4a) is that the persisting heavy tail forms when the droplet content has become spatially uniform. However, there are no reported DNS results that make it possible to conclude whether this is the case or not.

Also shown in Fig. (3.4a) are statistical-model predictions for a passive scalar (thick opaque lines), obtained by setting Da_s to zero in Eq. (3.16d). It can be seen that supersaturation behaves similarly to a passive scalar in the statistical model during the first large-eddy time. This is most likely a consequence of the neglected Lagrangian correlations. The Gaussian distribution of the passive scalar at later times is however clearly different from the statistical-model prediction of the persisting heavy tail. The differences between DNS results of Kumar *et al.* [2012] and passive-scalar predictions in Fig. (3.4a) tell us that the dynamics of supersaturation is quite different from that of a passive scalar, already at moderate Damköhler numbers.

Finally, I show that the statistical model is an improvement compared to the statistical model of Paper A, when it comes to predicting droplet-size distributions. Fig. (3.4b) shows steady-state droplet-size distributions at the Damköhler numbers of Fig. (3.4a) from DNS of Kumar *et al.* [2012] (pur-

ple), the improved statistical model (light blue), and the statistical model of Paper A (green). As opposed to the statistical model of Paper A, the improved statistical model reproduces the shape of the droplet-size distribution. The tail of the distribution comes out slightly heavier than in DNS however, which likely reflects the too heavy tail of $\mathcal{F}_s(S; t)$ during the initial transient in Fig. (3.4a). The improved statistical model reproduces droplet-size distributions at the low Damköhler numbers of Fig. (3.3) excellently (not shown).

3.3 Discussion

The above results yield insights into similarities and differences between supersaturation dynamics and the dynamics of a passive scalar. The formation of a heavy tail for the Lagrangian supersaturation PDF $\mathcal{F}_s(S; t)$ in the DNS of Kumar *et al.* [2014, 2013, 2012] is a passive-scalar behavior. However, the shape of the tail, and its persistence at large times, are strongly dependent on droplet phase change. Whether, why and how scalar PDF:s form heavy tails reflects how scalar inhomogeneities are introduced [Warhaft, 2000]. Stationary configurations in which exponential tails are sustained by forcing, or form in the presence of a mean scalar gradient, are not directly comparable to the transient DNS of Kumar *et al.* [2014, 2013, 2012]. The passive-scalar inhomogeneities initialized in the transient DNS of Eswaran & Pope [1988], on the other hand, are similar to the initial supersaturation inhomogeneity of Kumar *et al.* [2014, 2013, 2012]. This notion made it possible to conclude that the heavy tails of $\mathcal{F}_s(S; t)$ observed by Kumar *et al.* [2014, 2013, 2012] during the initial transient correspond to the U-shaped Eulerian passive-scalar distribution observed by Eswaran & Pope [1988].

That supersaturation behaves less similar to a passive scalar with increasing values of Da_s does not come as a surprise [see for instance Eq. (2) of Paper A]. One passive-scalar behavior of supersaturation at low values of Da_s is the Gaussian relaxation of $\mathcal{F}_s(S; t)$ [Fig. (3.3)]. By contrast, the persisting heavy tail at moderate values of Da_s is clearly a consequence of droplet phase change [Fig. (3.4a)]. The difference between these two relaxations can be understood through the boundedness of supersaturation. Subsaturated air can not obtain a positive supersaturation through droplet phase change, and saturation therefore constitutes an upper bound for $\mathcal{F}_s(S; t)$ during

evaporation. Phase change prevents Gaussian relaxation in Fig. (3.4a), by rapidly driving the mean of the distribution towards this upper bound. The persisting exponential tail therefore corresponds to the subsaturated tail of a Gaussian. That the shape of this tail does not match a Gaussian is a consequence of mixing with saturated air.

How supersaturation relaxes is highly relevant for statistical models of cloud-core dynamics. Cloud-core models that sustain Gaussian fluctuation of scalars by means of a forcing have been very successful in predicting cloud-core dynamics in simulations [Sardina *et al.*, 2015; Paoli & Shariff, 2009; Siewert *et al.*, 2017] and under laboratory conditions [Chandrakar *et al.*, 2016]. It is however not clear how supersaturation fluctuations in the atmosphere are affected by droplet phase change, because the supersaturations of individual droplets can not be observed with the measurement techniques of today. In-situ measurements that resolve supersaturation on spatial scales of about one meter indicate Gaussian distributions [Siebert & Shaw, 2017], while better resolved laboratory measurements reveal skewed distributions [Anderson *et al.*, 2021]. An indication of non-trivial effects of droplet phase change may be that a Gaussian model fails to compute the width of the droplet-size distribution in the cloud chamber experiment of Chandrakar *et al.* [2016] when Da_s is large. The authors speculate whether the deviations are indicative of a prolonged cloud-chamber residence time of droplets. Another possible explanation is that the Lagrangian supersaturation PDF was non-Gaussian. That supersaturation is a non-linear function of temperature and water-vapor content can be accounted for in a Gaussian cloud-core model [Thomas *et al.*, 2021], but a Gaussian model can not account for highly non-Gaussian fluctuations with heavy tails.

The statistical model reproduces both Gaussian and non-Gaussian relaxation quantitatively after the initial transient, as these relaxations are seen in DNS. Whether any one of, or both, these relaxations follow upon cloud-edge mixing and evaporation in the atmosphere is an open question. One may speculate whether the persisting heavy tail of the Lagrangian supersaturation PDF at moderate Damköhler numbers [Fig. (3.4a)] is more representative of atmospheric relaxation than the Gaussian relaxation at low Damköhler numbers [Fig. (3.3a)]. Some support for this hypothesis is provided by that the range of turbulent scales at a cloud edge is vast, and entails mixing-evaporation dynamics parameterized by very large Damköhler numbers. I emphasize that this speculation is based on simulation results, and that it is

not clear in which way these results generalize to atmospheric conditions. A direct generalization is not possible, because the simulation results are affected by the boundaries of the simulation domain. It seems possible to achieve a better understanding of atmospheric supersaturation relaxation through simulations of transient mixing-evaporation dynamics in the future. One must then compute the Lagrangian supersaturation PDF locally during the initial transient, before it has been affected by the boundaries of the simulation domain.

As stated above, the statistical-model results in Section 3.2.5 have been computed using a value for the empirical constant C_ϕ estimated from the DNS of Kumar *et al.* [2012]. See Appendix A for details on this estimate. The constant C_ϕ appears in Eq. (3.7), and reflects that the statistical model employs the spectral relaxation model of Fox [1995] to compute the supersaturation dissipation rate $\varepsilon_s(t)$. That C_ϕ is estimated from DNS used for comparison reduces the significance of the quantitative agreements observed in Figs. (3.3) and (3.4) to some extent. It should however be kept in mind that the agreements not only reflect that the evolution of supersaturation variance is accurately parameterized by C_ϕ . More importantly, the quantitative agreements reflect that the statistical model accurately describes effects of turbulent mixing and droplet phase change on the shape of the Lagrangian supersaturation PDF $\mathcal{F}_s(S; t)$.

For future development of the statistical model, it is worth considering the mapping closure of He & Zhang [2004], in which two-point statistics are used to infer the rate at which the mapping $X(\eta, t)$ evolves. With this mapping closure it is no longer necessary to estimate the empirical constant C_ϕ , because the spectral relaxation model is no longer needed to predict $\varepsilon_s(t)$. Furthermore, it seems as if the mapping closure of He & Zhang [2004] makes it possible to account for how droplet phase change modifies the rate at which turbulent mixing affects the mapping $X(\eta, t)$. The most important step towards a statistical model that is quantitative in the limit of large Damköhler numbers is however to account for Lagrangian correlations between supersaturation and condensation rate. In the Outlook of this thesis, I argue that it seems possible to do so with an extended probabilistic description that addresses the droplet-number densities of the air that surrounds the droplets. I also propose a cloud-core model that employs the new approximation of $\langle C(t) | s(\mathbf{x}, t) = S \rangle$ in Eq. (3.8) to describe droplet phase change. With this approximation it becomes possible to analyze the relaxed

supersaturation dynamics of cloud cores in a new way.

4 Angular dynamics of small crystals in flow

Papers B and C are devoted to the angular dynamics of small neutrally buoyant particles that possess certain symmetries. The results are valid in the limit of zero Reynolds number (1.18), which ensures that the particles move in Stokes flow. It is the linearity of the Stokes equations (1.27) that allows for the theory in Paper B, where we predict the angular dynamics of small particles that possess a rotation symmetry, and one or several mirror symmetries. In paper C we verify a theoretical prediction of Paper B experimentally, by showing that a triangular platelet spins and tumbles like a spheroid in a simple shear flow. Its angular motion is therefore in the form of Jeffery orbits, and described by one parameter.

4.1 Background

In Section 1.1.4 I explained that – in the limit of zero Reynolds number – the presence of a particle implies a Stokes problem. The Stokes problem of a particle is the problem of finding a solution to Stokes equations (1.27) with boundary conditions at the particle surface. Papers B and C consider particles with no-slip boundary conditions, which means that the flow moves together with the particle where the flow and the particle meet.

Boundary conditions are not only required at the particle surface, but also at large distances from the position $\mathbf{x}^{(o)}$ of the particle. This position moves together with the particle. It is not necessarily the center of mass of the particle, because there are other special points on a particle in Stokes flow. The center of hydrodynamic resistance and the center of hydrodynamic mobility are other special points [Kim & Karrila, 1991]. The particle does not affect the flow at large distances from itself. But the particle induces a disturbance flow

$$\mathbf{u}'(\mathbf{x}, t) = \mathbf{u}(\mathbf{x}, t) - \mathbf{u}^{(\infty)}(\mathbf{x}, t) \quad (4.1)$$

that is non-zero in its vicinity. Here, $\mathbf{u}^{(\infty)}(\mathbf{x}, t)$ denotes the ambient flow, which equals the undisturbed flow only at large distances from the particle. The boundary conditions at the surface S_p of the particle, and far away from

the particle are given by

$$\mathbf{u}(\mathbf{x}, t) = \mathbf{v}^{(o)} + \boldsymbol{\omega} \times (\mathbf{x} - \mathbf{x}^{(o)}) \quad \text{at } S_p, \quad \text{and} \quad (4.2a)$$

$$\mathbf{u}(\mathbf{x}, t) \rightarrow \mathbf{u}^{(\infty)}(\mathbf{x}, t) \quad \text{in the limit } |\mathbf{x} - \mathbf{x}^{(o)}| \rightarrow \infty. \quad (4.2b)$$

Here, $\mathbf{v}^{(o)}$ is the velocity of $\mathbf{x}^{(o)}$, and $\boldsymbol{\omega}$ is the angular velocity of the particle.

By solving the Stokes equations (1.27) with the boundary conditions in Eqs. (4.2), one finds the hydrodynamic force \mathbf{F} and the hydrodynamic torque $\boldsymbol{\tau}^{(o)}$ with respect to $\mathbf{r}^{(o)}$ that the fluid exerts. The change in translational and angular velocity can then be obtained if the mass and inertia tensor of the particle are known, using Eqs. (1.24) if $\mathbf{r}^{(o)}$ is the particles center of mass.

The ambient flow around the particle is roughly linear if its flow gradient $\mathbb{A}(\mathbf{x}, t)$, with components

$$A_{ij} = \frac{\partial u_i^{(\infty)}}{\partial x_j}, \quad (4.3)$$

varies only on lengths that are large compared to the particle size. In the case of a turbulent flow, this means that the particle size must be much smaller than the Kolmogorov length η . If the ambient flow is linear, the torque and force upon a particle in Stokes flow depend linearly upon the ambient translation, rotation and strain. I denote the rate-of-strain tensor by \mathbb{S} , and the anti-symmetric part of the flow gradient by \mathbb{O} :

$$\mathbb{S} = \frac{1}{2}(\mathbb{A} + \mathbb{A}^\top) \quad \text{and} \quad \mathbb{O} = \frac{1}{2}(\mathbb{A} - \mathbb{A}^\top). \quad (4.4)$$

The anti-symmetric part of the flow gradient is connected to the rotation $\boldsymbol{\Omega}$ of the ambient flow, because

$$\Omega_i = -\frac{1}{2} \varepsilon_{ijk} O_{jk}. \quad (4.5)$$

The linear dependences of the force and torque can be written [Kim & Karrila, 1991]:

$$\begin{bmatrix} \mathbf{F} \\ \boldsymbol{\tau}^{(o)} \end{bmatrix} = \mu \begin{bmatrix} \mathcal{A} & \mathcal{B}^\top & \mathcal{G} \\ \mathcal{B} & \mathcal{C} & \mathcal{H} \end{bmatrix} \begin{bmatrix} \mathbf{u}^{(\infty)} - \mathbf{v}^{(o)} \\ \boldsymbol{\Omega} - \boldsymbol{\omega} \\ \mathbb{S} \end{bmatrix}. \quad (4.6)$$

Here, $\mu = \rho \nu$ denotes the dynamic viscosity of the fluid. Furthermore, \mathcal{A} , \mathcal{B} , and \mathcal{C} are rank-2 tensors and \mathcal{G} and \mathcal{H} are rank-3 tensors. The tensors that map the components of the ambient flow to the force and torque on the particle in Eq. (4.6) are called resistance tensors. They are determined by the shape and orientation of the particle, and therefore fixed in a frame that moves together with the particle. All but \mathcal{A} depends on the choice of reference point $\mathbf{r}^{(o)}$ [Brenner & O'Neill, 1972]. All rank-2 tensors except \mathcal{B} are symmetric. However, there is one unique point in the particle frame at which \mathcal{B} is symmetric as well, the hydrodynamic center of resistance [Kim & Karrila, 1991].

A very small particle has very little translational and rotational inertia. Denoting the particle density by ρ_p and the linear size of the particle by a , the mass and inertia tensor scales as $m \sim \rho_p a^3$ and $\mathbb{I} \sim \rho_p a^5$. Inserting the hydrodynamic force and torque from Eqs. (1.24) into Eq. (4.6), one finds that the force and torque vanishes as the particle size tends to zero. In this overdamped limit, one finds the translational and angular dynamics by inserting $\mathbf{F} = \boldsymbol{\tau}^{(o)} = 0$ into Eq. (4.6). The translational velocity $\mathbf{v}^{(o)}$ and angular velocity $\boldsymbol{\omega}$ of a particle is therefore known in terms of its resistance tensors and ambient flow.

4.1.1 Jeffery orbits for spheroidal particles

In 1922, G. B. Jeffery published a well-known paper in which he solved an important Stokes problem for an ellipsoidal particle [Jeffery, 1922]. He considered a linear ambient flow and computed the disturbance flow caused by the presence of a neutrally buoyant ellipsoidal particle that translates together with the ambient flow. From this solution he found the angular velocity of the ellipsoid in the overdamped limit.

A special case of ellipsoids are spheroids. For a spheroid, I introduce a particle-fixed basis $[\mathbf{q}, \mathbf{p}, \mathbf{n}]$ at the particle center, as in Fig. (4.1). The surface of a spheroid is given by $\mathbf{x} = x_q \mathbf{q} + x_p \mathbf{p} + x_n \mathbf{n}$ for which

$$\frac{x_n^2}{(a/2)^2} + \frac{x_p^2 + x_q^2}{(b/2)^2} = 1, \quad (4.7)$$

where a and b denote the distance from pole to pole and the diameter of the spheroid. These distances define the aspect ratio $\lambda = a/b$ of the spheroid.

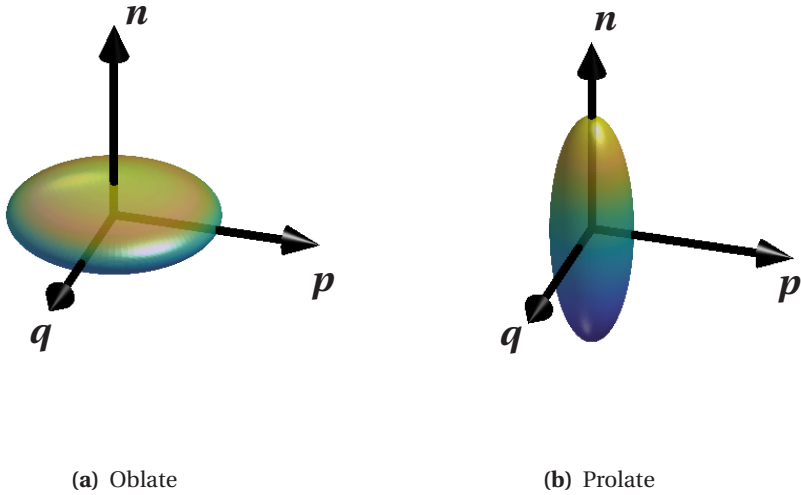


Figure 4.1: Two spheroids of different aspect ratios. The left spheroid is oblate with aspect ratio $\lambda = 1/3$, the right spheroid is prolate with aspect ratio $\lambda = 3$. The particle-fixed basis is placed at the center of the spheroid, with \mathbf{n} pointing along the symmetry axis.

Spheroids for which $\lambda < 1$ are oblate (Fig. 4.1a), and spheroids for which $\lambda > 1$ are prolate (Fig. 4.1b).

Since the shape of a spheroid is fully described by its aspect ratio, the aspect ratio determines its resistance tensors in Eq. (4.6). Accordingly, the motion that G. B. Jeffery found for a spheroid in the overdamped limit is described by a single shape parameter

$$\Lambda = \frac{\lambda^2 - 1}{\lambda^2 + 1}. \quad (4.8)$$

This shape parameter is negative for oblate spheroids, positive for prolate spheroids, and equals zero for spheres. It is bounded to the interval $[-1, 1]$, so that $\Lambda = -1$ for a totally flat disc, and $\Lambda = 1$ for an infinitely thin rod. In terms of Λ , the angular velocity that Jeffery found for a spheroid reads

$$\boldsymbol{\omega} = \boldsymbol{\Omega} - \Lambda(\mathbf{S}\mathbf{n}) \times \mathbf{n}. \quad (4.9)$$

It can be seen that the angular velocity depends on the aspect ratio and orientation of the spheroid. For a given orientation and aspect ratio, the

angular velocity is determined by the combined effect of flow rotation and strain.

A Jeffery orbit is the periodic angular motion that Jeffery derived for a spheroid in a simple shear flow. In a lab-fixed coordinate system $[\mathbf{e}_1, \mathbf{e}_2, \mathbf{e}_3]$ that translates with the spheroid's center, a simple shear flow with flow direction \mathbf{e}_1 , shear direction \mathbf{e}_2 and vorticity direction $-\mathbf{e}_3$ provides the ambient flow velocity:

$$\mathbf{u}^{(\infty)}(\mathbf{x}, t) = \gamma y \mathbf{e}_1. \quad (4.10)$$

Here, γ denotes the shear rate of the simple shear, and $y = \mathbf{e}_2^T \mathbf{x}$ is the position component in the shear direction. The simple shear flow is important, because it is easily obtained in laboratory experiments and approximates flows in industry [Dealy & Wissbrun, 2012].

Jeffery concluded that a spheroid translates with the ambient flow at its center of mass, with a spinning and tumbling motion given by

$$\dot{\phi} = -\frac{1}{2}\gamma(\Lambda \cos 2\phi + 1), \quad (4.11a)$$

$$\dot{\theta} = -\frac{1}{4}\gamma\Lambda \sin 2\phi \sin 2\theta, \quad \text{and} \quad (4.11b)$$

$$\dot{\psi} = \frac{1}{2}\gamma\Lambda \cos 2\phi \cos \theta. \quad (4.11c)$$

Here, I introduced the Euler-angles of Goldstein [1980] to express the particle orientation in the lab-fixed frame:

$$\mathbf{n} = \sin \phi \sin \theta \mathbf{e}_1 - \cos \phi \sin \theta \mathbf{e}_2 + \cos \theta \mathbf{e}_3, \quad (4.12a)$$

$$\begin{aligned} \mathbf{p} = & (-\sin \psi \cos \phi - \cos \theta \sin \phi \cos \psi) \mathbf{e}_1 \\ & + (-\sin \psi \sin \phi + \cos \theta \cos \phi \cos \psi) \mathbf{e}_2 \\ & + \cos \psi \sin \theta \mathbf{e}_3, \quad \text{and} \end{aligned} \quad (4.12b)$$

$$\mathbf{q} = \mathbf{p} \times \mathbf{n}. \quad (4.12c)$$

Integrating Eqs. (4.11a) and (4.11b) from an orientation $[\phi, \theta, \psi] = [0, \theta_0, \psi_0]$ at $t = 0$, one finds that the symmetry axis of the spheroid tumbles on a peri-

odic orbit in which

$$\tan \phi = -\sqrt{\frac{1+\Lambda}{1-\Lambda}} \tan \left[\frac{1}{2} \gamma \sqrt{1-\Lambda^2} t \right], \quad \text{and} \quad (4.13a)$$

$$\tan \theta = \tan \theta_0 \sqrt{\frac{\Lambda+1}{\Lambda \cos 2\phi + 1}}. \quad (4.13b)$$

This periodic orbit is called a Jeffery orbit. The orbit constant [Kim & Karrila, 1991]

$$C = \tan \theta \sqrt{\Lambda \cos 2\phi + 1} \quad (4.14)$$

is a conserved function of ϕ and θ . It specifies which of the infinitely many Jeffery orbits that a spheroid with shape parameter Λ tumbles on. From Eqs. (4.13a) and (4.13b), we find that the period of a Jeffery orbit is given by

$$T_J = -\frac{4\pi}{\gamma \sqrt{1-\Lambda^2}}, \quad (4.15)$$

and that this period is the same for all Jeffery orbits that a given spheroid can tumble upon. While tumbling, a spheroid has a spinning motion given by Eq. (4.11c). In general, the period of ψ is not the same as the period of the Jeffery orbit, and the initial state of three Euler angles $[0, \theta_0, \psi_0]$ is not adopted again within a finite time. Therefore, the full angular motion of a spheroid in a simple shear is not periodic, but quasiperiodic [Einarsson *et al.*, 2016]. Jeffery-orbit theory has been successfully applied within the field of rheology, where it has been used to predict the intrinsic viscosity of dilute particle suspensions [Leal & Hinch, 1971; Kim & Karrila, 1991].

Fig. (4.2) shows various aspects of the orbiting motion implied by Jeffery's angular velocity in Eq. (4.9), for the simple shear flow defined by Eq. (4.10). Fig. (4.2a) shows the evolution of ϕ for prolate and oblate spheroids with $\Lambda = \pm 12/13$. Since $|\Lambda|$ is the same, the Jeffery orbits have the same period. We note that ϕ decreases monotonously with γt , and is independent of the orbit constant C . Prolate spheroids spend a long time aligned with ϕ approximately equal to odd multiples of $\pi/2$, which means that the symmetry axis aligns with the flow direction for a long time. Oblate spheroids spend a long time aligned with ϕ approximately equal to even multiples of $\pi/2$, which means that the symmetry axis aligns with the shear direction for a

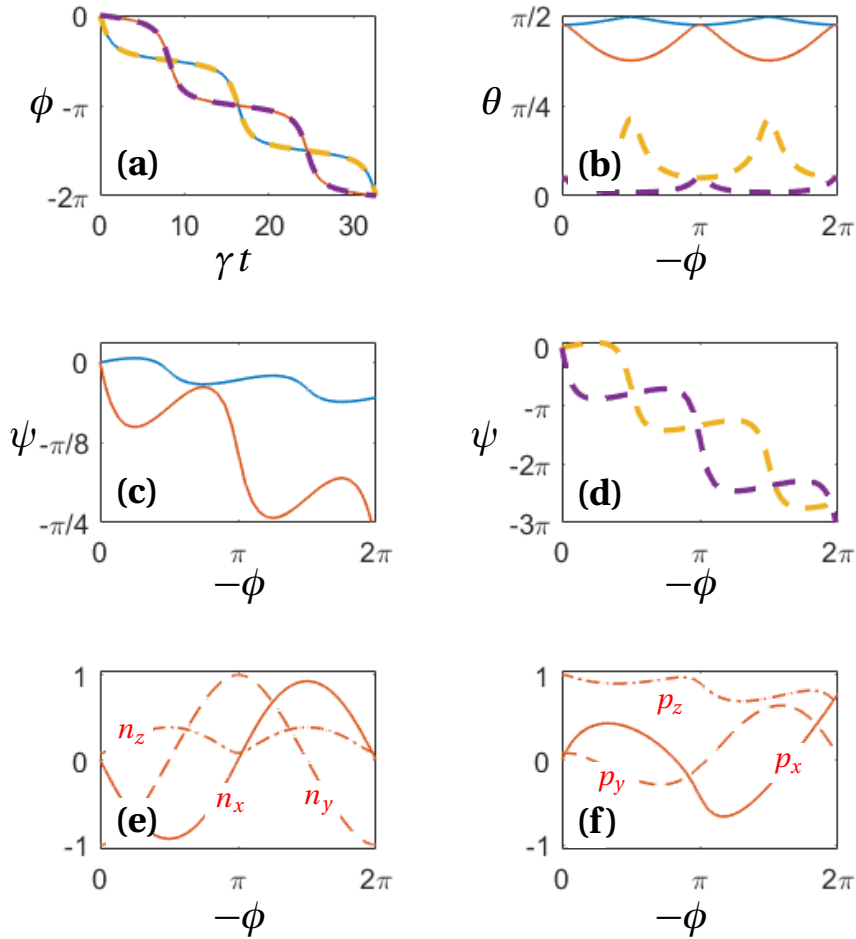


Figure 4.2: Jeffery orbits and spin in a simple shear. Blue and yellow are for a prolate spheroid with aspect ratio $\lambda = 5$ and shape parameter $\Lambda = 12/13$, red and purple are for an oblate spheroid with aspect ratio $\lambda = 1/5$ and shape parameter $\Lambda = -12/13$. Blue and red are tumbling orbits, initiated with $\theta_0 = 9\pi/19$ and orbit constants $C = 16.7$ and $C = 3.3$. Yellow and purple are log-rolling orbits, initiated with $\theta_0 = \pi/20$ and orbit constants $C = 0.22$ and $C = 0.04$.

long time. Fig. (4.2b) shows the evolution of θ for the same spheroids. Blue and red are tumbling orbits, in which \mathbf{n} tumbles in the flow-shear plane.

Purple and yellow are log-rolling orbits, in which the spheroid remains with its symmetry axis close to the negative vorticity direction. It can be seen that θ does not change sign, which means that \mathbf{n} does not cross the flow-shear plane. The evolution of ψ is seen in Figs. (4.2c) and (4.2d). The periods of spinning and tumbling are different, so the period of ψ differs from the period of ϕ and θ . The tumbling spheroids spin substantially less than the log-rolling ones. Figs. (4.2e) and (4.2f) show the components of \mathbf{n} and \mathbf{p} in the lab-fixed basis. It can be seen that \mathbf{p} does not evolve with the same period as \mathbf{n} , which reflects the quasiperiodicity of the spinning and tumbling motion.

4.1.2 Particles with symmetries

The resistance tensors that map the ambient flow to the force and torque upon a particle in Eq. (4.6) depend only on particle shape and orientation. It follows that any symmetries in the shape of a particle are reflected in its resistance tensors: If the surface of a particle is invariant under an orthogonal transformation (a rotation or a reflection), its resistance tensors are constrained by the invariance [Happel & Brenner, 1983].

Fig. (4.3a) shows a particle at rest in a purely straining flow ($\mathbf{u}^{(\infty)} = \mathbf{0}$, $\mathbf{\Omega} = \mathbf{0}, \mathbf{S} \neq \mathbf{0}$). For this particle, we have

$$\boldsymbol{\tau}^{(o)} = \mu \mathcal{H} : \mathbf{S}. \quad (4.16)$$

Now, transform the Stokes problem that the particle presents by an orthogonal transformation \mathbb{T} . The transformation can be either a rotation [Fig. (4.3b)], or a reflection [Fig. (4.3c)]. In the transformed Stokes problem, the rate-of-strain tensor is $\mathbb{T}\mathbf{S}\mathbb{T}^\top$, and the torque upon the particle is $\det[\mathbb{T}]\mathbb{T}\boldsymbol{\tau}^{(o)}$ (the torque is a pseudovector and transforms with the determinant of \mathbb{T} , $\det[\mathbb{T}]$). The particle in Fig. (4.3) has a symmetry that ensures that its surface is neither affected by the rotation in Fig. (4.3b), nor by the reflection in Fig. (4.3c). This implies that the resistance tensors in Eq. (4.6) are not affected by the transformations. In particular, we have

$$\det[\mathbb{T}]\mathbb{T}\boldsymbol{\tau}^{(o)} = \mu \mathcal{H} : (\mathbb{T}\mathbf{S}\mathbb{T}^\top) \quad (4.17)$$

for both the reflection and the rotation. By combining Eqs. (4.16) and (4.17), one finds that any orthogonal transformation \mathbb{T} that leaves the surface of

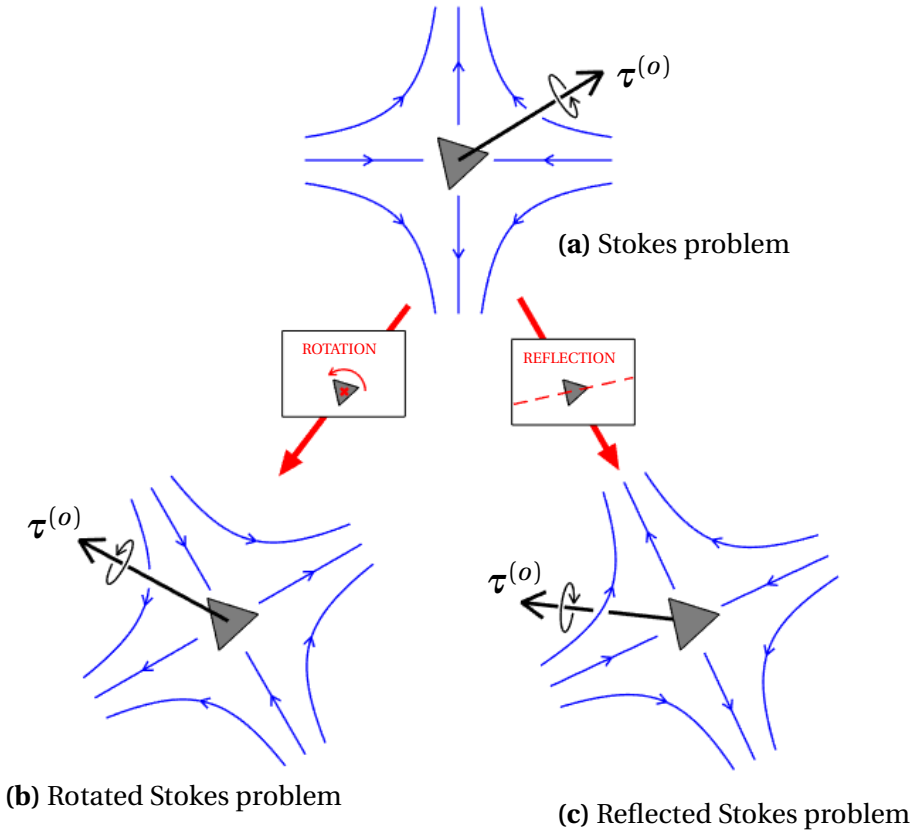


Figure 4.3: (a) Stokes problem implied by a triangular particle at rest in a purely straining flow ($\mathbf{u}^{(\infty)} = \mathbf{0}$, $\mathbf{\Omega} = \mathbf{0}$, $\mathbb{S} \neq \mathbf{0}$). Stream lines are given in blue, and the torque $\tau^{(o)}$ is schematically illustrated by a black arrow. The same Stokes problem is rotated in (b), and reflected in (c). The particle possesses symmetries, ensuring that its surface is not affected by the transformations. The symmetries imply constraints on the resistance tensor \mathcal{H} of the particle, and therefore on the linear relation between the ambient strain \mathbb{S} and the torque $\tau^{(o)}$ (see text).

the particle invariant implies a constraint on the resistance tensor \mathcal{H} of the

particle. The component \mathcal{H}_{ijk} of \mathcal{H} must fulfill

$$\mathcal{H}_{ijk} = \det[\mathbb{T}] T_{i'j'} T_{kk'} \mathcal{H}_{i'j'k'}, \quad (4.18)$$

where T_{ij} denotes a component of \mathbb{T} .

I have now explained how one may transform a Stokes problem with a straining flow, and deduce constraints on the resistance tensor \mathcal{H} of a symmetrical particle by analyzing how its torque transforms. Analogous constraints can be deduced for the resistance tensor \mathcal{G} , by analyzing how the force transforms instead. In the same way, one may conclude constraints on all resistance tensors in Eq. (4.6), by analyzing the force and torque upon particles at rest in purely translational flow ($\mathbf{u}^{(\infty)} \neq \mathbf{0}, \mathbf{\Omega} = \mathbf{0}, \mathbf{S} = \mathbf{0}$), and in purely rotational flow ($\mathbf{u}^{(\infty)} = \mathbf{0}, \mathbf{\Omega} \neq \mathbf{0}, \mathbf{S} = \mathbf{0}$). For particles whose surfaces do not change under an orthogonal transformation \mathbb{T} , one finds these constraints:

$$\mathcal{A}_{ij} = T_{i'j'} \mathcal{A}_{i'j'} \quad (4.19a)$$

$$\mathcal{B}_{ij} = \det[\mathbb{T}] T_{i'j'} \mathcal{B}_{i'j'} \quad (4.19b)$$

$$\mathcal{G}_{ijk} = T_{i'j'} T_{kk'} \mathcal{G}_{i'j'k'} \quad (4.19c)$$

$$\mathcal{C}_{ij} = T_{i'j'} \mathcal{C}_{i'j'} \quad (4.19d)$$

$$\mathcal{H}_{ijk} = \det[\mathbb{T}] T_{i'j'} T_{kk'} \mathcal{H}_{i'j'k'}. \quad (4.19e)$$

4.2 My work

My work on the angular dynamics of small crystals in flow has resulted in Papers B and C. In Paper B we apply the symmetry constraints in Eqs. (4.19) to find the angular motion of particles with orthogonal symmetries in Stokes flow. In Paper C, a prediction of Paper B is verified experimentally, namely that an equilateral triangle has the same angular dynamics as an equivalent spheroid. Since the triangle has corners, it is possible to observe how it spins, while tumbling on a Jeffery orbit in a simple shear flow.

4.2.1 Application of symmetry constraints

In Paper B, we use the constraints in Eqs. (4.19) to show that a small neutrally buoyant particle with a rotation symmetry and a mirror plane that contains the axis of the rotation symmetry [Fig. 2(a) of Paper B] has the same angular motion as a small neutrally buoyant spheroid. The rotation symmetry can

be discrete, but must then be N -fold with $N > 2$. Just as for spheroids, the angular motion is described by a single shape parameter Λ . The angular velocity is given by Eq. (4.9), if one defines a particle-fixed basis $[\mathbf{q}, \mathbf{p}, \mathbf{n}]$ with \mathbf{n} pointing along the axis of rotation symmetry.

We also show that a rotationally symmetric particle that lacks the above mentioned mirror plane, but has a mirror plane orthogonal to the axis of the rotation symmetry [Fig. 2(b) of Paper B], has a motion governed by two additional parameters, Γ and Ψ . In a simple shear, Eq. (4.10), the Euler-angles in Eq. (4.12) evolve according to:

$$\dot{\phi} = -\frac{1}{2}\gamma(\Lambda \cos 2\phi + 1 - \Psi \sin 2\phi \cos \theta), \quad (4.20a)$$

$$\dot{\theta} = -\frac{1}{4}\gamma(\Lambda \sin 2\phi \sin 2\theta + 2\Psi \cos 2\phi \sin \theta), \quad \text{and} \quad (4.20b)$$

$$\dot{\psi} = \frac{1}{2}\gamma(\Lambda \cos 2\phi \cos \theta - \Gamma \sin 2\phi \sin^2 \theta - \Psi \sin 2\phi). \quad (4.20c)$$

If $\Psi = 0$, the symmetry axis of the particle tumbles on a Jeffery orbit, just as it does for a spheroid. However, the particle spins differently if $\Gamma \neq 0$. If $\Psi \neq 0$, the symmetry axis does not move on a periodic orbit. Instead, the symmetry axis tends to a fixed orientation, at which it remains indefinitely. In Appendix C I construct model particles with small non-zero values of Γ and Ψ from a set of spheroids. Such multi-spheroid particles were constructed by Bretherton [1962], in order to give examples of qualitatively different particle dynamics. One particle that I construct looks like a water wheel. It has a non-zero value of Γ , but a zero value of Ψ . Another particle resembles two propellers of opposite chirality, sharing the same symmetry axis. Both Γ and Ψ are non-zero for this particle. In Appendix C, I use the multi-spheroid particles to argue for an intuitive understanding of how Γ and Ψ affect the dynamics of a particle.

Bretherton [1962] showed that a particle with a 4-fold rotation symmetry and a reflection symmetry in a plane that contains the axis of rotation symmetry has the angular motion of an equivalent spheroid. With Paper B, we generalize the symmetry requirements of Bretherton [1962], by showing that a N -fold rotation symmetry is enough, provided $N > 2$.

4.2.2 Experimentally observed Jeffery spin

Particles shaped as equilateral triangles, such as the particle in Fig. 1 of Paper C, have a rotation symmetry, and three mirror planes that contain the axis of rotation symmetry. The theory of Paper B predicts that small such particles tumble on Jeffery orbits in a simple-shear, just like small spheroids. As opposed to spheroids, triangles have corners. Their spin can therefore be observed in an experiment, and this was the motivation of Paper C. In this paper, we observe the spinning and tumbling motion of triangles in a micro channel. It can be seen in Paper C that the angular motion is indeed given by Eqs. (4.11), both for log-rolling and tumbling orbits.

The experiments were performed by M. V. Kumar. The triangular particle is about $1 \mu\text{m}$ thick and has a side length of $10 \mu\text{m}$. The micro channel is a 40 mm long, 2.5 mm wide, and $200 \mu\text{m}$ high molded rectangular cavity. Since the length and width of the channel are large compared to the channel height, the ambient flow profile near the channel center is one dimensional. The flow profile is parabolic, but approximates a simple shear in the vicinity of the particle. We define the shear Reynolds number as

$$\text{Re}_s = \gamma a^2 / \nu, \quad (4.21)$$

where γ is the shear rate, a is the center-to-corner distance of the triangular particle, and ν is the kinematic viscosity. The fluid is water with a dissolved polyethylene glycol, ensuring neutral particle buoyancy and large enough viscosity for Stokes-flow dynamics. The viscosity of the solution is $\nu = 76.3 \text{ mm}^2/\text{s}$. In a typical experiment we have $\text{Re}_s \sim 10^{-6}$, and we expect that such values are small enough to ensure that the particle moves in Stokes flow.

I analyzed the raw data, particle videos recorded by M. V. Kumar. In the analysis, I made use of that Stokes equations are time reversible [Bretherton, 1962], but that Navier-Stokes equations are not [Pope, 2000]. This means that one may ensure that the Reynolds number is small enough in the experiment, by reverting the flow through the micro channel. In the zero-Reynolds number limit, the particle must trace its angular orbit backwards, so that the Euler angles (ϕ, θ, ψ) in Eqs. (4.12) are functions of particle position only. If the Euler angles extracted from the recorded particle videos are uniquely determined by particle position, one can be sure that Re_s is so small that the flow is well approximated by a Stokes flow.

The value of Re_s can be decreased by reducing the flow rate through the

channel. One caveat is that the flow rate can not be so small that Brownian motion causes the orientations and positions of particles to diffuse significantly. This means that the flow rate must be small enough to ensure a Stokes flow, but not so small that effects of particle diffusion become important in comparison to the dynamics dictated by the flow. The time scale of the flow is γ^{-1} . The smallest diffusive time scale τ_D is proportional the temperature T , and to the resistance tensor \mathcal{C} that gives the torque upon a particle that rotates in a quiescent flow ($\mathbf{u}^{(\infty)} = \mathbf{0}$, $\mathbf{\Omega} = \mathbf{0}$, $\mathbb{S} = \mathbf{0}$) [Leal & Hinch, 1971]. The time-scale ratio forms the Péclet number

$$\text{Pe} = \gamma\tau_D, \quad (4.22)$$

which must be large enough for the flow dynamics to dominate over Brownian motion. In Paper C, we estimate $\text{Pe} \sim 10^5$, substantially larger than unity, by modeling the triangular particle as a thin circular disc.

The recorded particle videos allow us to reconstruct the full three-dimensional motion of the triangular particles from their corner positions in consecutive video frames. We identify several particle trajectories that are reversible, some of them are shown in Paper C. Since Brownian motion and effects of non-zero Re_s are absent for these trajectories, the symmetries of our particles ensure that they move on Jeffery orbits. Indeed, the reversible orbits shown in Paper C are well described by Jeffery's theory. By fitting Jeffery orbits to the observed angular trajectories, we infer that our triangular particles move as oblate spheroids with shape parameter $\Lambda \approx -0.95$. By showing that particles shaped as equilateral triangles move on Jeffery orbits in a simple shear flow, we verify that an axisymmetric particle that with a mirror plane that contains the axis of rotation symmetry has the same angular dynamics as an equivalent spheroid.

4.3 Discussion

The theory of Paper B extends that of Bretherton [1962], and makes it possible to predict the angular dynamics of more generally shaped particles. The symmetry requirements of Bretherton [1962] include spheroids and more general bodies of revolution, but exclude triangular and hexagonal particles. Bretherton [1962] concludes that the former particles spin and tumble like spheroids, and we conclude that the latter particles do so as well. Our results

are therefore important for the angular dynamics of microorganisms with cross sections in the form of regular polygons, such as the triangular algae of the Genus *Triceratium* [Guiry & Guiry, 2016]. Nguyen *et al.* [2011] used numerical simulations to test whether a plankton with spines can be modeled as a spheroid. They concluded that a spheroid model is sound, because the symmetry axis of a particle composed by a disc and 24 spines moves on a Jeffery orbit in numerical simulations. The results of Paper B imply that the model is not only sound. The model is perfect, because the spined particle is rotationally symmetric and possesses several mirror planes that contain the axis of rotation symmetry.

Our results in Paper B are of some relevance for angular dynamics of ice crystals in clouds, which are often hexagonal. Ice crystals in clouds are commonly modeled as spheroids, with terms that describe inertial effects added to the torque that they experience in Stokes flow [Jucha *et al.*, 2018; Gustavsson *et al.*, 2019, 2020; Anand *et al.*, 2020]. We show that the Stokes-flow solution must indeed be obtained in the inertia-free limit of these equations. It should however be noted that inertial effects are important for the orientational distribution of ice crystals in clouds, as a consequence of that the ice crystals are much heavier than the air. Recent results indicate that settling causes the orientational distribution of ice crystals to be dominated by inertial effects in most parameter regimes of interest [Gustavsson *et al.*, 2020].

Although axisymmetric particles with a mirror plane that contains the axis of rotation symmetry spin and tumble as equivalent spheroids, such particles may not translate as spheroids. This has recently been concluded by Ishimoto [2020]. The author shows that such particles can have a slip velocity $\mathbf{v}^{(s)} - \mathbf{u}^{(\infty)}$ that is described using two parameters in the overdamped limit. The slip velocity is due a coupling between the translational motion and strain, relying on a non-zero resistance tensor \mathcal{G} . The coupling imposes a force upon a particle at rest in a purely straining flow ($\mathbf{u}^{(\infty)} = \mathbf{0}, \mathbf{\Omega} = \mathbf{0}, \mathbb{S} \neq \mathbf{0}$). Ishimoto [2020] show that the combined translational and angular dynamics in a simple shear flow is nevertheless periodic in the overdamped limit. The center of hydrodynamic resistance translates periodically with the same period as the tumbling period of the symmetry axis, the period of the Jeffery orbit. The coupling between translational motion and strain vanishes if one imposes a mirror plane that is orthogonal to the axis of rotation symmetry. Therefore, both the translational and angular dynamics of a particle that

possesses all symmetries considered in Paper B are of the same form as they are for spheroids.

Einarsson *et al.* [2015] show that the combined effects of fluid and particle inertia can cause a spheroid to tumble into a stable orientation in a simple shear flow. The results in Paper B indicate that a similar effect must be expected for particles with a discrete rotation symmetry, also when inertial effects are absent. Imperfections in a symmetry plane that contains the axis of rotation symmetry can namely give rise to non-zero values of Ψ , and Eqs. (4.20) tell us that non-zero values of Ψ cause a particle to tumble into a stable orientation.

The intrinsic viscosity of a dilute suspension of particles is determined by the orientational distribution of the particles [Kim & Karrila, 1991]. In the Outlook of this thesis I propose a study on the intrinsic viscosity of a suspension of non-zero Ψ particles. Here, I argue that the intrinsic viscosity of such a suspension is subject to a hysteresis effect, as a consequence of that the particles tumble into stable orientations.

5 Conclusions

In this thesis I have presented my work on the simultaneous mixing and evaporation at the edge of a turbulent cloud, and on the angular dynamics of small crystals in flow.

Cloud-edge mixing and evaporation was the topic of Chapter 2 and Paper A. A general conclusion is that one must take both the time scale for droplet evaporation and saturation of the air into account when analyzing the evolution of a cloud region. Simultaneous mixing and evaporation must therefore be described using two Damköhler numbers. A three-parameter description in terms of two Damköhler numbers and the volume fraction of cloudy air captures the central ingredients of mixing-evaporation dynamics – mixing, evaporation, and saturation of the air – and provide a simple way to understand results of Andrejczuk *et al.* [2006], Kumar *et al.* [2014, 2018, 2013, 2012], Korolev *et al.* [2016], and Pinsky *et al.* [2016b].

The homogeneous mixing line in a mixing diagram can be generalized to include mixing-evaporation processes with a non-zero fraction of completely evaporated droplets as well. This notion, together with the three-parameter description used in Paper A, makes it possible to infer dynamical information from empirical data above the homogeneous mixing line. Each point in the diagram corresponds to an equilibrated mixing-evaporation process, and the spatial scale of the processes increases as one moves upwards from the homogeneous mixing line. Furthermore, the three-parameter description makes it possible to formulate a multiscale theory for how the effects of mixing, evaporation, and saturation vary with spatial scale and position within the cloud.

In Paper A we derive a statistical model to compute our numerical results. The statistical model reproduces important observables in DNS of transient mixing and evaporation [Kumar *et al.*, 2014, 2012], but the supersaturation dynamics of the model is oversimplified. The oversimplified supersaturation dynamics prevents the model from reproducing transient heavy tails and Gaussian relaxation of the Lagrangian supersaturation PDF; the PDF of supersaturation at droplet positions.

In Chapter 3, I derive an improved statistical model that partially overcomes the deficiencies of the statistical model in Paper A. The improved model quantitatively reproduces the Lagrangian supersaturation PDF in

DNS at low Damköhler numbers, and after the initial transient at moderate Damköhler numbers. Analyzing the Lagrangian supersaturation PDF using the model, I conclude the following. First, Gaussian relaxation of the Lagrangian supersaturation PDF reflects a passive scalar behavior of supersaturation at low Damköhler numbers, but droplet phase change prevents Gaussian relaxation at moderate Damköhler numbers. Second, heavy tails of the Lagrangian supersaturation PDF observed by Kumar *et al.* [2014, 2013, 2012] during the initial transient correspond to the U-shaped Eulerian PDF of a passive scalar in the DNS of Eswaran & Pope [1988]. Third, heavy tails persisting after the initial transient are independent of Lagrangian correlations between supersaturation and condensation rate.

The angular dynamics of crystals in flow was the topic of Chapter 4 and Papers B and C. In Paper B we generalize a theoretical prediction of Bretherton [1962] by showing that axisymmetric particles spin and tumble like spheroids if they possess an N -fold rotation symmetry with $N > 2$, and a reflection symmetry in a plane that contains the axis of rotation symmetry. As a consequence, the angular dynamics of a small particle shaped as an equilateral triangle is in the form of a Jeffery orbit in a simple shear flow. Paper C verifies this prediction experimentally. The theoretical and experimental results are important for the angular dynamics of small microorganisms with rotation-symmetric cross sections.

The angular dynamics of rotation-symmetric particles with a reflection symmetry orthogonal to the axis of rotation symmetry is in general described by three parameters. Some such particles tumble as spheroids, but spin differently. Other such particles tumble differently and tend towards a fixed orientation in a simple shear flow.

6 Outlook

6.1 Further improved cloud-edge model

The improved statistical model in Chapter 3 reproduces the supersaturations of droplets in DNS at low Damköhler numbers quantitatively. It is therefore a natural starting point in the development of future models that are quantitative in the limit of large Damköhler numbers. The initial deviations in Fig. (3.4a) at $Da_s \sim 10$ support that inaccuracies in the dynamics of the model in Chapter 3 stem primarily from the closure for bounded Lagrangian supersaturation fluctuations in Eqs. (3.14b) and (3.14c). The most important step when deriving a further improved statistical model is therefore to replace this closure. To describe bounded Lagrangian supersaturation fluctuations at large values of Da_s , it is necessary to account for Lagrangian correlations between supersaturation and condensation rate, as explained in Section 3.2.3. Such correlations can not be accurately accounted for in the statistical model in Chapter 3, because the presence of nearby droplets is not addressed by the joint PDF \mathcal{F}_{sr^2} of droplets and supersaturation. In light of this, it appears as if significant improvements are possible with a probabilistic description that also addresses the droplet-number density at droplet positions. A model that describes Lagrangian correlations of supersaturation and droplet-number density can namely account for how saturation is maintained at the position of a droplet when there are many nearby droplets in its vicinity.

Correlated bounded fluctuations of two scalars can be described using mapping closures [Pope, 1991; Klimenko & Pope, 2003]. In the development of a statistical model that describes correlated fluctuations of supersaturation and droplet-number density, one must be aware of that droplet-number density represents a dilute mixture of droplets. Droplet-number density does therefore not obey an advection-diffusion equation, like Eq. (2.1) for supersaturation. This raises a problem, because advection-diffusion equations are assumed in the derivation of mapping closures. One must however expect that inhomogeneities in droplet-number density undergo a similar relaxation as inhomogeneities in supersaturation. This suggests that the joint relaxation of droplet-number density and supersaturation can be accurately reproduced using mapping closures, despite that droplet-number density is a dilute field.

6.2 Improved cloud-core models

It would be interesting to use the approximation $\langle C(t)|s = S \rangle$ of the average condensation rate conditional on supersaturation [Eq. (3.8)] in a statistical model for the cloud core. In present models for isobaric cloud-core dynamics, droplet phase change affects the supersaturations of droplets through the unconditionally averaged condensation rate [Sardina *et al.*, 2015; Paoli & Shariff, 2009; Siewert *et al.*, 2017]. This does not account for that a phase changing droplet exchanges water and latent heat locally, and therefore only with air whose supersaturation is the same as the supersaturation of the droplet. As a consequence, the models describe Gaussian scalar fluctuations that are directly inherited from a Gaussian forcing, because droplet phase change can not break the Gaussianity. It is therefore not possible to explore effects of droplet phase change on the Lagrangian supersaturation PDF using present cloud-core models. Such effects can however be explored if droplet phase change is modeled using the approximation $\langle C(t)|s = S \rangle$.

6.3 Three-parameter analysis of empirical data

In Paper A, we explain how a three-parameter description of cloud-edge mixing and evaporation makes it possible to infer mixing-evaporation histories of empirically observed droplet populations represented in mixing diagrams. In particular, one may infer a length scale L for each droplet population that, under certain assumptions, is characteristic for the mixing and evaporation that it has experienced. In order to demonstrate this new theory, we analyze one of the droplet populations reported by Beals *et al.* [2015] in Paper A. It would be interesting to apply the theory systematically in the future, using additional measurements that make it possible to relate inferred length scales L to the positions of droplet populations within the cloud. Does the length scale increase with distance to the cloud edge? The answer to this question would indicate whether or not the three-parameter description and its associated theory are correct and useful when characterizing mixing and evaporation at different spatial scales.

6.4 Intrinsic viscosity of a suspension of particles with non-zero Ψ

A successful application of Jeffery's theory for the angular dynamics of spheroids in a simple shear, Eqs. (4.11), is on the intrinsic viscosity of a dilute suspension of small spheroids. Leal & Hinch [1971] were able to derive this viscosity for identical spheroids whose orientations change as a consequence of deterministic Stokes-flow dynamics and stochastic Brownian noise. Brownian noise adds a diffusion term to the Fokker-Planck equation for the PDF that describes the orientational distribution of the spheroids. This PDF is otherwise only subject to deterministic drift, reflecting the periodic Jeffery orbits in Eqs. (4.13). The drift and noise combined give rise to an equilibrium distribution, for which the intrinsic viscosity can be computed. The fluid is non-Newtonian (shear thinning), since the particles orient themselves so that they contribute less to the stress at large shear rates [Kim & Karrila, 1991].

How does the orientational distribution evolve for particles with non-zero Ψ ? One must expect that there is an equilibrium distribution, reflecting that each individual particle is driven towards a steady-state orientation. The steady-state distribution is therefore qualitatively different at $\Psi \neq 0$, because it does not reflect noise combined with a periodic particle motion. Instead, it reflects noise around a steady-state orientation. One must expect that this gives rise to a hysteresis effect, in which the intrinsic viscosity at a given time depends on the history of shear rates. If the shear rate has been constant for a long time, the intrinsic viscosity is determined by particles that fluctuate around their steady-state orientations. But stable steady states become unstable if the flow is reversed [Bretherton, 1962], so after a flow reversal the intrinsic viscosity must be determined by particles tumbling out of an unstable steady state for some time. The evolution of the intrinsic viscosity from the instant of the reversal is determined by the shear rate, the Péclet number, and the values of Λ and Ψ , because these factors determine how the orientational distribution evolves. It may be possible to learn about the intrinsic-viscosity dynamics by analyzing the Fokker-Planck equation for the PDF of particle orientations, which is straightforward to formulate [Kim & Karrila, 1991].

7 Appendices

A Complete description of simulations in Section 3.2.5

Details of the statistical-model simulations in Section 3.2.5 are best explained by dividing them into two classes. One class consists of parameters and equations required by the spectral relaxation model of Fox [1995], and used to compute the supersaturation dissipation rate $\varepsilon_s(t)$ in Eq. (3.7). The other class consists of parameters that describe all initial conditions that are not part of the spectral relaxation model.

A.1 Initial conditions not part of the spectral relaxation model

The initial distributions $\mathcal{F}_{sr^2}(S, R^2; t)$ and $f_s(S; t)$ are extracted from Kumar *et al.* [2012]. The initial Eulerian supersaturation PDF $f_s(S; t = 0)$ is obtained by sampling the initial cloud slab of Kumar *et al.* [2012] uniformly over the interval $-\frac{1}{2}L < x < \frac{1}{2}L$. The normalized supersaturation profile of the initial cloud slab of Kumar *et al.* [2012] is given by

$$s(x, t = 0) = (1 + s_c) \exp \left[-\zeta_1 \left(\frac{x}{L} \right)^{\zeta_2} \right] - 1, \quad (7.1)$$

with parameters $s_c = 0.1$, $\zeta_1 = 1410$, and $\zeta_2 = 6$. The initial droplet-size distribution of Kumar *et al.* [2012] is monodisperse, so all droplets are initialized with non-dimensional radius $r(t = 0) = 1$. The initial joint PDF \mathcal{F}_{sr^2} of droplets and supersaturation is therefore given by

$$\mathcal{F}_{sr^2}(S, R^2; t = 0) = \mathcal{F}_s(S; t = 0) \delta(R^2 - 1), \quad (7.2)$$

where $\delta(\dots)$ is Dirac's delta function.

The initial mapping $X(\eta, t = 0)$ is a transformation of f_s , as explained in Section 3.2.3. Consistently with Eq. (3.2), I initialize Lagrangian supersaturation PDF \mathcal{F}_s in Eq. (7.2) by sampling $\xi(t = 0)$ from a standardized Gaussian, conditional on

$$\xi(t = 0) > \mathbb{G}^{-1}(1 - \chi), \quad (7.3)$$

where $\mathbb{G}^{-1}(X)$ is the inverse CDF of a standardized Gaussian, and χ is the initial volume fraction of cloudy air. This initialization is a direct translation

of the initialization of droplets in Kumar *et al.* [2012], because Kumar *et al.* [2012] initialize droplets uniformly over the interval $-\frac{\chi}{2}L < x < \frac{\chi}{2}L$. The initial volume fraction χ for the statistical-model simulations in Section 3.2.5 is extracted from Kumar *et al.* [2012], $\chi = 0.4$.

A.2 Implementation of spectral relaxation model

The above mentioned feed-forward cascade of supersaturation variance described by the spectral relaxation model reads:

$$\frac{d\langle s'(t)^2 \rangle_m}{dt} = -\frac{C_\phi}{t_m} \langle s'(t)^2 \rangle_m \quad \text{for } m = 1, \text{ and} \quad (7.4)$$

$$\frac{d\langle s'(t)^2 \rangle_m}{dt} = C_\phi \frac{\langle s'(t)^2 \rangle_{m-1}}{t_{m-1}} - C_\phi \frac{\langle s'(t)^2 \rangle_m}{t_m} \quad \text{for } m > 1, \quad (7.5)$$

The number M of wave-number shells $m = 1, \dots, M$ with variances $\langle s'(t)^2 \rangle_m$ is computed from the Schmidt number $Sc = \kappa/\nu$ and the Reynolds number $Re_1 = TKE/\sqrt{\nu\epsilon}$, as explained by Fox [1995]. Extracting $Sc = 0.6818$ and $Re_1 = 22.22$ from Kumar *et al.* [2012], one finds $M = 5$. Following Fox [1995], I find the time constants t_m and the partition $0 = k_0 < k_1 < \dots < k_5$ of wave-number shells corresponding to the DNS of Kumar *et al.* [2012]. The time constants are listed in Table 7.1.

The initial supersaturation dissipation rate $\epsilon_s(t=0) = 1.277 \times 10^{-2} \tau_L^{-1}$ and the initial supersaturation variance $\sigma_s^2(t=0) = 2.258 \times 10^{-1}$ are computed from the initial supersaturation profile of Kumar *et al.* [2012]. Following Fox [1995], I set the modeling constants in Eq. (3.7) to $C_\omega = 0.54$ and $C_\chi = 3$. Fox [1995] prescribes $C_\phi = 2$, but reported values of C_ϕ typically range between 1.5 and 2.5 [Pope, 2000]. For meaningful comparison between statistical-model results and DNS, C_ϕ can not be too crudely approximated. When comparing to DNS of Kumar *et al.* [2014, 2012], I therefore estimate $C_\phi = 2.5$ from the top right panel of Fig. 4 of Kumar *et al.* [2012].

The spectral relaxation model describes statistically homogeneous turbulent mixing, but the DNS of Kumar *et al.* [2012] are statistically one-dimensional. One consequence is that, for the partition $0 = k_0 < k_1 < \dots < k_5$ of wave-number shells corresponding to the time constants in Table 7.1, all initial variance ends up within the first wave-number shell, $m = 1$. This causes $\epsilon_s(t)$ to make a peculiar dip during a minute first fraction of a simulation. This dip lacks

physical explanation, and most likely reflects that the spectral relaxation model is used beyond its indented scope. I therefore avoid the dip by initializing a small amount of variance within wave-number shells $m > 1$. These initial variances are such that they sustain a constant value of $\varepsilon_s(t)$ over the time interval of the non-physical dip. The initial shell variances $\langle s'(t)^2 \rangle_m$ are listed in Table 7.1.

Table 7.1: Time constants t_m and initial shell variances $\langle s'(t=0)^2 \rangle_m$ used in the implementation of the spectral relaxation model for the statistical-model simulations in Section 3.2.5.

m	1	2	3	4	5
t_m/τ_L	1	9.489×10^{-1}	3.163×10^{-1}	1.054×10^{-1}	5.272×10^{-2}
$\langle s'(0)^2 \rangle_m$	2.163×10^{-1}	6.067×10^{-3}	2.022×10^{-3}	6.741×10^{-4}	3.371×10^{-4}

B Derivation of Eq. (3.8)

Eq. (3.8) defines the function $\langle C_d(t) | s = S \rangle$, an approximation of the conditional average $\langle C_d(t) | s = S \rangle$. Here, I explain details in the derivation of this approximation, omitted in the main text. To derive $\langle C_d(t) | s = S \rangle$, I start by rewriting Eq. (1.12). Using Eq. (2.1), Eq. (1.12) can be written:

$$C_d(\mathbf{x}, t) = 4\pi A_3 \varrho_p \sum_{\alpha} G(|\mathbf{x} - \mathbf{x}_{\alpha}(t)|) r_{\alpha}(t) s(\mathbf{x}_{\alpha}(t), t). \quad (7.6)$$

This rewriting of Eq. (1.12) is well known, and used by Vaillancourt *et al.* [2001] and many others. I now impose that the width of the spatial kernel $G(|\mathbf{x} - \mathbf{x}_{\alpha}(t)|)$ is much smaller than the smallest length scale of the supersaturation field $s(\mathbf{x}, t)$. This constraint yields

$$C_d(\mathbf{x}, t) = 4\pi A_3 \varrho_p s(\mathbf{x}, t) \sum_{\alpha} G(|\mathbf{x} - \mathbf{x}_{\alpha}(t)|) r_{\alpha}(t), \quad (7.7)$$

because it implies that only droplets with supersaturations $s(\mathbf{x}_{\alpha}(t), t) = s(\mathbf{x}, t)$ contribute to the condensation rate at \mathbf{x} . Averaging Eq. (7.7) over the volume $V(t)_S^{S+\Delta S}$ of the space between the contours $s(\mathbf{x}, t) = S$ and $s(\mathbf{x}, t) = S + \Delta S$, one finds:

$$\overline{C}_d(t)_S^{S+\Delta S} = 4\pi A_3 \varrho_p \frac{N(t)_S^{S+\Delta S}}{V(t)_S^{S+\Delta S}} \overline{r}(t)_S^{S+\Delta S} S + \mathcal{O}(\Delta S). \quad (7.8)$$

Here, the number $N(t)_S^{S+\Delta S}$ and average radius $\bar{r}(t)_S^{S+\Delta S}$ of droplets within $V(t)_S^{S+\Delta S}$ are given by

$$N(t)_S^{S+\Delta S} = \sum_{\alpha=1}^{N_0} \psi_{\alpha}(t)_S^{S+\Delta S}, \quad (7.9)$$

and

$$\bar{r}(t)_S^{S+\Delta S} = \frac{1}{N(t)_S^{S+\Delta S}} \sum_{\alpha=1}^{N_0} r_{\alpha}(t) \psi_{\alpha}(t)_S^{S+\Delta S}, \quad (7.10)$$

where

$$\psi_{\alpha}(t)_S^{S+\Delta S} = \int_{V(t)_S^{S+\Delta S}} G(|\mathbf{x} - \mathbf{x}_{\alpha}(t)|) d\mathbf{x} \quad (7.11)$$

denotes the fraction of the effects on supersaturation that droplet α exerts within $V(t)_S^{S+\Delta S}$. Having formulated $\bar{C}_d(t)_S^{S+\Delta S}$ in term of $N(t)_S^{S+\Delta S}$ and $\bar{r}(t)_S^{S+\Delta S}$, I take the limit $\Delta S \rightarrow 0$ and arrive at Eq. (3.9).

To arrive at $\langle C_d(t) | s = S \rangle$, it remains to prove Eq. (3.12). I start by deriving

$$\langle V(t)_S^{S+\Delta S} \rangle = V f_s(S; t) \Delta S + \mathcal{O}(\Delta S^2). \quad (7.12)$$

To derive Eq. (7.12), I define the volume fraction $\chi(t)_S^{S+\Delta S}$ of the domain with supersaturation in the interval $S < s(\mathbf{x}, t) < S + \Delta S$. This volume fraction is a random variable, and I introduce its PDF

$$f_{\chi}(\Phi_S^{S+\Delta S}; t) = \frac{\partial}{\partial \chi(t)_S^{S+\Delta S}} F_{\chi}(\Phi_S^{S+\Delta S}; t), \quad (7.13)$$

where

$$F_{\chi}(\Phi_S^{S+\Delta S}; t) = \text{Prob} \{ \chi(t)_S^{S+\Delta S} < \Phi_S^{S+\Delta S} \} \quad (7.14)$$

is the CDF of $\chi(t)_S^{S+\Delta S}$. Furthermore, I introduce

$$F_{s|\chi}(\bar{S}; t | \Phi_S^{S+\Delta S}) = \text{Prob} \{ s(\mathbf{x}, t) < \bar{S} \} \text{ given } \{ \chi(t)_S^{S+\Delta S} = \Phi_S^{S+\Delta S} \} \quad (7.15)$$

to denote the CDF $F_{s|\chi}(\bar{S}; t|\Phi_S^{S+\Delta S})$ of supersaturation conditioned on volume fraction. For a given volume fraction $\chi(t)_S^{S+\Delta S} = \Phi_S^{S+\Delta S}$, the probability of supersaturation to be within the interval $S < s(\mathbf{x}, t) < S + \Delta S$ equals $\Phi_S^{S+\Delta S}$,

$$\begin{aligned}\Phi_S^{S+\Delta S} &= F_{s|\chi}(S + \Delta S; t|\Phi_S^{S+\Delta S}) - F_{s|\chi}(S; t|\Phi_S^{S+\Delta S}) \\ &= f_{s|\chi}(S; t|\Phi_S^{S+\Delta S})\Delta S + \mathcal{O}(\Delta S^2),\end{aligned}\quad (7.16)$$

where

$$f_{s|\chi}(\bar{S}; t|\Phi_S^{S+\Delta S}) = \frac{\partial}{\partial \bar{S}} F_{s|\chi}(\bar{S}; t|\Phi_S^{S+\Delta S}) \quad (7.17)$$

is the PDF of supersaturation conditioned on volume fraction. The average volume fraction $\langle \chi(t)_S^{S+\Delta S} \rangle$ of the domain with supersaturation in the interval $S < s(\mathbf{x}, t) < S + \Delta S$ is given by:

$$\langle \chi(t)_S^{S+\Delta S} \rangle = \int \Phi_S^{S+\Delta S} f_\chi(\Phi_S^{S+\Delta S}; t) d\Phi_S^{S+\Delta S} \quad (7.18)$$

$$= \Delta S \int f_{s|\chi}(S; t|\Phi_S^{S+\Delta S}) f_\chi(\Phi_S^{S+\Delta S}; t) d\Phi_S^{S+\Delta S} + \mathcal{O}(\Delta S^2) \quad (7.19)$$

$$= f_s(S; t)\Delta S + \mathcal{O}(\Delta S^2). \quad (7.20)$$

Here, the first step is to define $\langle \chi(t)_S^{S+\Delta S} \rangle$. The second step is to insert the expression for $\Phi_S^{S+\Delta S}$ in Eq. (7.16). The third step is to obtain $f_s(S; t)$ as a marginal PDF of $f_{s|\chi}(S; t|\Phi_S^{S+\Delta S})f_\chi(\Phi_S^{S+\Delta S}; t)$, which is the joint PDF of $s(\mathbf{x}, t)$ and $\chi(t)_S^{S+\Delta S}$. Multiplying Eq. (7.18) by the domain volume V , one obtains Eq. (7.12).

An analogous derivation leads to the relation

$$\langle N(t)_S^{S+\Delta S} \rangle = N_0 \mathcal{F}_s(S; t)\Delta S + \mathcal{O}(\Delta S^2). \quad (7.21)$$

In the analogous derivation, one starts by defining the fraction $q(t)_S^{S+\Delta S}$ of droplets with supersaturations $s(\mathbf{x}_\alpha(t), t)$ in the interval $S < s(\mathbf{x}_\alpha(t), t) < S + \Delta S$. One then introduces the PDF of $q(t)_S^{S+\Delta S}$, in analogy with Eq. (7.13). After that, one defines the conditional CDF

$$F_{s|q}(\bar{S}; t|Q_S^{S+\Delta S}) = \text{Prob} \{s(\mathbf{x}_\alpha(t), t) < \bar{S}\} \text{ given } \{q(t)_S^{S+\Delta S} = Q_S^{S+\Delta S}\}, \quad (7.22)$$

of droplet supersaturation conditioned on droplet fraction, in analogy with Eq. (7.15). One proceeds by considering a given droplet fraction $q(t)_S^{S+\Delta S} = Q_S^{S+\Delta S}$. Up to first order in ΔS , this fraction can be expressed as a product of ΔS and the PDF that corresponds to $F_{s|q}(\bar{S}; t|Q_S^{S+\Delta S})$, in analogy with Eq. (7.16). Performing the steps in Eq. (7.18), one finds the expected fraction of droplets with supersaturation supersaturations $s(\mathbf{x}_\alpha(t), t)$ in the interval $S < s(\mathbf{x}_\alpha(t), t) < S + \Delta S$,

$$\langle q(t)_S^{S+\Delta S} \rangle = \mathcal{F}_s(S; t) \Delta S + \mathcal{O}(\Delta S^2), \quad (7.23)$$

which multiplied by N_0 gives Eq. (7.21). Dividing Eq. (7.21) by Eq. (7.12), one obtains Eq. (3.12).

C Particles with non-zero Γ and Ψ

It was explained in Section 4.2 that the angular dynamics of a rotation-symmetric particle that possesses a mirror plane that is orthogonal to the axis of rotation symmetry is governed by three shape parameters in Stokes flow: Λ , Γ , and Ψ . Exact values of these shape parameters can be computed for a particle that is constructed from a set of spheroids connected by infinitely thin rigid rods. It is clear that such particles are artificial, and do not exist in reality. Particles consisting of many spheroids can however be continuously deformed into more realistic particle shapes, and one may therefore expect that a particle constructed from spheroids can give an intuitive understanding for the physical meaning of the shape parameters of realistic particles. Multi-spheroid models for particles in Stokes flow were used already by Bretherton [1962].

In this Appendix I construct a particle that consists of four spheroids and has $\Gamma \neq 0$ and $\Psi = 0$, and another particle that consists of eight spheroids and has $\Gamma \neq 0$ and $\Psi \neq 0$. I then argue for why the parameters Γ and Ψ are non-zero by analyzing the torque that the flow exerts upon the particles when they are placed in a simple shear flow. The particles that I construct have a rotation symmetry and a reflection symmetry in a plane that is orthogonal to the axis of rotation symmetry, so Paper B tells us that their angular dynamics are completely determined by Λ , Γ and Ψ . Before I construct the particles in Sections C.2 and C.3, I start by explaining how the shape parameters of a multi-spheroid particle can be computed in Section C.1.

C.1 Shape parameters of multi-spheroid particles

In Paper B, we express the shape parameters in terms of elements of the resistance tensors \mathcal{C} and \mathcal{H} in the particle fixed basis $[\mathbf{q}, \mathbf{p}, \mathbf{n}]$, where \mathbf{n} points along the symmetry axis of the particle. For particles with the symmetries under consideration, it is found that:

$$\Lambda = -2 \frac{\mathcal{H}_{123}}{\mathcal{C}_{11}}, \quad \Psi = 2 \frac{\mathcal{H}_{113}}{\mathcal{C}_{11}}, \quad \text{and} \quad \Gamma = \frac{\mathcal{H}_{333} - \mathcal{H}_{311}}{\mathcal{C}_{33}} - \Psi. \quad (7.24)$$

Here, it is assumed that \mathcal{H} is symmetric in its last two indices, $\mathcal{H}_{ijk} = \mathcal{H}_{ikj}$. This assumption causes no complications, because \mathcal{H} occurs only multiplied with the strain rate \mathbb{S} in Eq. (4.6), which is symmetric. Eqs. (7.24) make it possible to find the shape parameters Λ , Γ and Ψ for a particle by computing the tensor elements \mathcal{H}_{123} , \mathcal{H}_{113} , \mathcal{H}_{333} , \mathcal{H}_{311} , \mathcal{C}_{11} , and \mathcal{C}_{33} in the particle-fixed basis.

The tensor elements can be computed for a particle by analyzing its hydrodynamic torque in different flows, using Eq. (4.6). For example one finds

$$\mathcal{C}_{11} = \frac{\tau_1}{\mu} \quad (7.25)$$

by placing the particle at rest in the purely rotating ambient flow with $\Omega_i = \delta_{i1}$, $u_i^{(\infty)} = 0$, and $S_{ij} = 0$. In the same way one finds \mathcal{C}_{33} from τ_3 in a purely rotating flow with $\Omega_i = \delta_{i3}$. Similarly, one finds the tensor elements \mathcal{H}_{123} , \mathcal{H}_{113} , \mathcal{H}_{333} , and \mathcal{H}_{311} by putting the particle at rest in different straining flows. If the rate of strain S_{ij} is symmetric and traceless it is guaranteed that it represents a Stokes flow in which the torque is given by $\tau_i = \mu \mathcal{H}_{ijk} S_{jk}$.

The distances between the spheroids of the multi-spheroid particles that I construct below are much larger than the spheroids that they consist of. This ensures that there are no interactions between the spheroids, and that the torque upon the multi-spheroid particles does not depend on the torque that each spheroid experiences around its center due to flow gradients [Kim & Karrila, 1991]. That the rods that connect the spheroids are infinitely thin implies that they do not contribute to the torque upon the particle. The particle torque $\boldsymbol{\tau}$ is therefore the summed torque contributions of all spheroids:

$$\boldsymbol{\tau} = \sum_{s=1}^N \mathbf{r}^{(s)} \times \mathbf{F}^{(s)}. \quad (7.26)$$

Here, I introduced N to denote the number spheroids, and labeled each spheroid by an index $s = 1, \dots, N$. Furthermore, $\mathbf{F}^{(s)}$ is the force upon spheroid s , and $\mathbf{r}^{(s)}$ is its position.

The flow velocity $\mathbf{u}^{(s)}$ at spheroid s in a purely rotating or straining flow is given by

$$\mathbf{u}^{(s)} = \boldsymbol{\Omega} \times \mathbf{r}^{(s)} + \mathbb{S} \mathbf{r}^{(s)}, \quad (7.27)$$

where $\boldsymbol{\Omega}$ and \mathbb{S} are the flow rotation and strain. The force $\mathbf{F}^{(s)}$ upon spheroid s depends upon the flow velocity at the spheroids position, and upon the spheroids orientation. The orientation dependence is given by the spheroids force-velocity resistance tensor $\mathcal{A}^{(s)}$. If the particle is at rest, one finds

$$\mathbf{F}^{(s)} = \mu \mathcal{A}^{(s)} \mathbf{u}^{(s)}. \quad (7.28)$$

The particles that I construct consist of identical spheroids. The resistance tensor $\mathcal{A}^{(s)}$ for spheroid s can be written

$$\mathcal{A}^{(s)} = X^A \mathbf{t}^{(s)} \mathbf{t}^{(s)\top} + Y^A (\mathbb{1} - \mathbf{t}^{(s)} \mathbf{t}^{(s)\top}), \quad (7.29)$$

where $\mathbf{t}^{(s)}$ is a unit vector pointing along the symmetry axis of spheroid s , and X^A and Y^A are resistance functions that depend on the size and aspect ratio of the spheroid [Kim & Karrila, 1991].

In summary, one can find the shape parameters of the multi-spheroid particles that I construct below from the resistance-tensor elements in Eqs. (7.24). These tensor elements are given by the torque upon the particle in different flows, as in Eq. (7.25). The torque is given by Eqs. (7.26), (7.27), (7.28), and (7.29).

C.2 A particle with $\Gamma \neq 0$ and $\Psi = 0$

The particle in Fig. (7.1) is similar to the particle in Fig. 5 of Paper B, and looks like a water wheel. It however consists of four spheroids ($N = 4$), as opposed particle in Fig. 5 of Paper B, which consists of three. The four-spheroid setup facilitates the intuitive understanding of the parameter Γ that I argue for below. The spheroids are located in the (\mathbf{q}, \mathbf{p}) -plane, at a distance ξ from the origin. Their symmetry axes are contained in the (\mathbf{q}, \mathbf{p}) -plane, but are rotated by an angle φ_1 , in order to ensure that the particle does not possess

a reflection symmetry in a plane that contains the axis of rotation symmetry. The angle φ_1 is defined in Fig. (7.1a).

For the particle in Fig. (7.1) one finds

$$C_{11} = 2\xi^2 Y^A \quad , \quad C_{33} = 4\xi^2 [Y^A + (X^A - Y^A)\sin^2 \varphi_1], \quad (7.30)$$

$$H_{123} = \xi^2 Y^A \quad , \quad H_{113} = 0 \quad , \quad \text{and} \quad (7.31)$$

$$H_{333} - H_{311} = (Y^A - X^A)\xi^2 \sin 2\varphi_1, \quad (7.32)$$

using the procedures outlined above. Eqs. (7.24) give:

$$\Lambda = -1 \quad , \quad \Psi = 0 \quad , \quad \text{and} \quad \Gamma = \frac{1}{4} \sin 2\varphi_1 \left[\frac{1}{1 - X^A/Y^A} - \sin^2 \varphi_1 \right]^{-1}. \quad (7.33)$$

Consistently with that Γ relies on that the particles does not possess a reflection symmetry in a plane that contains the axis of rotation symmetry, the parameter vanishes for $\varphi_1 = 0$, $\varphi_1 = \pi/2$, and $X^A = Y^A$. The particle has $\Lambda = -1$, which corresponds to a spheroid with zero aspect ratio. This is a consequence of that the particle is infinitely flat, since all spheroids are much smaller than the particle size, and since the spheroids reside in the same plane.

The magnitude of the shape parameter Γ can not exceed $1/(4\sqrt{2}) = 0.18$ for this particle. This can be understood by analyzing the expression for Γ in Eqs. (7.33), and taking into account that the ratio X^A/Y^A ranges from $1/2$ for infinitely thin discs, to 2 for infinitely thin rods Kim & Karrila [1991]. The largest magnitudes $|\Gamma|$ are obtained if the particle is constructed from infinitely thin discs. At the angles $\varphi_1 = \pm \arctan(\sqrt{2}) = 55^\circ$, one obtains $\Gamma = \pm 1/(4\sqrt{2})$ by inserting $X^A/Y^A = 1/2$ into the expression for Γ in Eqs. (7.33).

Placed in the simple shear flow defined in Section 4.1.1, the effect of Γ on the particle spin is described by Eq. (4.20c). The effect is maximal at the angles $\phi = \pi/4$ and $\theta = \pi/2$. In this orientation the particle is oriented with its symmetry axis in the flow-shear plane, so that it makes a 45° angle with the flow direction. In this orientation, the particle has a non-zero spin only if $\Gamma \neq 0$. Figs. 7.1b and 7.1c show a $\Gamma \neq 0$ -particle in this orientation, viewed from different angles. It can be seen that the particle orientation ensures that the flow hits the different sides of the particle in opposite directions. The x -velocity is positive for the spheroid above the flow-vorticity plane, but negative for the spheroid below this plane. If the particle is at rest, spheroids

1 and 3 give a non-zero torque along the symmetry axis of the particle. In the overdamped limit, the particle moves so that the torque upon it vanishes at every instant. It must therefore make a spinning motion parameterized by Γ to compensate for this torque.

C.3 A particle with $\Gamma \neq 0$ and $\Psi \neq 0$

This particle resembles two propellers of opposite chirality that are fixed to the same axis of rotation symmetry. The spheroids reside in two layers that are mirror images of each other, reflected in a plane that is orthogonal to the axis of rotation symmetry. The layers are separated by a distance ζ , and contain four spheroids each. The particle is constructed as follows:

1. Place the first spheroid at $\mathbf{r}^{(1)} = \xi \mathbf{q} + (\zeta/2)\mathbf{n}$. Orient the spheroid so that its symmetry axis resides in the (\mathbf{p}, \mathbf{n}) -plane, and forms the angle φ_2 with the \mathbf{p} -direction; $\mathbf{t}^{(1)} = \cos \varphi_2 \mathbf{p} + \sin \varphi_2 \mathbf{n}$.
2. Construct the top layer of the particle by adding spheroids 2, 3 and 4 as rotations of spheroid 1 by the angles $\pi/2$, π , and $3\pi/4$ around the \mathbf{n} -axis. The position and orientation of spheroid s ($2 \leq s \leq 4$) is then given by $\mathbf{r}^{(s)} = \mathbb{R}_{\mathbf{n}}^{\pi/2} \mathbf{r}^{(s-1)}$ and $\mathbf{t}^{(s)} = \mathbb{R}_{\mathbf{n}}^{\pi/2} \mathbf{t}^{(s-1)}$, where $\mathbb{R}_{\mathbf{n}}^{\pi/2}$ denotes a $\pi/2$ rotation around the \mathbf{n} -axis.
3. Construct the bottom layer of the particle by adding spheroids 5, 6, 7, and 8 as reflections of spheroids 1, 2, 3, and 4 in the (\mathbf{p}, \mathbf{n}) -plane. The position and orientation of spheroid s ($5 \leq s \leq 8$) is then given by $\mathbf{r}^{(s)} = \mathbf{r}^{(s-4)} - \zeta \mathbf{n}$ and $\mathbf{t}^{(s)} = \mathbf{t}^{(s-4)} - 2(\mathbf{n} \cdot \mathbf{t}^{(s-4)})\mathbf{n}$.

Figs. 7.2a and 7.2b show a particle of this type, viewed from two different angles. Following the procedure described in Section C.1, one finds

$$C_{11} = 2Y^A(\zeta^2 + 2\xi^2) + (X^A - Y^A)\zeta^2 \cos^2 \varphi_2 + 4(X^A - Y^A)\sin^2 \varphi_2, \quad (7.34)$$

$$C_{33} = 8\xi^2 [Y^A + (X^A - Y^A)\cos^2 \varphi_2], \quad (7.35)$$

$$H_{123} = -Y^A(\zeta^2 - 2\xi^2) - \frac{1}{2}(X^A - Y^A)\zeta^2 \cos^2 \varphi_2 + 2(X^A - Y^A)\xi^2 \sin^2 \varphi_2, \quad (7.36)$$

$$H_{113} = -(X^A - Y^A)\zeta \xi \sin 2\varphi_2, \quad \text{and} \quad H_{333} - H_{311} = -2H_{113}, \quad (7.37)$$

and

$$\Lambda = \frac{\lambda^2 - 1 + \frac{1}{4}(1 - X^A/Y^A)[2 - \lambda^2 - (\lambda^2 + 2)\cos 2\varphi_2]}{\lambda^2 + 1 - \frac{1}{4}(1 - X^A/Y^A)[2 + \lambda^2 + (\lambda^2 - 2)\cos 2\varphi_2]}, \quad (7.38)$$

$$\Psi = \frac{\frac{1}{\sqrt{2}}(1 - X^A/Y^A)\lambda \sin 2\varphi_2}{\lambda^2 + 1 - \frac{1}{4}(1 - X^A/Y^A)[2 + \lambda^2 + (\lambda^2 - 2)\cos 2\varphi_2]}, \text{ and} \quad (7.39)$$

$$\Gamma = - \left[\frac{1/2}{\lambda^2 + 1 - \frac{1}{4}(1 - X^A/Y^A)[2 + \lambda^2 + (\lambda^2 - 2)\cos 2\varphi_2]} + \frac{1/4}{1 - (1 - X^A/Y^A)\cos^2 \varphi_2} \right] \sqrt{2}(1 - X^A/Y^A)\lambda \sin 2\varphi_2, \quad (7.40)$$

where $\lambda = \zeta/(\sqrt{2}\xi)$. The parameter Ψ vanishes for $\varphi_2 = 0$, $\varphi_2 = \pi/2$, and $X^A = Y^A$, because the particle then possesses a mirror plane that contains the axis of rotation symmetry. The particle is not flat, as opposed to the particle constructed in the previous section, and the shape parameter Λ corresponds to the shape parameter of a spheroid with finite aspect ratio.

The magnitude of the shape parameter Ψ can not exceed $\frac{2}{5}\sqrt{103\sqrt{6}-252}/\sin[2\arccos(\sqrt{\sqrt{6}-2})] = 0.22$ for the particle in Fig. 7.2. This constraint follows from that $1/2 \leq X^A/Y^A \leq 2$, just as the constraint on $|\Gamma|$ that I concluded in the previous section, for the particle in Fig. 7.1. Analyzing Eq. (7.39), one finds that $|\Psi|$ is maximized at $\lambda = (2/3)^{1/4} = 0.90$, $X^A/Y^A = 1/2$, and $\varphi_2 = \pm \arccos(\sqrt{\sqrt{6}-2}) = 48^\circ$. A particle that maximizes $|\Psi|$ consists of infinitely thin discs, since $X^A/Y^A = 1/2$ at the maxima.

As in the previous section, we place the particle in the simple shear flow defined in Section 4.1.1, and analyze the effect of Ψ using Eq. (4.20). The shape parameter has a distinct effect on the tumbling when $\theta = 3\pi/2$, so that the particle is oriented with its symmetry axis in flow-shear direction. It is only for a non-zero value of Ψ that particle tumbles with a non-zero value of $\dot{\theta}$. This means that the symmetry axis of a particle with a non-zero value of Ψ can cross the flow-shear plane, as opposed to the symmetry axis of a particle that moves of a Jeffery orbit. The magnitude of this effect peaks at $\phi = 0$ and $\theta = 3\pi/2$. In this orientation the particle aligns its symmetry axis with the shear direction. Figs. 7.2c and 7.2d show the non-zero- Ψ particle at rest in this orientation, view from different angles. It can be seen that the two layers of the particle face opposing flow, and that the chirality of the propeller-like layers ensures that two opposing sides of the particle are dragged in opposite

direction around the flow direction. As a consequence, the particle has a non-zero torque component in the flow direction. To compensate for this torque in the overdamped limit, the symmetry axis must perform a tumbling motion across the flow shear plane that is parameterized by Ψ .

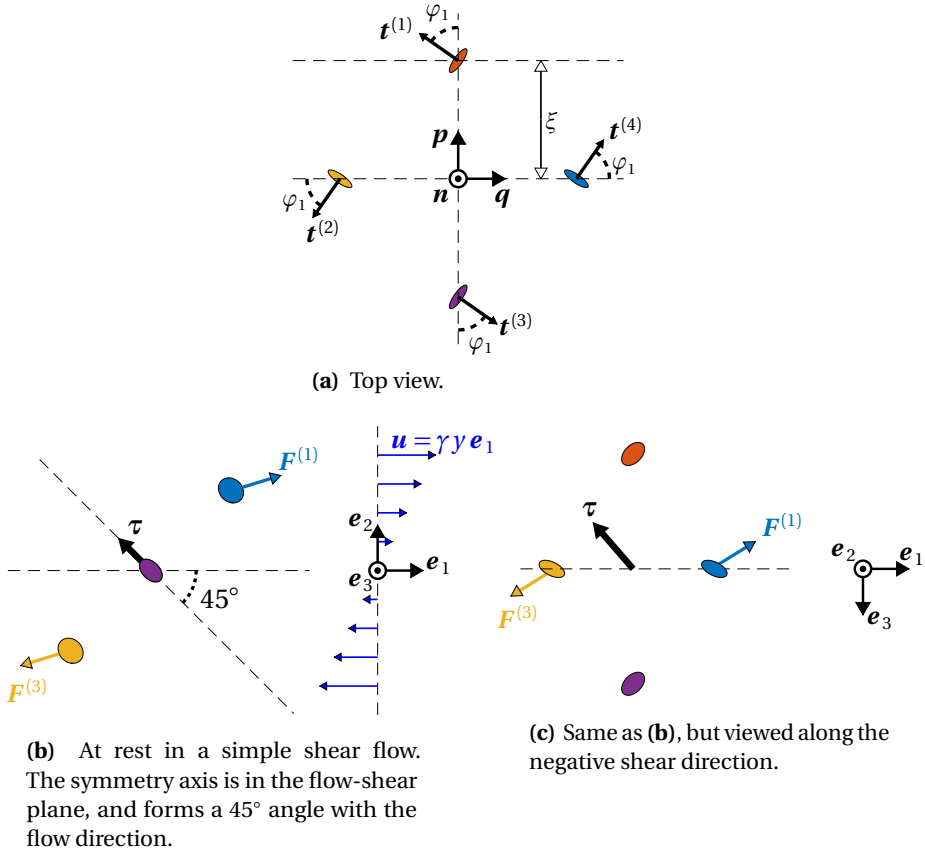


Figure 7.1: Particle with a non-zero shape parameter Γ . The particle consists of four spheroids, and resembles a water wheel. The shape parameter Γ is a function of ξ , and the angle φ_1 that determines the orientations of the spheroids (see text). **(a)** Top view. The spheroids form a square, and each spheroid is at the distance ξ from the symmetry axis of the particle. The symmetry axis of each spheroid reside in the plane of this square, and forms the angle φ_1 with the spheroids position vector. **(b)** The non-zero Γ reflects that the torque τ has a non-zero component along the symmetry axis of the particle when the particle is placed at rest in a simple shear flow with its symmetry axis in the flow-shear plane. The effect of Γ is largest when symmetry axis resides in this plane and is at a 45° angle with the flow direction. **(c)** Same as **(b)**, but viewed along the negative shear direction. The non-zero torque component in **(b)** follows from that the drag force on spheroids 1 and 3 have opposing components in the vorticity direction. This is a consequence of the orientations of the spheroids, and of that the spheroids face opposing flow.

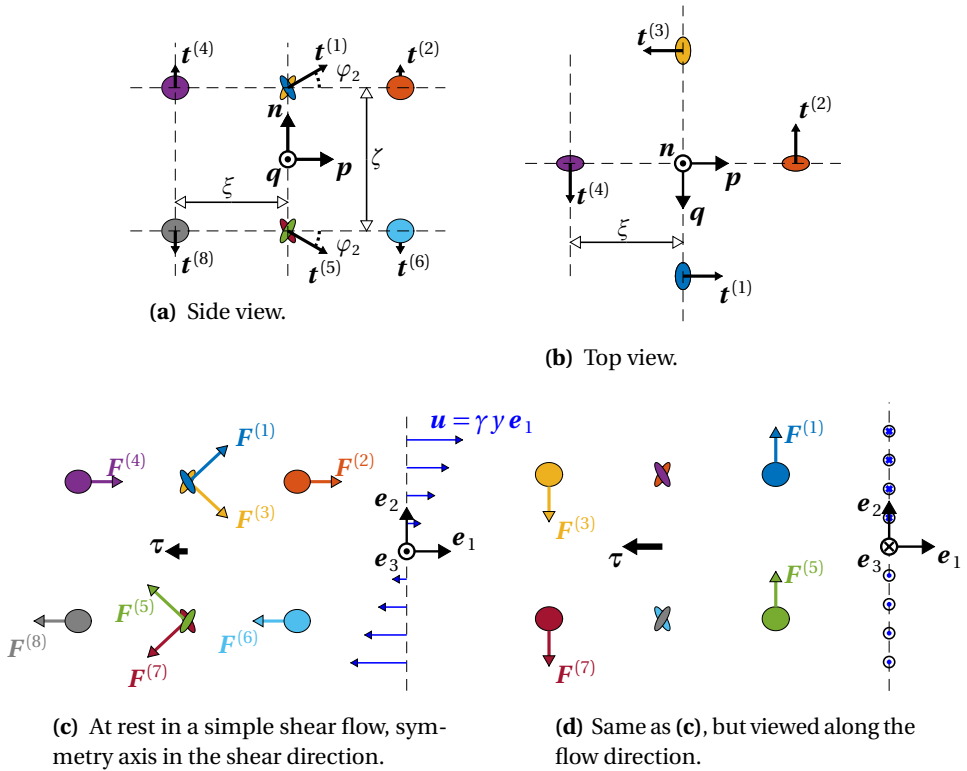


Figure 7.2: Particle with a non-zero shape parameter Ψ . The particle consists of eight spheroids that reside in two layers that are mirror images of each other. The shape parameter Ψ is a function of the lengths ξ and ζ that determine the positions of the spheroids, and the angle φ_2 that determines their orientations (see text). **(a)** Side view. The top and bottom layers are mirror images of each other. The distance between the two layers is ζ , and the angle φ_2 ensures that the particle does not possess a reflection symmetry in a plane that contains its axis of rotation symmetry. Each spheroid is located at a distance ξ from the symmetry axis. **(b)** Top view. The spheroids in each layer form a square, and each spheroid is a $\pi/2$ -rotation of a neighboring spheroid in the same layer. **(c)** The non-zero Ψ reflects that the torque τ has a non-zero component in the flow direction when the particle is placed at rest in a simple shear flow with its symmetry axis in the shear direction. **(d)** Same as (c), but viewed along the flow direction. The non-zero torque component in (c) follows from that one side of the particle is dragged in the shear direction, while the opposing side is dragged against the shear direction.

References

- WALLACE, J. M & HOBBS, P. V 2006 *Atmospheric Science: An Introductory Survey*. Elsevier.
- LAMB, D & VERLINDE, J 2011 *Physics and Chemistry of Clouds*. Cambridge University Press.
- DEGIRMENDŽIĆ, J & WIBIG, J 2007 Jet stream patterns over Europe in the period 1950–2001 – classification and basic statistical properties. *Theoretical and Applied Climatology* **88** (3-4), 149–167.
- DEVENISH, B, BARTELLO, P, BRENGUIER, J.-L, COLLINS, L, GRABOWSKI, W. W, IJZERMANS, R, MALINOWSKI, S. P, REEKS, M, VASSILICOS, J, WANG, L.-P & WARHAFT, Z 2012 Droplet growth in warm turbulent clouds. *Quarterly Journal of the Royal Meteorological Society* **138** (667), 1401–1429.
- SCHWARTZ, S. E 2008 Uncertainty in climate sensitivity: Causes, consequences, challenges. *Energy & Environmental Science* **1** (4), 430–453.
- BELLOUIN, N, QUAAS, J, GRYSPEERDT, E, KINNE, S, STIER, P, WATSON-PARRIS, D, BOUCHER, O, CARSLAW, K. S, CHRISTENSEN, M, DANIAU, A.-L *et al.* 2020 Bounding global aerosol radiative forcing of climate change. *Reviews of Geophysics* **58** (1), e2019RG000660.
- SZUMOWSKI, M. J, RAUBER, R. M, OCHS III, H. T & MILLER, L 1997 The microphysical structure and evolution of Hawaiian rainband clouds. Part I: Radar observations of rainbands containing high reflectivity cores. *Journal of the Atmospheric Sciences* **54** (3), 369–385.
- SZUMOWSKI, M. J, RAUBER, R. M, OCHS III, H. T & BEARD, K. V 1998 The microphysical structure and evolution of Hawaiian rainband clouds. Part II: Aircraft measurements within rainbands containing high reflectivity cores. *Journal of the Atmospheric Sciences* **55** (2), 208–226.
- GRABOWSKI, W. W & WANG, L.-P 2013 Growth of cloud droplets in a turbulent environment. *Annual Review of Fluid Mechanics* **45**, 293–324.
- YAU, M. K & ROGERS, R. R 1989 *A Short Course in Cloud Physics*. Butterworth Heinemann.

- LASHER-TRAPP, S. G, COOPER, W. A & BLYTH, A. M 2005 Broadening of droplet size distributions from entrainment and mixing in a cumulus cloud. *Quarterly Journal of the Royal Meteorological Society* **131** (605), 195–220.
- COOPER, W. A 1989 Effects of variable droplet growth histories on droplet size distributions. Part I: Theory. *Journal of the Atmospheric Sciences* **46** (10), 1301–1311.
- GRABOWSKI, W. W 2006 Indirect impact of atmospheric aerosols in idealized simulations of convective–radiative quasi equilibrium. *Journal of Climate* **19** (18), 4664–4682.
- JEFFERY, C. A 2007 Inhomogeneous cloud evaporation, invariance, and Damköhler number. *Journal of Geophysical Research: Atmospheres* **112** (D24).
- BAKER, M, CORBIN, R & LATHAM, J 1980 The influence of entrainment on the evolution of cloud droplet spectra: I. a model of inhomogeneous mixing. *Quarterly Journal of the Royal Meteorological Society* **106** (449), 581–598.
- NGUYEN, H, KARP-BOSS, L, JUMARS, P. A & FAUCI, L 2011 Hydrodynamic effects of spines: A different spin. *Limnology and Oceanography: Fluids and Environments* **1** (1), 110–119.
- JUCHA, J, NASO, A, LÉVÊQUE, E & PUMIR, A 2018 Settling and collision between small ice crystals in turbulent flows. *Physical Review Fluids* **3** (1), 014604.
- GUSTAVSSON, K, SHEIKH, M, LOPEZ, D, NASO, A, PUMIR, A & MEHLIG, B 2019 Effect of fluid inertia on the orientation of a small prolate spheroid settling in turbulence. *New Journal of Physics* **21** (8), 083008.
- GUSTAVSSON, K, SHEIKH, M, NASO, A, PUMIR, A & MEHLIG, B 2020 Effect of particle inertia on the alignment of small ice crystals in turbulent clouds. *arXiv preprint: 2007.11530* .
- ANAND, P, RAY, S. S & SUBRAMANIAN, G 2020 Orientation dynamics of sedimenting anisotropic particles in turbulence. *Physical Review Letters* **125** (3), 034501.
- LEAL, L & HINCH, E 1971 The effect of weak Brownian rotations on particles in shear flow. *Journal of Fluid Mechanics* **46** (4), 685–703.

- RALLISON, J 1978 The effects of Brownian rotations in a dilute suspension of rigid particles of arbitrary shape. *Journal of Fluid Mechanics* **84** (2), 237–263.
- ALMONDO, G, EINARSSON, J, ANGILELLA, J & MEHLIG, B 2018 Intrinsic viscosity of a suspension of weakly Brownian ellipsoids in shear. *Physical Review Fluids* **3** (6), 064307.
- KIM, S & KARRILA, S. J 1991 *Microhydrodynamics*. Butterworth-Heinemann.
- EINARSSON, J, ANGILELLA, J & MEHLIG, B 2014 Orientational dynamics of weakly inertial axisymmetric particles in steady viscous flows. *Physica D: Nonlinear Phenomena* **278**, 79–85.
- BRETHERTON, F. P 1962 The motion of rigid particles in a shear flow at low Reynolds number. *Journal of Fluid Mechanics* **14** (2), 284–304.
- KOLMOGOROV, A. N 1941 The local structure of turbulence in incompressible viscous fluid for very large reynolds numbers. *Cr Acad. Sci. URSS* **30**, 301–305.
- CHEN, X, ANEL, J. A, SU, Z, DE LA TORRE, L, KELDER, H, VAN PEET, J & MA, Y 2013 The deep atmospheric boundary layer and its significance to the stratosphere and troposphere exchange over the Tibetan Plateau. *PloS one* **8** (2), e56909.
- CAVCAR, M 2000 The international standard atmosphere (ISA). *Anadolu University, Turkey* **30** (9), 1–6.
- SRIVASTAVA, R 1989 Growth of cloud drops by condensation: A criticism of currently accepted theory and a new approach. *Journal of Atmospheric Sciences* **46** (7), 869–887.
- VAILLANCOURT, P, YAU, M & GRABOWSKI, W 2001 Microscopic approach to cloud droplet growth by condensation. Part I: Model description and results without turbulence. *Journal of the Atmospheric Sciences* **58** (14), 1945–1964.
- ANDREJCZUK, M, GRABOWSKI, W. W, MALINOWSKI, S. P & SMOLARKIEWICZ, P. K 2006 Numerical simulation of cloud–clear air interfacial mixing: Effects

- on cloud microphysics. *Journal of the Atmospheric Sciences* **63** (12), 3204–3225.
- PINSKY, M, KHAIN, A & KOROLEV, A 2016a Theoretical analysis of mixing in liquid clouds – Part 3: Inhomogeneous mixing. *Atmospheric Chemistry and Physics* **16** (14).
- KUMAR, B, SCHUMACHER, J & SHAW, R. A 2014 Lagrangian mixing dynamics at the cloudy–clear air interface. *Journal of the Atmospheric Sciences* **71** (7), 2564–2580.
- PERRIN, V. E & JONKER, H. J 2015 Lagrangian droplet dynamics in the subsiding shell of a cloud using direct numerical simulations. *Journal of the Atmospheric Sciences* **72** (10), 4015–4028.
- SARDINA, G, PICANO, F, BRANDT, L & CABALLERO, R 2015 Continuous growth of droplet size variance due to condensation in turbulent clouds. *Physical Review Letters* **115**, 184501.
- BANNON, P. R 1996 On the anelastic approximation for a compressible atmosphere. *Journal of the Atmospheric Sciences* **53** (23), 3618–3628.
- VAILLANCOURT, P, YAU, M, BARTELLO, P & GRABOWSKI, W. W 2002 Microscopic approach to cloud droplet growth by condensation. Part II: Turbulence, clustering, and condensational growth. *Journal of the Atmospheric Sciences* **59** (24), 3421–3435.
- KUMAR, B, BERA, S, PRABHA, T. V & GRABOWSKI, W. W 2017 Cloud-edge mixing: Direct numerical simulation and observations in Indian Monsoon clouds. *Journal of Advances in Modeling Earth Systems* **9** (1), 332–353.
- KUMAR, B, GÖTZFRIED, P, SURESH, N, SCHUMACHER, J & SHAW, R. A 2018 Scale dependence of cloud microphysical response to turbulent entrainment and mixing. *Journal of Advances in Modeling Earth Systems* **10** (11), 2777–2785.
- BODENSCHATZ, E, MALINOWSKI, S. P, SHAW, R. A & STRATMANN, F 2010 Can we understand clouds without turbulence? *Science* **327** (5968), 970–971.

- ANDREJCZUK, M, GRABOWSKI, W. W, MALINOWSKI, S. P & SMOLARKIEWICZ, P. K 2004 Numerical simulation of cloud-clear air interfacial mixing. *Journal of the Atmospheric Sciences* **61** (14), 1726–1739.
- LEHMANN, K, SIEBERT, H & SHAW, R. A 2009 Homogeneous and inhomogeneous mixing in cumulus clouds: Dependence on local turbulence structure. *Journal of the Atmospheric Sciences* **66** (12), 3641–3659.
- POPE, S. B 2000 *Turbulent Flows*. Cambridge university press.
- ISHIHARA, T, GOTOH, T & KANEDA, Y 2009 Study of high-Reynolds number isotropic turbulence by direct numerical simulation. *Annual Review of Fluid Mechanics* **41**, 165–180.
- KOLMOGOROV, A. N 1962 A refinement of previous hypotheses concerning the local structure of turbulence in a viscous incompressible fluid at high Reynolds number. *Journal of Fluid Mechanics* **13** (1), 82–85.
- MARION, J. B 2013 *Classical dynamics of particles and systems*. Academic Press.
- SHAW, R. A 2003 Particle-turbulence interactions in atmospheric clouds. *Annual Review of Fluid Mechanics* **35** (1), 183–227.
- MELLADO, J. P 2017 Cloud-top entrainment in stratocumulus clouds. *Annual Review of Fluid Mechanics* **49**, 145–169.
- KERSTEIN, A. R 1988 A linear-eddy model of turbulent scalar transport and mixing. *Combustion Science and Technology* **60** (4-6), 391–421.
- KRUEGER, S. K 1993 Linear eddy modeling of entrainment and mixing in stratus clouds. *Journal of the Atmospheric Sciences* **50** (18), 3078–3090.
- SU, C.-W, KRUEGER, S. K, MCMURTRY, P. A & AUSTIN, P. H 1998 Linear eddy modeling of droplet spectral evolution during entrainment and mixing in cumulus clouds. *Atmospheric Research* **47**, 41–58.
- TÖLLE, M. H & KRUEGER, S. K 2014 Effects of entrainment and mixing on droplet size distributions in warm cumulus clouds. *Journal of Advances in Modeling Earth Systems* **6** (2), 281–299.

- HOFFMANN, F & FEINGOLD, G 2019 Entrainment and mixing in stratocumulus: Effects of a new explicit subgrid-scale scheme for large-eddy simulations with particle-based microphysics. *Journal of the Atmospheric Sciences* **76** (7), 1955–1973.
- SHIMA, S.-I, KUSANO, K, KAWANO, A, SUGIYAMA, T & KAWAHARA, S 2009 The super-droplet method for the numerical simulation of clouds and precipitation: A particle-based and probabilistic microphysics model coupled with a non-hydrostatic model. *Quarterly Journal of the Royal Meteorological Society* **135** (642), 1307–1320.
- PAOLI, R & SHARIFF, K 2009 Turbulent condensation of droplets: Direct simulation and a stochastic model. *Journal of the Atmospheric Sciences* **66** (3), 723–740.
- GRABOWSKI, W. W, MORRISON, H, SHIMA, S.-I, ABADE, G. C, DZIEKAN, P & PAWLOWSKA, H 2019 Modeling of cloud microphysics: Can we do better? *Bulletin of the American Meteorological Society* **100** (4), 655–672.
- JENNY, P, ROEKAERTS, D & BEISHUIZEN, N 2012 Modeling of turbulent dilute spray combustion. *Progress in Energy and Combustion Science* **38** (6), 846–887.
- JEFFERY, C. A & REISNER, J. M 2006 A study of cloud mixing and evolution using PDF methods. Part I: Cloud front propagation and evaporation. *Journal of the Atmospheric Sciences* **63** (11), 2848–2864.
- CHANDRAKAR, K. K, CANTRELL, W, CHANG, K, CIOCHETTO, D, NIEDERMEIER, D, OVCHINNIKOV, M, SHAW, R. A & YANG, F 2016 Aerosol indirect effect from turbulence-induced broadening of cloud-droplet size distributions. *Proceedings of the National Academy of Sciences* **113** (50), 14243–14248.
- SIEWERT, C, BEC, J & KRSTULOVIC, G 2017 Statistical steady state in turbulent droplet condensation. *Journal of Fluid Mechanics* **810**, 254–280.
- GRABOWSKI, W. W & ABADE, G. C 2017 Broadening of cloud droplet spectra through eddy hopping: Turbulent adiabatic parcel simulations. *Journal of the Atmospheric Sciences* **74** (5), 1485–1493.

- ABADE, G. C, GRABOWSKI, W. W & PAWLOWSKA, H 2018 Broadening of cloud droplet spectra through eddy hopping: Turbulent entraining parcel simulations. *Journal of the Atmospheric Sciences* **75** (10), 3365–3379.
- POPE, S. B 1985 PDF methods for turbulent reactive flows. *Progress in Energy and Combustion Science* **11** (2), 119–192.
- POPE, S 1991 Mapping closures for turbulent mixing and reaction. *Theoretical and Computational Fluid Dynamics* **2** (5), 255–270.
- COLUCCI, P, JABERI, F, GIVI, P & POPE, S 1998 Filtered density function for large eddy simulation of turbulent reacting flows. *Physics of Fluids* **10** (2), 499–515.
- GIVI, P 2006 Filtered density function for subgrid scale modeling of turbulent combustion. *AIAA Journal* **44** (1), 16–23.
- KUMAR, B, SCHUMACHER, J & SHAW, R. A 2013 Cloud microphysical effects of turbulent mixing and entrainment. *Theoretical and Computational Fluid Dynamics* **27** (3-4), 361–376.
- BEALS, M. J, FUGAL, J. P, SHAW, R. A, LU, J, SPULER, S. M & STITH, J. L 2015 Holographic measurements of inhomogeneous cloud mixing at the centimeter scale. *Science* **350** (6256), 87–90.
- BEARD, K. V & OCHS, H. T 1993 Warm-rain initiation: An overview of microphysical mechanisms. *Journal of Applied Meteorology* **32** (4), 608–625.
- TELFORD, J. W & CHAI, S. K 1980 A new aspect of condensation theory. *Pure and Applied Geophysics* **118** (2), 720–742.
- YANG, F, SHAW, R & XUE, H 2016 Conditions for super-adiabatic droplet growth after entrainment mixing. *Atmospheric Chemistry and Physics* **16** (14), 9421–9433.
- DESAI, N, GLIENKE, S, FUGAL, J & SHAW, R 2019 Search for microphysical signatures of stochastic condensation in marine boundary layer clouds using airborne digital holography. *Journal of Geophysical Research: Atmospheres* **124** (5), 2739–2752.

- KOKHANOVSKY, A 2004 Optical properties of terrestrial clouds. *Earth-Science Reviews* **64** (3-4), 189–241.
- ANDREJCZUK, M, GRABOWSKI, W. W, MALINOWSKI, S. P & SMOLARKIEWICZ, P. K 2009 Numerical simulation of cloud–clear air interfacial mixing: Homogeneous versus inhomogeneous mixing. *Journal of the Atmospheric Sciences* **66** (8), 2493–2500.
- KUMAR, B, JANETZKO, E, SCHUMACHER, J & SHAW, R. A 2012 Extreme responses of a coupled scalar–particle system during turbulent mixing. *New Journal of Physics* **14** (11), 115020.
- PINSKY, M & KHAIN, A 2018 Theoretical analysis of mixing in liquid clouds–Part IV: DSD evolution and mixing diagrams. *Atmospheric Chemistry and Physics* **18** (5), 3659–3676.
- DIMOTAKIS, P. E 2005 Turbulent mixing. *Annual Review of Fluid Mechanics* **37**, 329–356.
- KOROLEV, A, KHAIN, A, PINSKY, M & FRENCH, J 2016 Theoretical study of mixing in liquid clouds–Part 1: Classical concepts. *Atmospheric Chemistry and Physics* **16** (14).
- PINSKY, M, KHAIN, A, KOROLEV, A & MAGARITZ-RONEN, L 2016*b* Theoretical investigation of mixing in warm clouds – Part 2: Homogeneous mixing. *Atmospheric Chemistry and Physics* **16** (14).
- ESWARAN, V & POPE, S 1988 Direct numerical simulations of the turbulent mixing of a passive scalar. *Physics of Fluids* **31** (3), 506–520.
- CHEN, H, CHEN, S & KRAICHNAN, R. H 1989 Probability distribution of a stochastically advected scalar field. *Physical Review Letters* **63** (24), 2657.
- FOX, R. O 1995 The spectral relaxation model of the scalar dissipation rate in homogeneous turbulence. *Physics of Fluids* **7** (5), 1082–1094.
- BAKER, M & LATHAM, J 1979 The evolution of droplet spectra and the rate of production of embryonic raindrops in small cumulus clouds. *Journal of the Atmospheric Sciences* **36** (8), 1612–1615.

- WARHAFT, Z 2000 Passive scalars in turbulent flows. *Annual Review of Fluid Mechanics* **32** (1), 203–240.
- SREENIVASAN, K. R, TAVOULARIS, S, HENRY, R & CORRSIN, S 1980 Temperature fluctuations and scales in grid-generated turbulence. *Journal of Fluid Mechanics* **100** (3), 597–621.
- CURL, R. L 1963 Dispersed phase mixing: I. Theory and effects in simple reactors. *AIChE journal* **9** (2), 175–181.
- VALINO, L & DOPAZO, C 1991 A binomial langevin model for turbulent mixing. *Physics of Fluids A: Fluid Dynamics* **3** (12), 3034–3037.
- FOX, R. O 1992 The Fokker–Planck closure for turbulent molecular mixing: Passive scalars. *Physics of Fluids A: Fluid Dynamics* **4** (6), 1230–1244.
- MEYER, D & JENNY, P 2006 A mixing model for turbulent flows based on parameterized scalar profiles. *Physics of Fluids* **18** (3), 035105.
- VALIÑO, L & GAO, F 1992 Monte Carlo implementation of a single-scalar mapping closure for diffusion in the presence of chemical reaction. *Physics of Fluids A: Fluid Dynamics* **4** (9), 2062–2069.
- FOX, R. O 1997 The Lagrangian spectral relaxation model of the scalar dissipation in homogeneous turbulence. *Physics of Fluids* **9** (8), 2364–2386.
- KLIMENKO, A. Y & POPE, S 2003 The modeling of turbulent reactive flows based on multiple mapping conditioning. *Physics of Fluids* **15** (7), 1907–1925.
- SIEBERT, H & SHAW, R. A 2017 Supersaturation fluctuations during the early stage of cumulus formation. *Journal of the Atmospheric Sciences* **74** (4), 975–988.
- ANDERSON, J. C, THOMAS, S, PRABHAKARAN, P, SHAW, R. A & CANTRELL, W 2021 Effects of the large-scale circulation on temperature and water vapor distributions in the π chamber. *Atmospheric Measurement Techniques* **14** (8), 5473–5485.
- THOMAS, S, PRABHAKARAN, P, CANTRELL, W & SHAW, R. A 2021 Is the water vapor supersaturation distribution Gaussian? *Journal of the Atmospheric Sciences* **78** (8), 2385–2395.

- HE, G.-W & ZHANG, Z.-F 2004 Two-point closure strategy in the mapping closure approximation approach. *Physical Review E* **70** (3), 036309.
- BRENNER, H & O'NEILL, M. E 1972 On the Stokes resistance of multiparticle systems in a linear shear field. *Chemical Engineering Science* **27** (7), 1421–1439.
- JEFFERY, G. B 1922 The motion of ellipsoidal particles immersed in a viscous fluid. *Proceedings of the Royal Society of London. Series A, Containing papers of a mathematical and physical character* **102** (715), 161–179.
- DEALY, J. M & WISSBRUN, K. F 2012 *Melt Rheology and its role in Plastics Processing: Theory and Applications*. Springer Science & Business Media.
- GOLDSTEIN, H 1980 *Classical mechanics*. Addison-Wesley.
- EINARSSON, J, MIHIRETIE, B, LAAS, A, ANKARDAL, S, ANGILELLA, J, HANSTORP, D & MEHLIG, B 2016 Tumbling of asymmetric microrods in a microchannel flow. *Physics of Fluids* **28** (1), 013302.
- HAPPEL, J & BRENNER, H 1983 *Low Reynolds number hydrodynamics: with special applications to particulate media*. Springer Science & Business Media.
- GUIRY, M. D & GUIRY, G. M 2016 AlgaeBase, www.algaebase.org, accessed 19 July 2016.
- ISHIMOTO, K 2020 Helicoidal particles and swimmers in a flow at low Reynolds number. *Journal of Fluid Mechanics* **892**.
- EINARSSON, J, CANDELIER, F, LUNDELL, F, ANGILELLA, J & MEHLIG, B 2015 Rotation of a spheroid in a simple shear at small reynolds number. *Physics of Fluids* **27** (6), 063301.

